# S-WAVE PROCESSING AND INTERPRETATION OF WIDE-ANGLE SEISMIC REFRACTION DATA, MALPELO RIDGE, EASTERN PANAMA BASIN

Dissertation
zur Erlangung des Doktorgrades
der Mathematisch-Naturwissenschaftlichen Fakultät
der Christian-Albrechts-Universität
zu Kiel

vorgelegt von

Irmgard Trummer

Kiel

2002

Referent: Prof. Dr. Ernst R. Flueh
Koreferent: Prof. Dr. Wolfgang Rabbel
Tag der mündlichen Prüfung: 1. November 2002
Zum Druck genehmigt: Kiel,

Der Dekan

# Abstract

The Panama Basin is defined as the area bounded by the continental margins of Panama and Colombia to the north and east, and by the aseismic Cocos and Carnegie Ridges to the west and south. The Cocos and Carnegie Ridges are considered as hotspot tracks of the Galapagos Hotspot, which is located beneath the Galapagos Archipelago today. The Galapagos Hotspot is believed to have influenced the tectonic history of the Panama Basin and its main tectonic features to a great extent. So is the origin of the Cocos and Carnegie Ridges attributed to the interaction of the hotspot and the nearby Cocos-Nazca Spreading Center. Malpelo Ridge is also believed to originate from such an interaction, but its existence as a former continuation of Cocos Ridge, shifted south along the Panama Fracture Zone, or as a former part of Carnegie Ridge, moved north through continuous rifting at the now inactive Malpelo Rift, is still disputed.

On a seismic wide-angle profile across Malpelo Ridge converted shear waves of very high quality were recorded, which enabled the evaluation of a model of Poisson's ratio versus depth, that was interpreted in terms of the lithological composition of the underground. Values of compressional and shear wave velocities and Poisson's ratios were mainly compared to laboratory measurements obtained from ophiolite sequences, and match the expected layering for the oceanic crust and upper mantle very well.

A sedimentary layer consisting of calcareous ooze covers a layer of extrusives, that is underlain by a sheeted dike complex and subsequently by pyroxene- and olivine gabbros. The upper mantle consists of ultramafites. The profile is divided into two distinct areas: the thickened crust beneath Malpelo Ridge and normal oceanic crust northwest off the ridge. For the thickened crust a higher degree of metamorphism is suggested. For the crust and upper mantle underneath Malpelo Ridge and northwest off the ridge a melt with a different chemical composition is indicated.

The oceanic crust between Regina Ridge, situated to the northwest of Malpelo Ridge, and Malpelo Ridge is proposed to have been formed at an abandoned spreading center in this area. Spreading at this abandoned rift is suggested to have occurred after Malpelo Ridge has been formed. A long-term influence of the hotspot is made responsible for a high magnesium content in the area northwest off Malpelo Ridge, which decreases with increasing distance to the hotspot due to ongoing spreading.

# Zusammenfassung

Das Panama Becken befindet sich südwestlich von Panama und Kolumbien und ist nach Süden und Westen hin durch zwei aseismische untermeerische Rücken, Cocos und Carnegie Rücken, begrenzt. Diese werden als Spuren der Plattenbewegung über den Galapagos Hotspot angesehen. Der Galapagos Hotspot befindet sich heute unterhalb des Galapagos Archipels und war wesentlich an der Enstehungsgeschichte des Panama Beckens und seiner tektonischen Einheiten beteiligt. Seine Nähe zum Cocos-Nazca Spreizungszentrum wird nicht nur mit der Bildung des Cocos und des Carnegie Rückens in Verbindung gebracht, sondern auch die Herkunft des Malpelo Rückens wird dem Hotspot zugeschrieben. Zur genauen Entstehung des Malpelo Rückens gibt es mehrere Theorien: Eine Interpretation beschreibt ihn als eine Verlängerung des Cocos Rückens, die entlang der Panama Bruchzone nach Süden verschoben wurde. Eine andere Möglichkeit wäre, den Malpelo Rücken als einen durch die heute inaktive Malpelo Spreizungszone nach Norden verschobenen Teil des Carnegie Rückens zu erklären.

Die Aufnahme von konvertierten Scherwellen sehr guter Qualität auf einem seismischen Weit-Winkel Profil quer zum Malpelo Rücken erlaubte die Berechnung eines Tiefenmodells der Poisson Zahl, das in Hinblick auf die Lithologie des Untergrundes interpretiert wurde. Vergleiche mit Labormessungen von Kompressions- und Scherwellengeschwindigkeiten und Poisson Zahlen, grösstenteils handelt es sich dabei um Probennahmen von Ophiolitkomplexen, bestätigen die zu erwartende Schichtabfolge in der ozeanischen Kruste.

Eine kalkhaltige Sedimentschicht bedeckt Extrusiva, die einen Sheeted Dike Komplex und in weiterer Folge Pyroxen- und Olivin-Gabbros überlagern, der obere Mantel besteht aus Ultramafiten. Das Profil wird in zwei unterschiedliche Bereiche geteilt, die verdickte Kruste des Malpelo Rückens und die normale ozeanische Kruste nordwestlich davon. Im Bereich der verdickten Kruste tritt ein erhöhter Metamorphosegrad auf. Weiters deuten die Daten darauf hin, dass Kruste und oberer Mantel in den beiden Bereichen aus aufgeschmolzenem Mantelmaterial unterschiedlicher chemischer Zusammensetzung und Herkunft bestehen.

Es scheint, dass die ozeanische Kruste zwischen Malpelo Rücken und dem nordwestlich davon gelegenen Regina Rücken an einem heute inaktiven Rift entstanden ist. Diese Spreizungszone wurde aktiv, nachdem der Malpelo Rücken entstanden ist, und die aufgetretenen erhöhten Magnesium-Gehalte in der gebildeten Kruste werden einem möglichen

lange anhaltenden Einfluss des Hotspots zugeschrieben. Der Einfluss des Hotspots wurde mit zunehmender Entfernung vom Spreizungszentrum durch die fortlaufende Krustenbildung geringer.

# Contents

# Introduction 1

The Galapagos Archipelago, located in the eastern Pacific, is the surface expression of the Galapagos Hotspot or mantle plume fixed in the mantle. It is associated by two long, linear, submarine ridges, which are commonly accepted to represent traces of the Cocos and Nazca Plates moving over the hotspot with the ridges marking the azimuths of plate motion relative to the hotspot (Figure 1.1). The area bounded by the aseismic Cocos and Carnegie Ridges to the west and south, and Panama and Colombia to the north and east, is defined as the Panama Basin. It has been formed through spreading at the Cocos-Nazca Spreading Center, which divides the northward subducting Cocos Plate from the eastward subducting Nazca Plate.

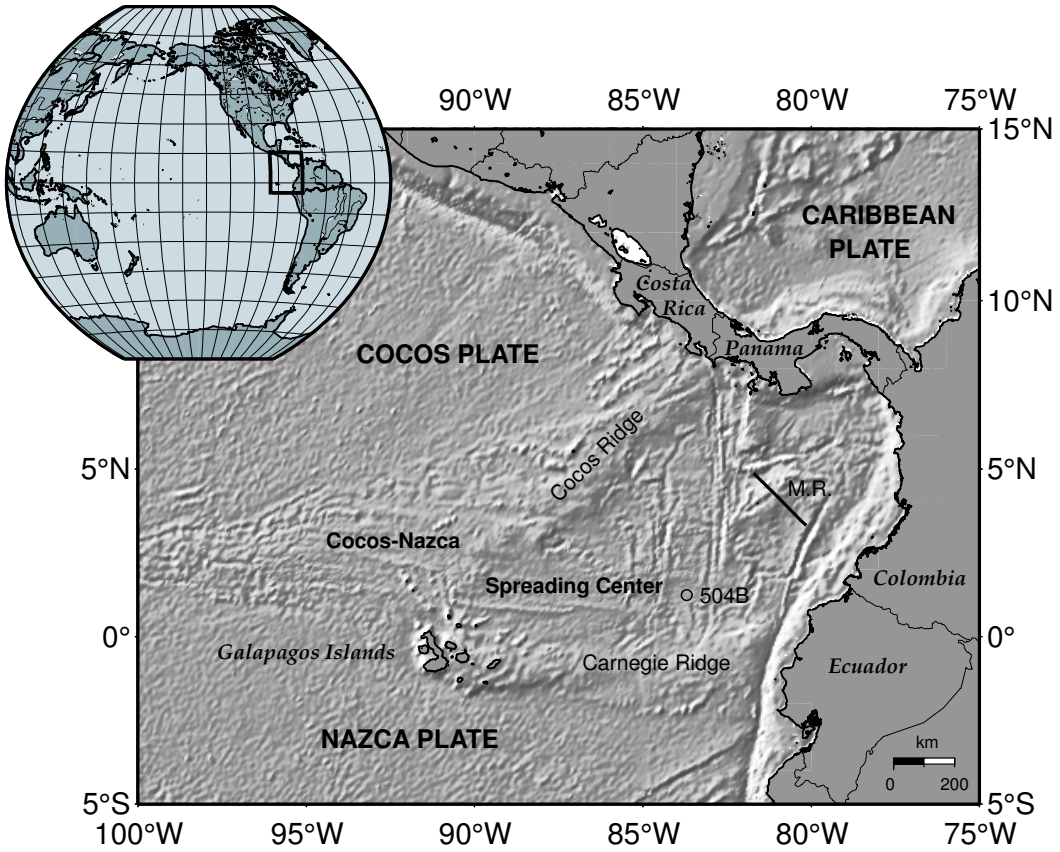


Figure 1.1: Bathymetric map of the Panama Basin. The basin is defined as the area bounded by Cocos Ridge to the west, Carnegie Ridge to the south, Costa Rica and Panama to the north, and Colombia and Ecuador to the east. The wide-angle profile across Malpelo Ridge (M.R.) is shown as a black line. Bathymetry is based on satellite altimetry [Smith and Sandwell, 1997].

In late 1999 marine investigations of the aseismic ridges located in the Panama Basin

were carried out within the PAGANINI project. PAGANINI is an acronym for *PA*nama basin and *GA*lapagos "plume" - *N*ew *IN*vestigations of *I*ntraplate magmatism. The project aimed at obtaining a better understanding of of the geodynamic processes in this region, which is characterized by asymmetric spreading, discrete jumps of the plate boundary, and the influence of the Galapagos Hotspot. Performed investigations included extensive geophysical, volcanological, geochronological, and geochemical studies in the region of the Panama Basin and the surrounding shelf area. The main tasks of the first two legs SO144-1&2 comprised seismic and seismological measurements [Bialas et al., 1999].

The third leg SO144-3 was mainly dedicated to geological and geochemical analyses [Werner et al., 2000].

Within the PAGANINI project a 244km long seismic wide-angle profile across Malpelo Ridge (Figure 1.1) was acquired. On this profile converted shear waves of surprisingly high quality were recorded. The work presented here deals with the evaluation of a model of Poisson's ratio across Malpelo Ridge that was interpreted in terms of the lithological composition of the crust and upper mantle.

The work is structured into the following parts:

Initially a short overview of the tectonic evolution of the Eastern Panama Basin including remaining uncertainties as e.g. the possible origin of Malpelo Ridge as a former part of Cocos or Carnegie Ridge is given. A discussion of shear wave conversion in oceanic crust and associated energy coefficients is followed by a summary of the main influences of temperature, pressure, and mineralogical composition, on Poisson's ratios of common crustal lithologies. A velocity-depth model based on evaluation of the recorded compressional waves (P-wave model) along the profile has been presented by Marcaillou [2000]. To facilitate the modeling process of a shear wave (S-wave) velocity depth model a new P-wave model was calculated, and processing and modeling of the compressional wide-angle data and the resulting P-wave model are discussed before the converted shear wave phases are presented. Processing of the horizontal components included rotation, filtering, and deconvolution. Modeling of the converted phases was performed based on the P-wave model. The resulting model of the distribution of Poisson's ratio across Malpelo Ridge was compared to laboratory measurements of an ophiolite sequence, findings from Deep Sea Drilling Project (DSDP) site 504B, and published results from refraction measurements on oceanic crust. The suggested lithology for the crustal layers and upper mantle is extensively discussed before probable inferences for the possible origin of Malpelo Ridge within the tectonic framework of the Panama Basin are presented.

# Tectonic Evolution of the Eastern Panama Basin

# 2

The Eastern Panama Basin is defined as the area enclosed by the continental margins of Panama and Colombia to the north and east, the Carnegie Ridge to the south and the Panama Fracture Zone to the west, which divides the eastern basin from the remaining western part of the Panama Basin itself. The Panama Basin, which extends westward to the Cocos Ridge, was formed by seafloor spreading along the Cocos-Nazca Spreading Center after the breakup of the Farallon Plate. Breakup of the Farallon Plate into the southern Juan de Fuca Plate and the northern Cocos- and Nazca Plates originated along the Grijalva Fracture Zone, that was identified as a pre-existing zone of weakness [Hey, 1977]. The Grijalva Scarp or Grijalva Fracture Zone, which is preserved on the Nazca Plate today, is interpreted to represent the scar where the breakup took place (Figure 2.1).

The geologic history of the Cocos-Nazca Spreading Center includes asymmetric spreading, discrete jumps of the plate boundary, and the influence of the Galapagos Hotspot, which is currently situated about 170km south of the spreading center. Commonly accepted models interpret both the aseismic Cocos and Carnegie Ridges as hotspot traces, formed through interaction of the hotspot with the spreading center, with the ridges marking the azimuths of plate motion relative to the hotspot. Carnegie Ridge, located on the Nazca Plate, is still actively growing at the Galapagos Islands at its western end. The oldest parts of the Galapagos Hotspot track, located on the Cocos Plate off the coast of Costa Rica, are part of Cocos Ridge and are dated at 13-14.5ma [Werner et al., 1999, Hoernle et al., 2000] but geochemical investigations of accreted oceanic complexes in Costa Rica indicate that the hotspot has been active for at least 90ma [Canales et al., 1997, Hauff et al., 1997].

The Cocos-Nazca Spreading Center (CNS) is an intermediate spreading center with spreading rates of 60-70mm/a. The ocean floor formed at the CNS has a rough topography and high-amplitude magnetic anomalies in contrast to the smooth topography and low-amplitude anomalies featuring the oceanic crust formed at the fast spreading East Pacific Rise (EPR) [Hey, 1977, Wilson and Hey, 1995, Barckhausen et al., 2001]. The rough-smooth boundary between these two provinces was first mapped by Hey [1977] and is considered as the trace of the triple junction of the EPR and CNS off Costa Rica (Figure 2.1). Its prolongation to the coast of Costa Rica has been recently defined more exactly by Barckhausen et al. [2001] through the evaluation of new magnetic data in the area.

Spreading between the Cocos and Nazca plates was initiated about 22.7ma probably due to their differing plate motions: the Cocos Plate subducts northeastward whereas

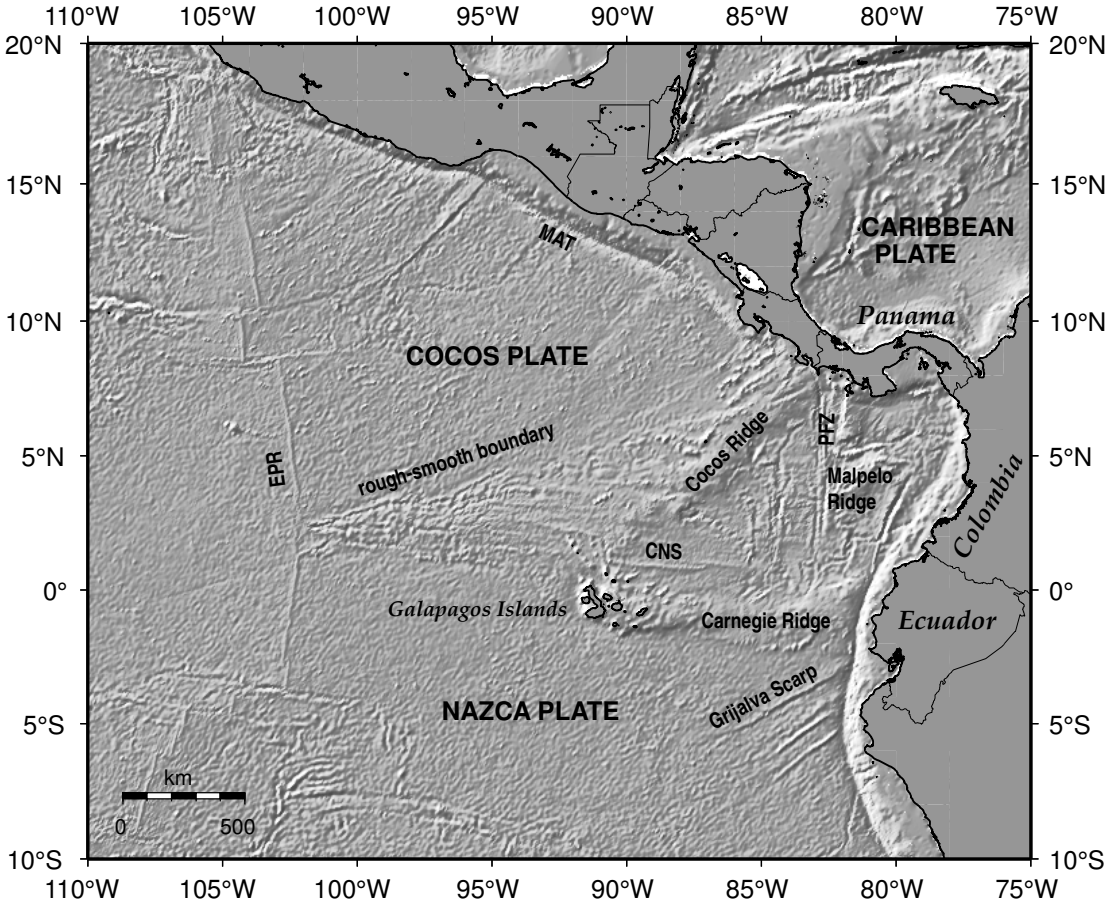


Figure 2.1: Bathymetric map of the of the East Pacific in the area of the Cocos-Nazca Spreading Center. EPR, East Pacific Rise; CNS, Cocos-Nazca Spreading Center; MAT, Middle America Trench; PFZ, Panama Fracture Zone. The rough-smooth boundary separates provinces formed at the East Pacific Rise and Cocos-Nazca Spreading Center. Bathymetry after Smith and Sandwell [1997].

the Nazca Plate subducts eastward. Barckhausen et al. [2001] refined the early models of Lonsdale and Klitgord [1978] and Pennington [1989] (Figure 2.2) for the evolution of the CNS and dated a major ridge jump to the south at 19.5ma after a phase of rapid and symmetric spreading. The ridge jump, after which spreading remained symmetric but at lower spreading rates (CNS-2 in Figure 2.3), was accompanied by a change in direction of the CNS by $22°$. At about 14.5ma another ridge jump to the south initiated a phase of frequent smaller southward ridge jumps that still continues (CNS-3 in Figure 2.3). Barckhausen et al. [2001] suggest the influence of the Galapagos Hotspot as a driving force for the frequent southward ridge jumps and the resulting asymmetric crustal accretion.

Current plate motions as deducted from satellite measurements are presented in Figure 2.4. The Cocos-Nazca Spreading Center is currently active at three east-west trending rift segments bounded by major north-south trending transform faults. The rifts are named

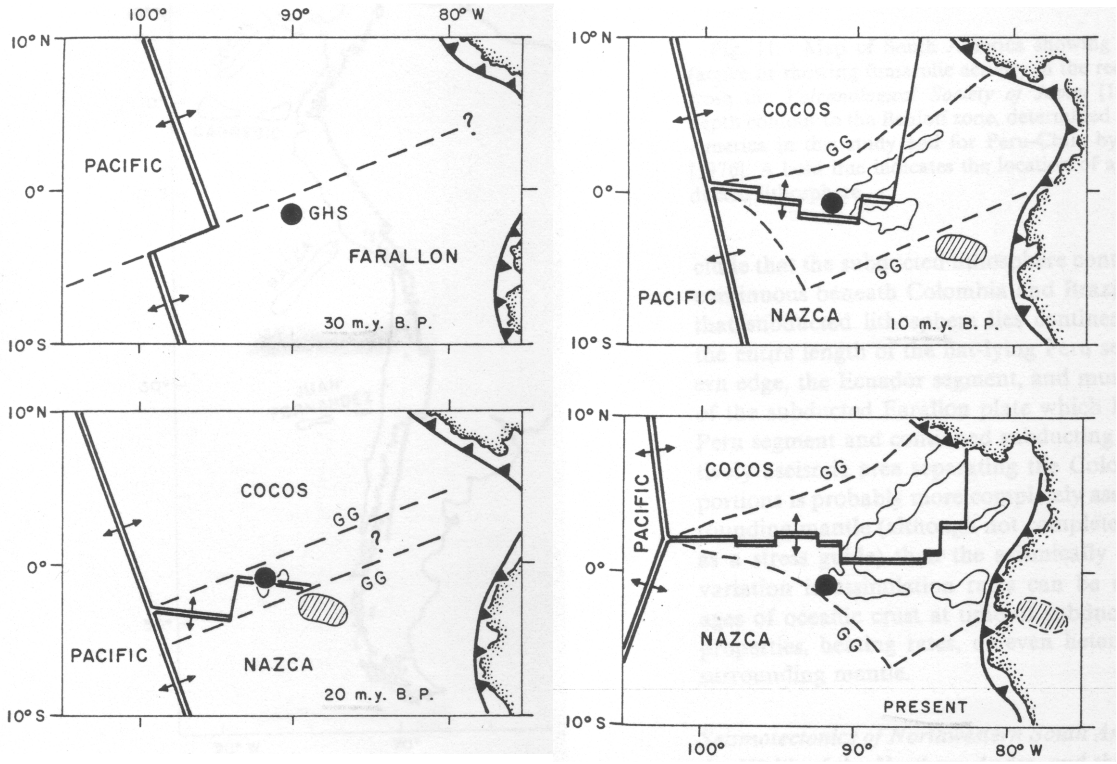


Figure 2.2: The interaction between the Galapagos Spreading Center and the Galapagos Hotspot (GHS) as proposed from Pennington [1989]. GG denotes the Galapagos Gore, which is the area within the pre-existing zones of weakness at which breakup of the Farallon Plate was initiated.

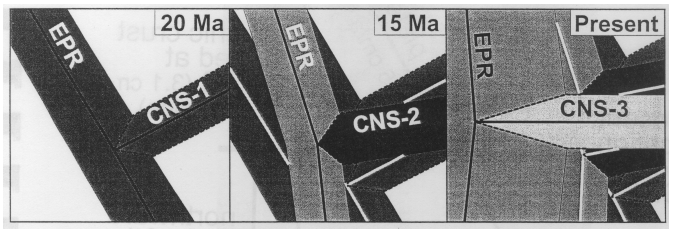


Figure 2.3: Schematic sketch of the evolution of the Cocos-Nazca Spreading Center summarizing its three-stage evolution. After Meschede et al. [1998].

the Galapagos Rift, the Ecuador Rift and the Costa Rica or Panama Rift, whose eastern boundary is the Panama Fracture Zone at $83°W$ [Hey, 1977, Lonsdale and Klitgord, 1978, Pennington, 1981].

For the western half of the Panama Basin a high density of magnetic, seismic reflection, and heat flow data has disclosed a detailed evolutionary scheme of the area. But east of the Panama Fracture Zone the structure and tectonic evolution is more complex. Active seafloor-spreading does not extend into this older part of the basin and most of the structural features are evidently relict [Lonsdale and Klitgord, 1978]. At the now extinct Fossil, Malpelo, and Buenaventura Rifts, spreading was probably asymmetric with half rates of 40mm/a to the north and 25mm/a to the south until 21ma. A reverse in the sense of asymmetry in spreading at the Buenaventura Rift accompanied by a decrease

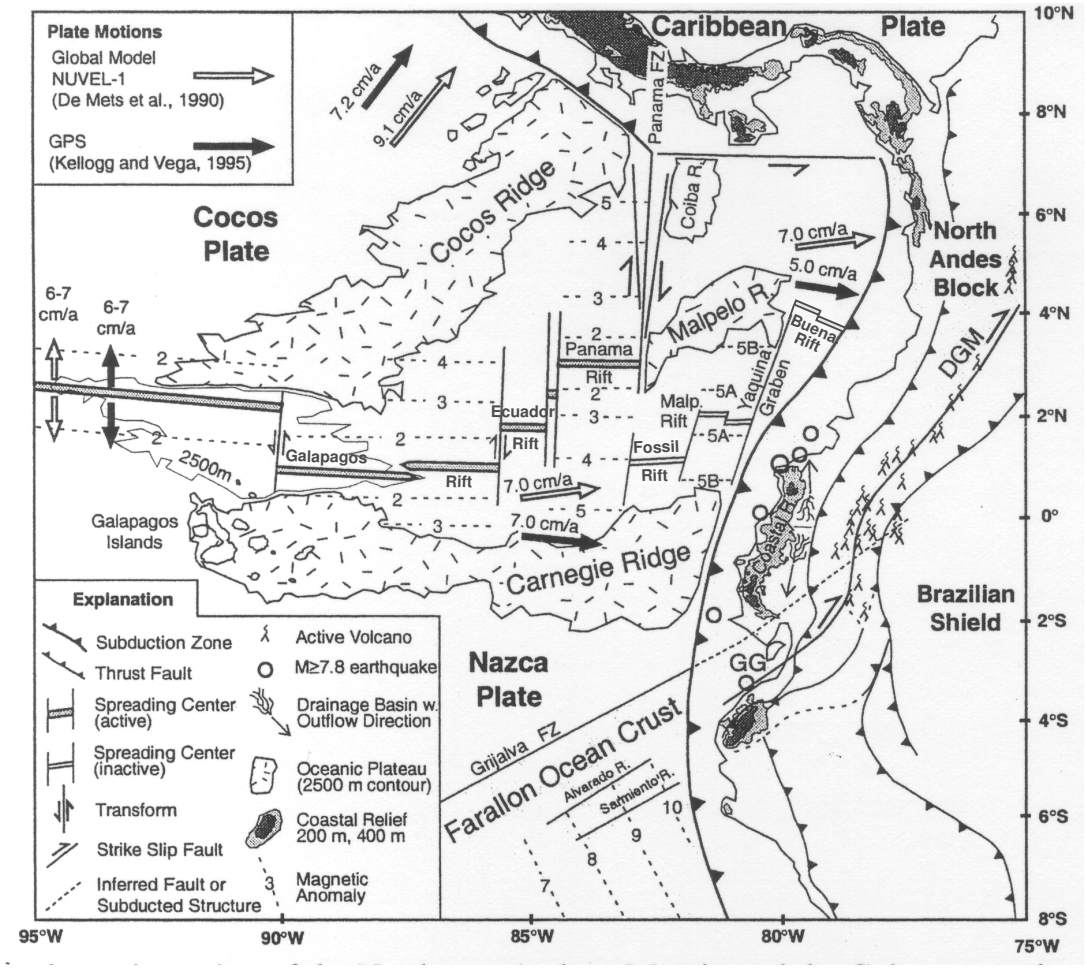


Figure 2.4: Main tectonic features of the Panama Basin, modified after Gutscher et al. [1999]. Buena. Rift, Buenaventura Rift; Grijalva FZ, Grijalva Fracture Zone; Panama FZ, Panama Fracture Zone.

in the half rate to 14mm/a at the northern flank culminated in a southward jump of the rift at about 16ma. The Buenaventura Rift was also split by a transform fault during this episode. Until 13ma near symmetric spreading occurred at the Buenaventura Rift while spreading at Malpelo Rift remained asymmetric [Hardy, 1991]. At 12ma spreading ceased at Buenaventura Rift and also at Malpelo Rift at 8ma, after 3ma of decreased spreathoughding. A possible explanation for cessation of spreading in the eastern Panama Basin is that an aseismic ridge, or maybe a northern equivalent of the Grijalva Scarp, collided with the northern subduction zone and blocked further spreading. The Coiba Fracture Zone as a nearby line of weakness may have acted as an additional trigger for this process. At the same time subduction ceased at the southern margin of Panama. It is unclear if cessation of subduction developed because of ceased spreading or vice versa. The existence of a Coiba microplate north of Malpelo Ridge, which moves independently from the Nazca Plate, remains controversial, though it could explain the differing strike of the magnetic lineations mapped in the northern and southern part of the basin

[Lonsdale and Klitgord, 1978, Hardy, 1991].

Since 8ma there has been continued asymmetric spreading on the Costa Rica Rift at a rate of about 66mm/a, which has increasingly separated Cocos and Malpelo Ridges. This continuation of spreading west of $83°W$, while spreading has ended at Malpelo and Buenaventura Rifts, has also led to the creation of a new Cocos-Nazca plate boundary between Cocos and Malpelo Ridges. This new plate boundary, extending from the Costa Rica Rift to the Nazca-Cocos-Caribbean triple junction near Coiba Island, evolved from the former fracture zone at $83°W$.

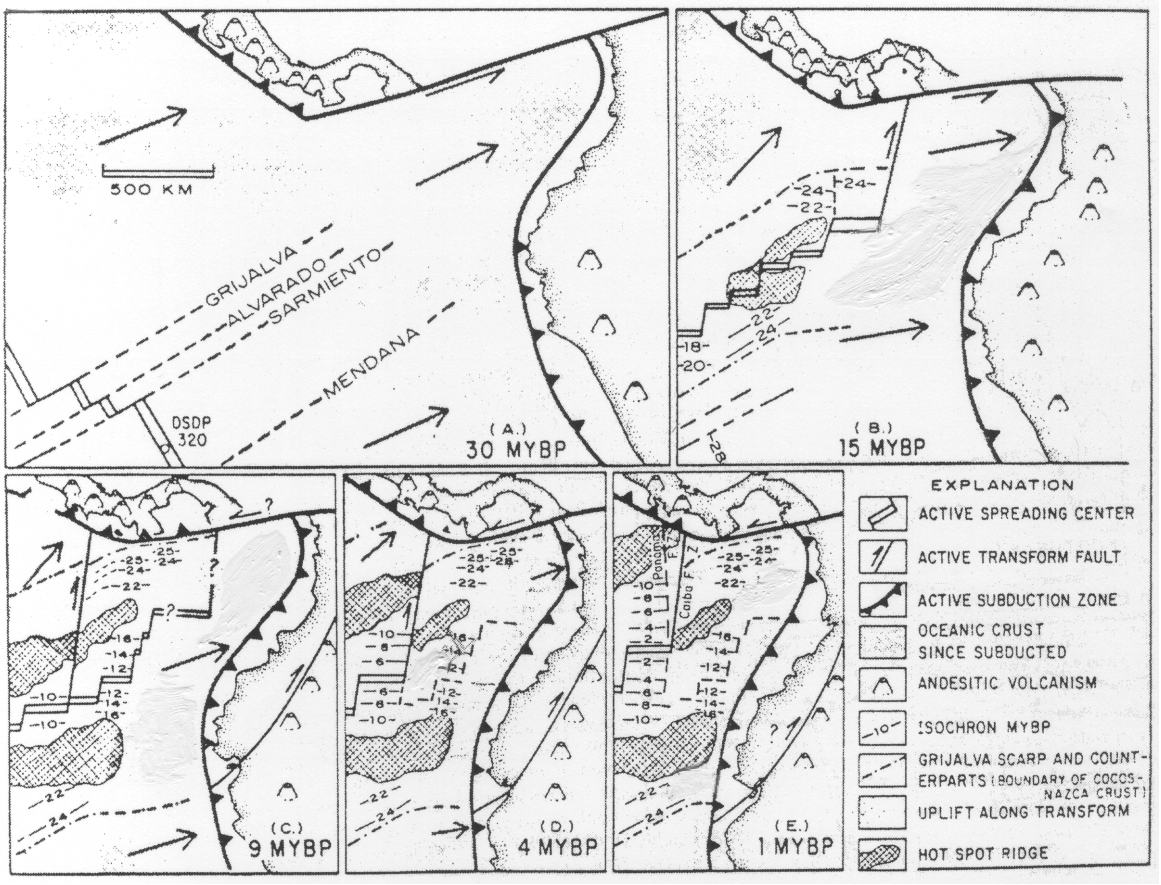


Figure 2.5: Tectonic reconstruction of the Eastern Panama Basin, from Lonsdale and Klitgord [1978].

Figure 2.5 illustrates the tectonic history of the Eastern Panama Basin as discussed by Lonsdale and Klitgord [1978]. At 30ma interaction of the Farallon Plate with the Caribbean and South American Plates is displayed, just before splitting along the Grijalva Fracture Zone initiated. At 15ma Malpelo and Carnegie Ridges are being formed by the Galapagos Hotspot, centered on the Nazca Plate. Lonsdale and Klitgord considered Malpelo Ridge as the oldest part of the hotspot trail and former continuation of Cocos Ridge. Malpelo and Carnegie Ridges were formed simultaneously and separated continuously by spreading at the Malpelo and Fossil Rifts. Separation between the Cocos and

Malpelo Ridges by dextral motion along the N-S trending Coiba Fracture Zone is dated at about 8ma. Slowing of spreading at the Malpelo Rift and cessation of subduction at the Panama Trench lead to further separation of the Cocos and Malpelo Ridges at 4ma. The movement of the triple junction between Cocos and Nazca Plates and the Coiba Fracture Zone to the Panama Fracture Zone is shown at 1ma [Lonsdale and Klitgord, 1978]. The origin of Malpelo Ridge is still disputed, its existence as the former continuation of Cocos Ridge, shifted south along the Panama Fracture Zone, or as the northern part of the former Carnegie Ridge, moved north through continuous rifting at the now extinct Malpelo and Fossil Rifts, is a controversial issue. More magnetic and geochemical data are probably needed to gain further comprehension of its detailed tectonic history.

## 2.1 Seismicity

Seismicity in the eastern Panama Basin is mainly restricted to the North Andean Margin, where the Nazca Plate subducts eastwards beneath South America at a rate of about 50-70mm/a, and the Panama Fracture Zone, which divides the northward subducting Cocos Plate from the Nazca Plate. The North Andean Margin between $6°N$ and $2.5°N$ exhibits a steep ESE-dipping subduction and a narrow volcanic arc, which broadens to the south, where the subduction of the aseismic Carnegie Ridge is associated with a seismic gap (Figure 2.4)[Gutscher et al., 1999]. The northern boundary of the Nazca plate subducts northward underneath the Panama Block west of $81°30'W$, while east of $81°30'W$ subduction has ceased and the northern margin of the Nazca Plate is located at the Southern Panama Fault Zone, south of the Azuero Peninsula (Figure 2.6). This fault zone is predominantly left-lateral strike slip and occupies an elongated sedimentary basin. The tectonics in this region are still discussed, some authors propose that active subduction occurs along the full length of the south Panama boundary [Westbrook et al., 1995].

Figure 2.6 displays the epicenter distribution of earthquakes with $M \geqslant 1.0$ recorded in the Eastern Panama Basin since 1901. Todays plate motions measured from 1988 to 1991 indicate that the northern part of the Nazca Plate moves eastward at a rate of 35mm/s while the plate south of Malpelo Ridge subducts southeastward at a rate of 50mm/a at the Colombian Trench and at a rate of 70mm/a at the Ecuadorean Trench [Kellogg and Vega, 1995]. These measurements were interpreted to support the existence of a separate North-Nazca Plate that extends south of Malpelo Island. A significant active northward spreading in the northern part of the Panama Basin is not supported [Kellogg and Vega, 1995]. Considering the strike-slip directions of the Panama Fracture Zone and Southern Panama Fault Zone and the plate motion of this part of the basin in an eastward direction, extensional tectonics within the basin are implicated, though. A separate Coiba microplate has also been proposed by Hardy [1991] with its southern boundary linked to an extinct, abandoned, rift zone at $5°N$, located northeast of Malpelo Ridge.

Near Malpelo Ridge (Figure 2.6) earthquakes occur mainly along the Panama Fracture Zone and within the Panama Rift and the Yaquina Graben. As can be observed from Figure 2.6 there is one earthquake south of Sandra Seamount and a few more are located at the northeastern prolongation of Regina Ridge and Sandra Seamount. These earthquakes have magnitudes ranging from $M_b$=3.5-6.2 and are located at shallow depths between 20km to 40km. At the northern flank of Malpelo Ridge, west of $81°50'W$, three earthquakes also form a line in northwestern direction, parallel to the Malpelo Ridge axis, with magnitudes $M_b$=4.8-5.3 and epicenter depths of 10-33km. Along the southern flank of Malpelo Ridge no seismicity is observed. The shallow earthquakes parallel to the northern flank of Malpelo Ridge indicate tectonic movements in the area between Malpelo and Regina Ridges, even if a possible North-Nazca Plate boundary is located south of Malpelo Island, as proposed by Kellog and Vega [1995].

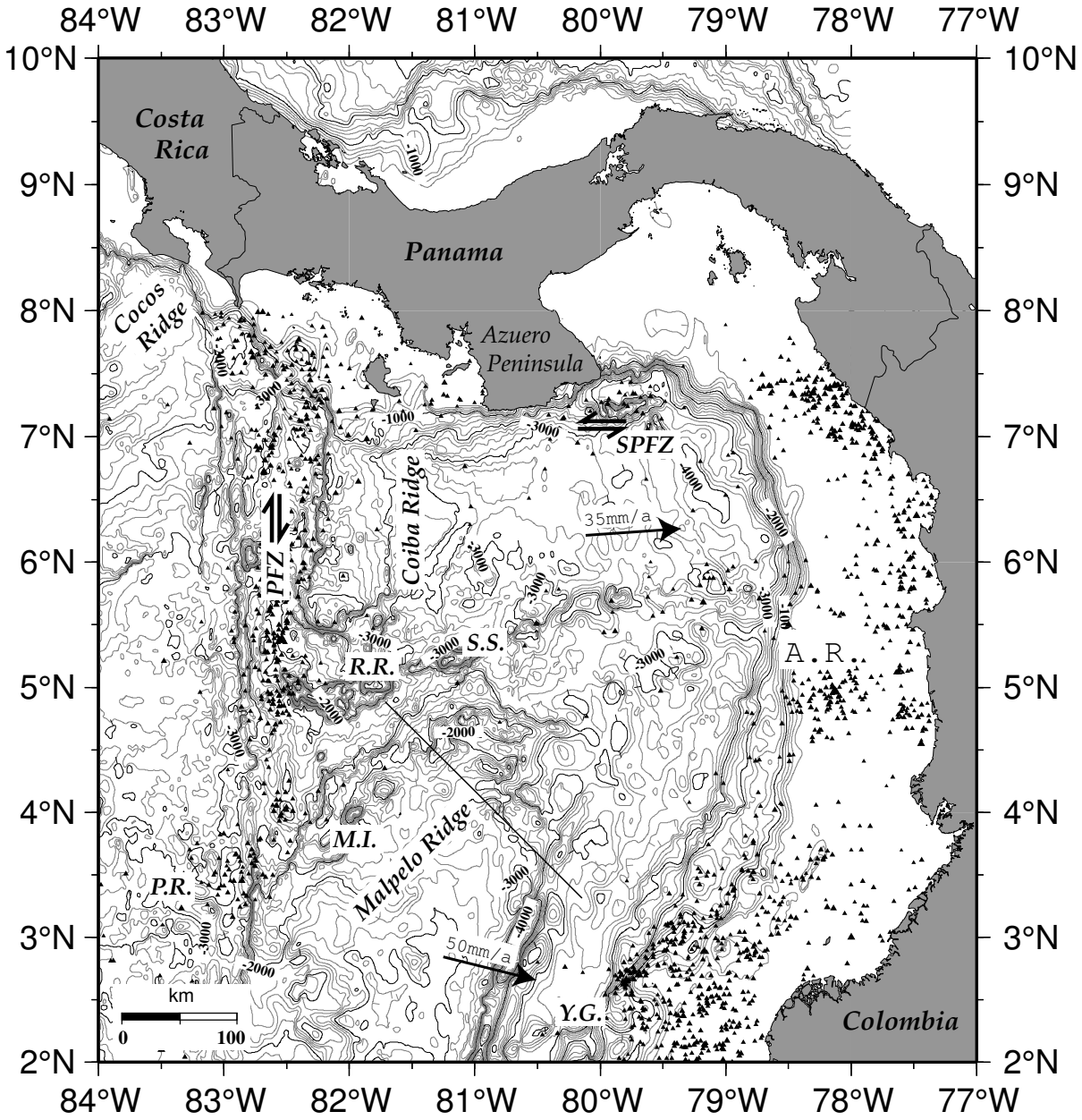


Figure 2.6: Epicenter distribution of earthquakes with $M_b \geqslant 1.0$ recorded near Malpelo Ridge. Plate motions are taken from Kellog and Vega [1995]. PFZ, Panama Fracture Zone; SPFZ, Southern Panama Fault Zone; R.R., Regina Ridge; S.S., Sandra Seamount; M.I., Malpelo Island; Y.G., Yaquina Graben; P.R., Panama Rift, and A.R., the zone of abandoned rifting as proposed by Hardy [1991]. Location of the wide-angle profile is shown as a black line. Earthquake data are taken from USGS earthquake databases SISRA (South American Catalogue, 1901-1973) and PDE (Preliminary Determination of Earthquakes Catalogue, 1973-2002). Bathymetry after Smith and Sandwell [1997].

# Shear Wave Conversion 3

Since airguns fired in a water layer generate a purely compressional wavefield, the shear waves observed in marine refraction data are generated through mode conversion. Mode conversion takes place at any interface in the subsurface and the amount of converted energy depends on the angle of incidence and the contrast in velocities and densities across the interface. In general an incident P-wave or S-wave generates reflected and transmitted S-waves as well as reflected and transmitted P-waves. The waves whose wave mode changes at the interface are called converted waves. The relationship between the amplitudes of the incident, reflected, and transmitted waves, can be described using the Zoeppritz Equations [Zoeppritz, 1919]. High velocity and/or density contrasts and large angles of incidence maximize converted energy and therefore may enable the recording of clear P- to S- converted arrivals.

The most plausible interface for generation of converted shear arrivals in marine refraction experiments is the interface between sedimentary layer and crystalline basement, which is usually providing a sharp velocity interface. In this context, sharp is defined with respect to one seismic wavelength. When velocity varies smoothly and gradually in solid media, mode converted waves are incoherent in phase whereas waves converted at a sharp interface are phase coherent and tend to be strong. The same argumentation about phase coherence can be applied to waves converted at a rough interface. For an interface topography with an amplitude approaching a seismic wavelength or more, converted waves will be radiated incoherently from the interface thus resulting in small converted waves.

In Figure 3.1 the wave modes that are most frequently recorded in marine refraction experiments are denoted. The PPS-wave gets converted at the sediment/basement interface underneath the OBS after traveling through the crust as a P-wave. The PSS-wave

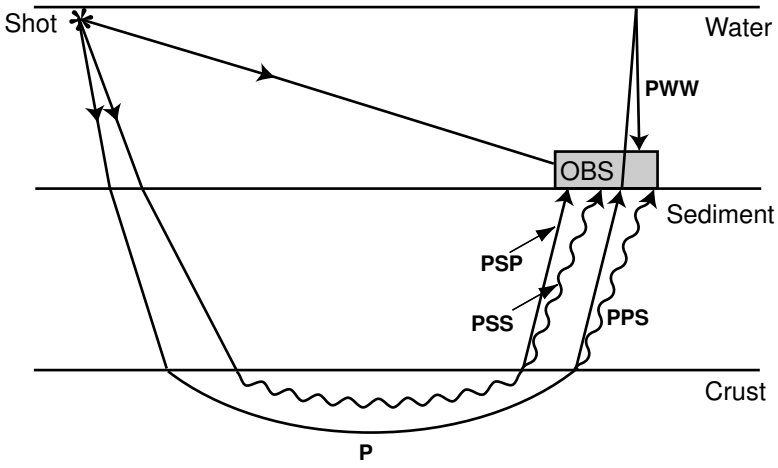


Figure 3.1: Nomenclature for converted waves in marine seismic experiments, modified after Au and Clowes [1984].

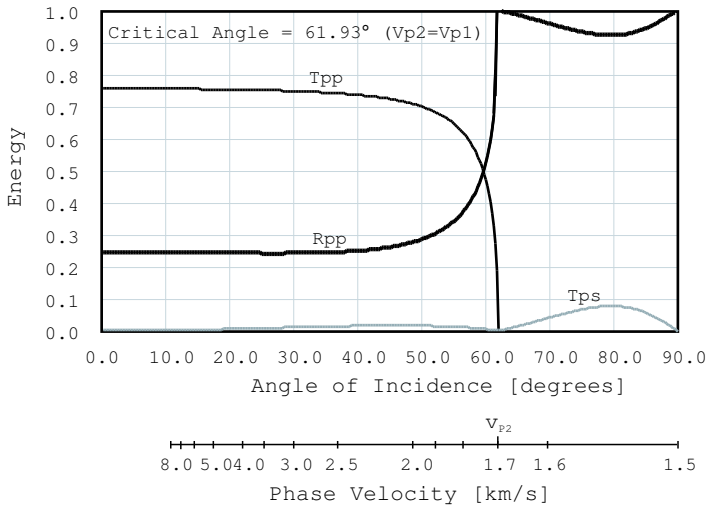


Figure 3.2: Partitioning of energy between transmitted and reflected waves as a function of angle of incidence. Incident wave is a P-wave in the water, reflection and transmission take place at the water/sediment interface. Rpp and Tpp denote energy of the reflected and transmitted P-wave, Rps and Tps denote energy of the reflected and transmitted S-wave. Curves have been calculated using the Zoeppritz Equations [Zoeppritz, 1919].

and PSP-wave travel through the crust as S-waves, the PSP-wave gets converted twice and reaches the OBS as a P-wave. PWW denotes the water wave multiple.

In Figures 3.2 and 3.3 energy partition as a function of the angle of incidence for transmitted and reflected waves at the water/sediment and sediment/basement interfaces are compared. The velocity values that were chosen for the calculations are given in Table 3.1 and are similar to those obtained from the seismic refraction profile across Malpelo Ridge and values published from Hamilton [1971, 1976], Spudich and Orcutt [1980] and Au and Clowes [1984]. $V_{p1}$, $v_{s1}$, and $\rho_1$ denote velocities and density of the incident medium, $v_{p2}$, $v_{s2}$, and $\rho_2$ of the refractive medium. For calculation of curves only generation of vertically polarized S-waves was assumed, as would be expected for conversion at a horizontal interface. As can be observed, the amount of energy converted from P-wave mode to S-wave mode for conversion at the water/sediment interface reaches a maximum of only $5\%$ of the energy of the incident wave for the transmitted S-wave (Tps) and no S-wave will be reflected from the interface. For conversion at the sediment/basement interface energy for the converted waves is much higher, the converted, transmitted, S-wave (Tps) reaches values of $50\%$ to $60\%$, which is in the range of the transmitted P-wave (Tpp). For small incident angles nearly all the energy is in the reflected and transmitted P-wave (Rpp, Tpp in Figures 3.2 to 3.4) and there are essentially no S-waves. Mode conversion gets considerable at angles between the P-wave critical angle, where $v_{p1} = v_{p2}$, and the S-wave critical angle ($v_{p1} = v_{s2}$) where energy for the converted waves reaches its maxima. At the S-wave critical angle energy on the converted, reflected, S-wave (Rps) reaches its maximum. For angles of incidence higher than the S-wave critical angle nearly $100\%$ of the incident energy will go into the reflected P-wave.

Figures 3.2 and 3.3 not only illustrate how much energy will be converted for certain velocity and density values but also underline the assumption that mode conversion for the data recorded across Malpelo Ridge took place at the sediment/basement interface and

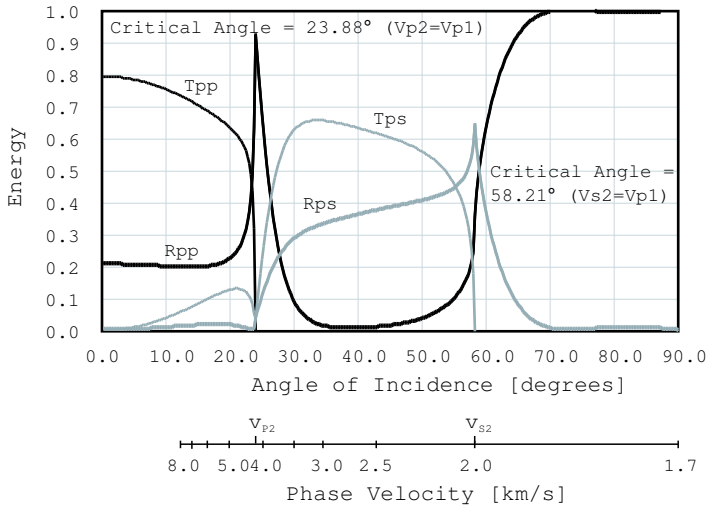


Figure 3.3: Partitioning of energy between transmitted and reflected waves as a function of angle of incidence. Incident wave is a P-wave in the sediment, reflection and transmission take place at the sediment/basement interface. Rpp, Tpp, Rps and Tps as in Figure 3.2.

not at the sea bottom.

| *Figure* | $v_{p1}[m/s]$ | $v_{s1}[m/s]$ | $\rho_1[kg/m^3]$ | $v_{p2}[m/s]$ | $v_{s2}[m/s]$ | $\rho_2[kg/m^3]$ |
|---|---|---|---|---|---|---|
| *3.2* | 1500 | 0 | 1000 | 1700 | 400 | 2600 |
| *3.3* | 1700 | 400 | 2600 | 4200 | 2000 | 2800 |
| *3.4* | 4200 | 2000 | 2800 | 1700 | 400 | 2600 |

Table 3.1: Parameters used for calculation of energy partitioning across an interface.

Figure 3.4 illustrates the effect of an incident S-wave encountering the sediment/basement interface from below (for velocity and density values see Table 3.1). Energy of the transmitted S-wave (Tss) is highest for angles smaller than the critical angle whereas energy of the converted and transmitted P-wave (Tsp) is about $60\%$ for a S-wave incident at angles higher than the critical angle. This is an important result for the case of the PSP-wave that undergoes two conversions. After conversion at the sediment/basement interface from P- to S-wave mode and again to P-wave mode still $36\%$ of the incident energy can be recorded by the OBS (not taking the filter effect of the earth into account). It has to be noted, that the energy of converted shear waves depend not only on the efficiency of conversion and crustal absorptivity but also on the crustal S-wave velocity structure. Thus the calculated value of $36\%$ represents the upper bound on the converted energy for the case of a PSP-phase for the given velocities and densities.

As for the case of an SPS-wave (not shown in Figure 3.1) that would travel through the sediment in S-wave mode and penetrate the crust in P-wave mode, the possibility to record such an event is much smaller. This wave mode requires not two but three conversions, starting with a conversion from the incident purely compressional water wave to a S-wave at the water/sediment interface. As can be seen from Figure 3.2 a maximum of only $10\%$ goes into such a converted, transmitted S-wave (Tps). This number will be further reduced to a negligible amount during the following conversions.

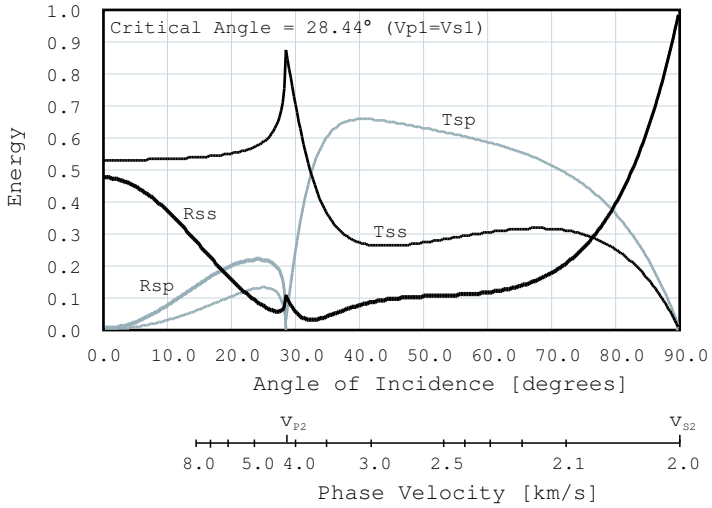


Figure 3.4: Partitioning of energy between transmitted and reflected waves as a function of angle of incidence. Incident wave is a S-wave in the basement, reflection and transmission take place at the basement/sediment interface. Rss and Tss denote energy of the reflected and transmitted S-wave, Rsp and Tsp denote energy of the reflected and transmitted P-wave.

Considering these values it remains an astonishing fact that the amount of recorded converted shear waves in marine refraction measurements still seems to be unpredictable. This may be mainly due to unfavorable velocity and density contrasts across the sediment/basement interface, e.g. lower velocity contrasts than in the examples shown have a decreasing effect on the energy values for the converted waves. Additionally the P-wave and S-wave critical angles act as boundary values, limiting the range of angles of incidence leading to measurable converted wave energy. This range will widen for a higher velocity contrast in $v_s$ but will counter-actively shorten for a smaller velocity contrast in $v_p$ across the interface.

Spudich and Orcutt [1980] and White and Stephen [1980] suggest another important factor for the efficiency of mode conversion at the sediment/basement interface: the filter effect of the basement velocities $v_p$ and $v_s$.

Instead of plotting partition energy versus the angle of incidence it is useful to plot the energy versus phase velocity, with phase velocity $v_{ph} = v_i / \sin \alpha_i$, $v_i$ being the velocity of the incident wave, $\alpha_i$ the incident angle. E.g. for Figure 3.3 it is a striking detail that the critical angles, where energy becomes very small, are, in terms of phase velocity, equivalent to incident phase velocities resembling $v_p$ and $v_s$ of the lower medium or basement. As Spudich and Orcutt [1980] and White and Stephen [1980] have pointed out, this leads to the useful way of viewing the top of the oceanic crust as a phase velocity filter for converted shear waves. More specifically it is a notch filter with its minimum falling at the compressional velocity of the basement and its width increasing with increasing $v_p$ and decreasing $v_s$ in the basement. Since typical phase velocities for converted shear waves fall in the range of 3.7-3.9km/s for the crustal S-wave refractions, 4.5-4.8km/s for the mantle refraction and 3.7-5.5km/s for the shear wave reflected from the mantle, it has to be expected that at least some part of the crustal shear response will be filtered out at the sediment/basement interface. This connection between basement velocities and con-

verted shear wave energy is apparently more evident when viewing converted energy or reflection and transmission coefficients in terms of phase velocity (Figures 3.2 to 3.4).

# Poisson‘s Ratio 4

Poisson‘s ratio is one of the constants describing wave propagation in isotropic homogenous media, like bulk modulus or Young‘s modulus. They all originally result from classic experiments, where relative changes of the length and diameter of a bar under tension were measured. In this context, Poisson‘s ratio $\sigma$ is expressed in terms of length $L$ and diameter $D$ as the ratio of radial contraction to axial elongation:

$$\sigma = -\frac{L\Delta D}{D\Delta L} \tag{4.1}$$

Changes in length $\Delta L$ and diameter $\Delta D$ are also related to particle motion and propagation velocity and this relationship results in the following expression of $\sigma$ in terms of compressional velocity $v_p$ and shear velocity $v_s$:

$$\sigma = \frac{\left(\frac{v_p{}^2}{2v_s{}^2} - 1\right)}{\left(\frac{v_p{}^2}{v_s{}^2} - 1\right)} \tag{4.2}$$

Since for $\sigma = 0$, $v_p/v_s = \sqrt{2}$, and for $\sigma = 0.5$, $v_p/v_s = \infty$, values of Poisson‘s ratio for solids theoretically fall between 0 and 0.5. Liquids or incompressible solids as well as materials without rigidity, have a Poisson‘s ratio of 0.5.

Rock Poisson‘s ratios can be calculated from compressional and shear wave velocity measurements using equation 4.2. To account for in situ conditions, laboratory measurements on rock samples are generally performed at elevated hydrostatic pressures. Otherwise open crack porosity would influence velocity measurements and results would depend to a great extent on crack structure, distribution and possible filling. Another aspect that has to be considered concerning laboratory measurements is the effect of anisotropy. For anisotropic samples shear wave velocity has to be measured in three directions resulting in Poisson‘s ratios depending on wave propagation direction. Strictly, the relationship between Poisson‘s ratio $\sigma$ and seismic velocities $v_p$ and $v_s$ (Equation 4.2) is appropriate only for isotropic media, thus the values of Poisson‘s ratio calculated are apparent values.

Having the potential of providing valuable constraints on lithological composition, several publications have focused on investigations of oceanic or continental crust using Poisson‘s ratio, e.g. Spudich and Orcutt [1980], Au and Clowes [1984], during the last few decades. Comparable laboratory measurements of compressional and shear wave velocities were published simultaneously [Salisbury and Christensen, 1978, Christensen, 1996, Kern and Richter, 1981], enabling possible correlation with findings of seismic measurements. The following sections will provide an overview on the influences of pressure, temperature, and rock composition, on compressional and shear wave velocity and thus Poisson‘s ratio on rocks typical for crust and mantle.

### Pressure and Temperature Effects

To relate Poisson's ratio with crustal composition and/or rock type, its pressure and temperature dependence are important factors. Figure 4.1 presents the effect of increasing pressure and temperature for major rock types. As can be seen in Figure 4.1(a) there is a slight increase in Poisson's ratio with increasing pressure from 200MPa to 1GPa, which is approximately equivalent to depths of 7km to 35km. At lower pressures than 200MPa (not shown in Figure 4.1(a)) Poisson's ratio is following an exponential curve due to a decrease in porosity due to compaction of porespace, in particular the closing of microcracks. In terms of velocity, P-wave as well as S-wave velocity are increasing with increasing pressure an effect which passes on to the values of $\sigma$ derived.

Increasing temperature lowers both P-wave and S-wave velocities due to thermal expansion of the constituent minerals that may cause grain boundary cracks to widen and new cracks to open [Kern and Richter, 1981].

Velocities are not decreasing to the same extent, though, resulting in a slightly increasing Poisson's ratio for increasing temperature. Figure 4.1(b) illustrates Poisson's ratio versus temperature at a given hydrostatic pressure of 600MPa, equivalent to approximately 20km depth. The variation in $\sigma$ is about $\pm 1\%$, which is within the experimental error. For temperature values higher than $500°$C the change in slope and decrease in Poisson's ratio indicates the onset of thermal cracking. The transition from $\alpha-$quartz to $\beta-$quartz is not observed for quartz-bearing rocks at a pressure of 6kbar since the transition temperature at such high pressures is placed outside the investigated temperature range [Kern and Richter, 1981].

In summary, dependence of Poisson's ratio on pressure and temperature is related mainly to porosity at low pressures and on rock composition and elastic properties of the constituent mineral content at higher pressures.

### Variation with Rock Types

As can be seen in Figure 4.1 values for Poisson's ratio for major rock types are commonly in the range of 0.25 to 0.32. With a Poisson's ratio below 0.15 quartzite shows an extreme low value. Variations for different types of quartzite depend on the content of pure quartz since quartz shows the lowest Poisson's ratio of all minerals (0.08). On the contrary feldspars have relatively high Poisson's ratios (0.28 to 0.3) as a consequence of high P-wave and low S-wave velocities. Poisson's ratio for many crustal rocks depends on the content and type of plagioclase feldspar, because Poisson's ratio of anorthite equals 0.314 compared to the relatively low value of 0.28 for albite. Tholeiitic or andesitic basalt, as mostly found in oceanic crust, have a very high anorthite content which therefore defines their Poisson's ratio. In addition, progressive metamorphism can be accompanied by a gradual increase of Poisson's ratio due to changes in plagioclase composition. Anorthite-rich plagioclase in basalts breaks down to albite at low metamorphic grades, but increases in anorthite content to andesine in amphibolites and labradorite in

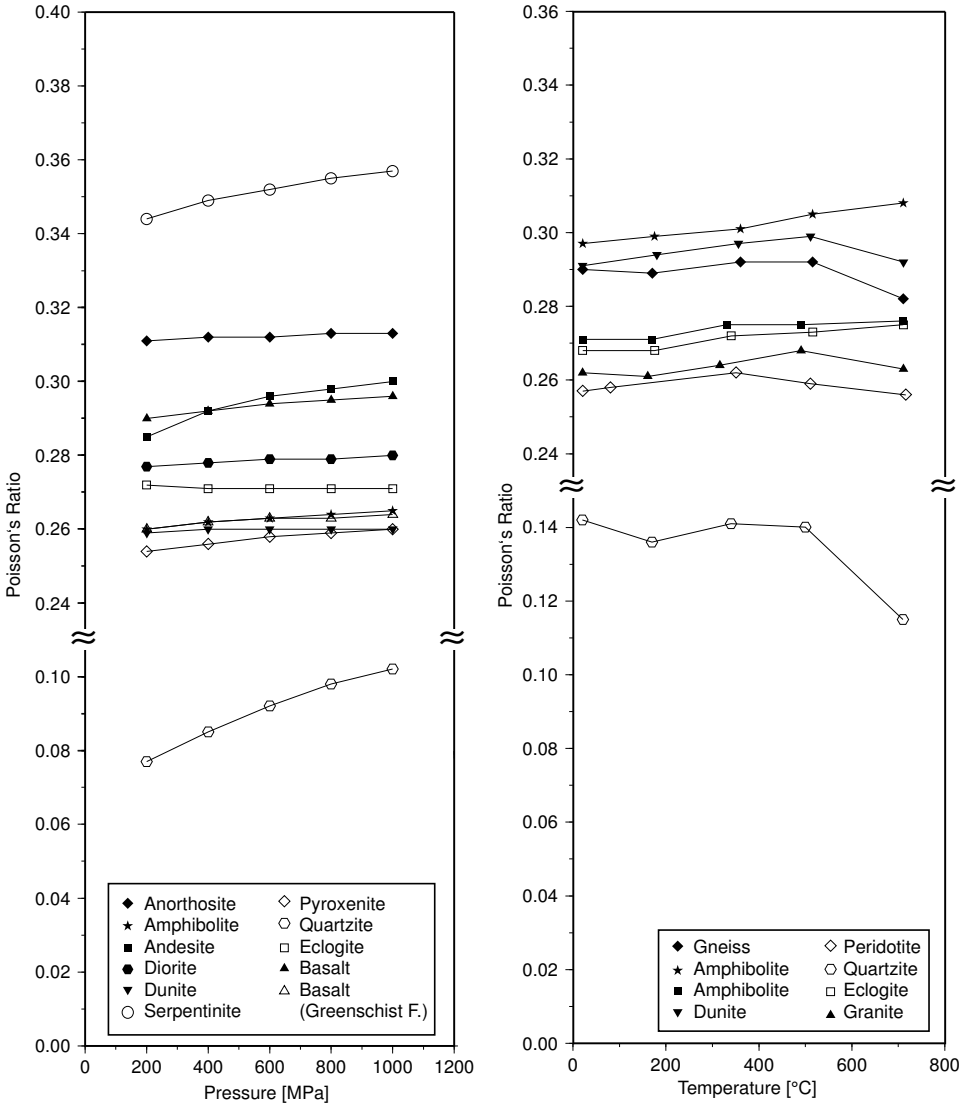


(a) Poisson's ratio versus pressure for rocks at room temperature. Data taken from Christensen (1996).

(b) Poisson's ratio versus temperature for rocks at 600MPa. Data taken from Kern and Richter (1981).

Figure 4.1: Pressure and temperature dependence of common crustal rocks.

mafic granulites [Christensen, 1996].

The contrary effect, a decrease in Poisson's ratio with metamorphism, is observed in the transition from basalt to greenschist and amphibolite facies. Transition to granulite facies is accompanied by an slight increase followed by a slight decrease as eclogite facies becomes stable. These changes in Poisson's ratio correlate with the various mineral actions caused through altered pressure and temperature conditions [Christensen, 1996]. Figure 4.1(a) also illustrates this effect of metamorphism. Serpentinization of dunite to

serpentinite forces Poisson's ratio to change from average 0.26 in dunite to an average 0.35 in serpentinite. Partially serpentinized dunites and peridotites have values that fall between these limiting values.

Another significant trend in Poisson's ratio is due to Fe-Mg substitution in pyroxenes and olivines. For the orthopyroxenes Poisson's ratio increases from 0.209 in enstatite ($MgSiO_3$) to 0.28 in orthoferrosilite ($FeSiO_3$). The two endmembers of the olivine series show values of 0.24 (forsterite, $Mg_2SiO_4$) and 0.336 (fayalite, $Fe_2SiO_4$) [Christensen, 1996].

# Crustal Structure of Malpelo Ridge 5

## 5.1 Malpelo Ridge

Malpelo Ridge is considered as one of the oldest parts of thickened crust in the Panama Basin that originated from the Galapagos Hotspot. It has been suggested to be either a former continuation of Cocos Ridge that was later transferred south along the Panama Fracture Zone [Hey, 1977] or to represent part of Carnegie Ridge that was rifted north at the Malpelo Rift [Lonsdale and Klitgord, 1978, Pennington, 1981, Hardy, 1991].

Malpelo Ridge has a length of 300km, a width of 100km, and occupies an area of about 15.000km$^2$. Most of the area lies 1000m below sea-level though the highest elevation of 254m above sea-level is obtained by Malpelo Island, slightly less than 1km$^2$ in area. Lonsdale and Fornari [1980] described it as an "elongate dome with a rough, lineated northwest flank and a southeast flank that gradually merges with the surrounding seafloor. The dome is bisected by a central graben that trends $060^\circ$ and divides a narrow, steep-sided northwest ridge from a more extensive southeast plateau. The central graben is 18km wide, and the normal faults that define its near-vertical walls have total throws of up to 3km". They also inferred sediment thickness from airgun records and showed that the graben is filled with up to 1km of sediment while for the surrounding flanks sediment thickness seldom exceeds 300m.

Data from a pair of crossed seismic refraction profiles recorded in 1973 displayed P-wave velocities of 4.2-5.2km/s and 6.7-7.15km/s for the upper and lower crust, respectively. No refractions of the mantle were observed on the data, but a minimum depth of 16-19km was calculated for the seismic Moho [Wade et al., 1977].

## 5.2 Data Acquisition

Within the PAGANINI project a 244km long seismic refraction profile across Malpelo Ridge was acquired. The seismic signals were generated by a set of three *BOLT* airguns, Model 800 CT. Each airgun has a volume of 2000in$^3$ (32 liter) and the main frequency of the generated signal is centered around 6 to 8Hz. The shots were triggered in time intervals of 60s at a speed of 3.5kn, resulting in an average shot point distance of 105m. A total of 33 Ocean Bottom Instruments comprising 17 GEOMAR Ocean Bottom Hydrophones (OBH), 2 GEOMAR Ocean Bottom Seismometers [Bialas and Flueh, 1999] and 13 Ocean Bottom Seismometers (OBS) [Nakamura and Garmany, 1991] from IRD-GéoAzur, were deployed along the profile. A detailed location map is provided in Figure

5.1, Figure 5.2 illustrates the seabed topography along the profile. Locations of the Ocean Bottom Instruments that recorded useful data are displayed in both Figures. OBS stations 122 to 116 are situated on normal oceanic crust between Regina Ridge to the northwest and Malpelo Ridge to the southeast. OBS 115 was placed on the northwest ridge which steep sided slope marks the boundary of Malpelo Ridge to the northwest. The south-eastern boundary of Malpelo Ridge, the so-called southeast plateau (OBH 107 to 102), merges gradually with the surrounding seafloor, where OBH 96 to 90 were located. OBS 113 to OBH 108 were situated above the 40km wide central graben, which is bounded by steep-sided flanks to both sides.

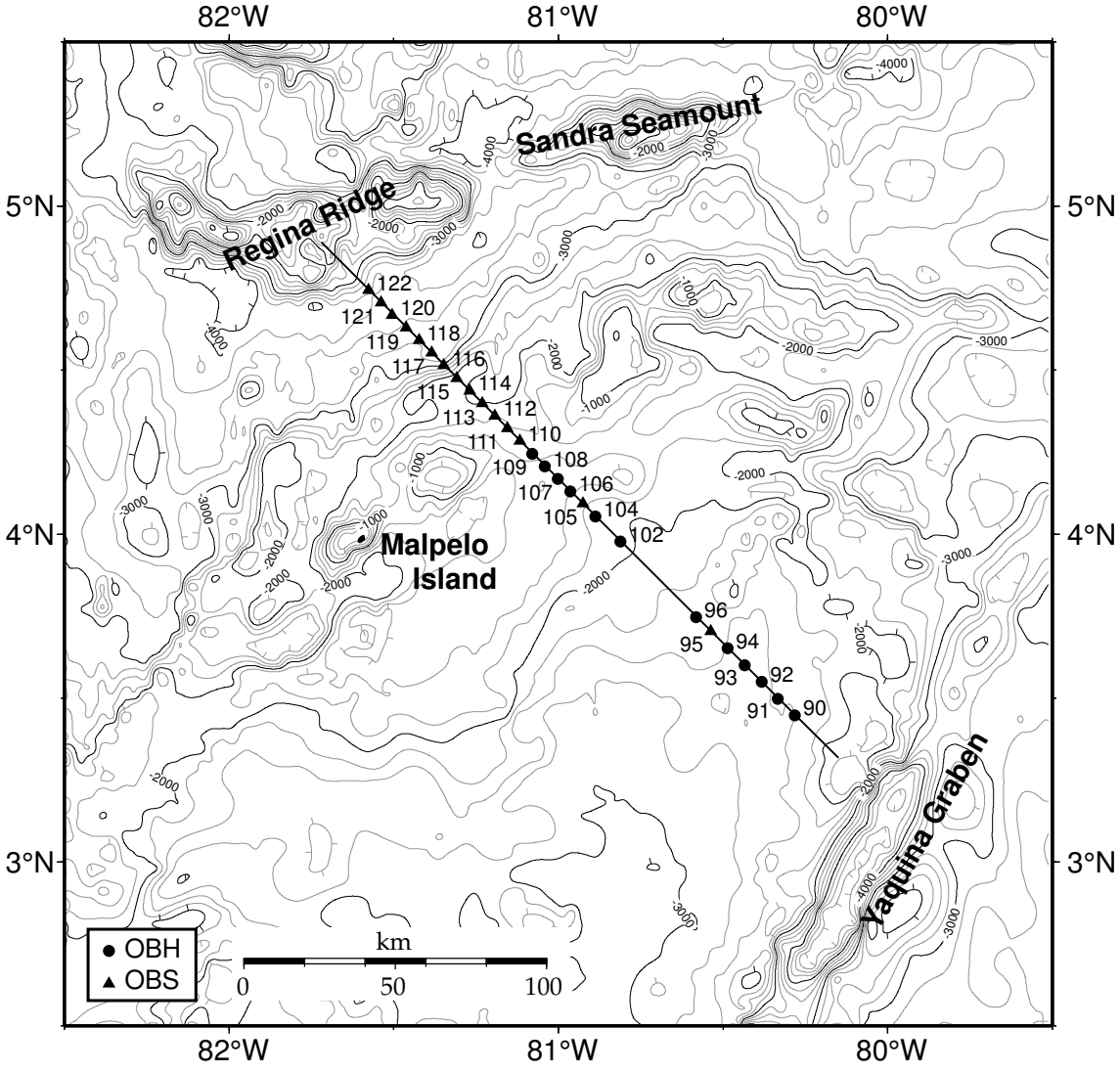


Figure 5.1: Location Map of the seismic wide-angle Profile P03 across Malpelo Ridge, as part of the PAGANINI Project. Bathymetry after Smith and Sandwell [1997].

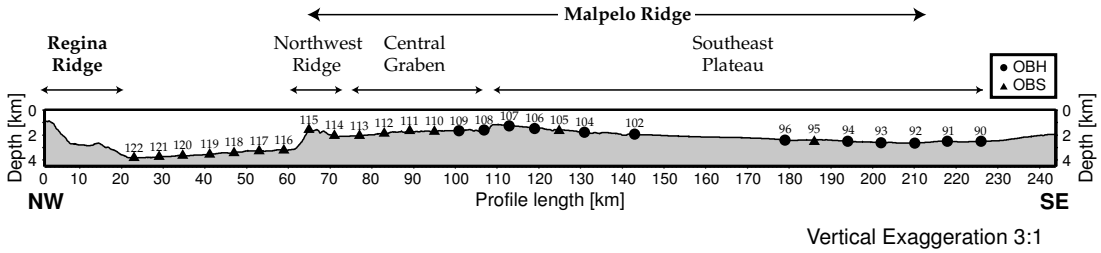


Figure 5.2: Seabed topography along the seismic wide-angle Profile P03 across Malpelo Ridge. Water depth varies from 3450m at OBH 107 to 4750m at OBS 122. Symbols denote positions of OBH and OBS stations that were input into the forward modeling process.

Unfortunately 6 of the Ocean Bottom Hydrophones failed to record any data due to technical problems, and OBS 95 and OBS 105 did not record on both horizontal components. The 13 OBS from IRD-GéoAzur that were situated at the northwestern part of the profile recorded converted shear waves of surprisingly high quality. Converted wave phases that have partly travelled through the crust as shear phases could also be identified on the OBH record sections and were highly valuable in constraining and confirming shear wave velocities, especially for that areas along the profile where no 4-component receivers were available.

Modeling of the S-wave data is based on a preliminary velocity-depth model derived from modeling of the P-wave data. In the following the calculation of the P-wave velocity-depth model will be discussed before processing and modeling of the S-wave model, building up on the P-wave model as a starting model, is presented in more detail.

## 5.3 Compressional Wave Data

### 5.3.1 Data Processing

Data processing included relocation of the instrument position by analysis of the direct arrivals. Filtering and deconvolution are important steps in the data processing sequence to enhance data quality with the prospect of obtaining record sections with clearer arrivals for picking and modeling.

#### Filtering and Deconvolution

Filter and deconvolution tests were performed for different offsets and time windows. As a broad frequency range is contained in the data, especially regarding to near- and far-offset traces, a time and offset dependent frequency filter was applied. Filter parameters were applied on time reduced record sections with a reducing velocity of 6.0km/s for vertical/hydrophone components and are presented in Table 5.1. A predictive deconvolution with a gate length of 3000ms was applied to the data to further improve temporal

| offset [km] | time [sec] | lower stop/pass | upper stop/pass |
|---|---|---|---|
| 0 | 1 | 3/5 | 28/48 |
| | 3 | 3/5 | 23/38 |
| | 5 | 3/5 | 18/28 |
| | 8+ | 3/5 | 13/18 |
| 10 | 1 | 3/5 | 28/48 |
| | 3 | 3/5 | 23/38 |
| | 5 | 3/5 | 18/28 |
| | 8+ | 3/5 | 13/18 |
| 20 | 1 | 3/5 | 23/38 |
| | 4 | 3/5 | 18/28 |
| | 7+ | 3/5 | 13/18 |
| 40 | 1 | 3/5 | 18/28 |
| | 5+ | 3/5 | 13/18 |
| 70+ | 1+ | 3/5 | 13/18 |

Table 5.1: Offset and time dependent filter parameters applied to compressional wave data.

resolution. Overlap time between the gates as well as the merging region, was 1000ms. Deconvolution parameters are given in Table 5.2. Figure 5.3 compares the record section of OBH station 93 before and after application of the discussed processing steps. The raw data (upper image) are bandpass filtered.

| Component Type | Operator Length [ms] | Prediction Lag [ms] | Prewhitening [%] |
|---|---|---|---|
| P-wave | 300 | 100 | 0.1 |

Table 5.2: Parameters for predictive deconvolution of compressional wave data.

### 5.3.2 Modeling

For seismic forward modeling a 2-D raytracing method after Luetgert et al. [1992], was chosen. The program MACRAY allows interactive manipulation of a velocity model using a layer-stripping technique, starting from the uppermost layer which comprises only the seafloor morphology. The various phases could be picked with an accuracy of 50ms to 100ms. Seven representative record sections are displayed in Figures 5.4 to 5.10. Refractions from the upper crustal layers exhibit a good signal-to-noise ratio and could be identified easily. The refraction from the lower crust can be followed up to an offset of 80km on most record sections and is often visible again at an offset of 120km. The PmP, the reflection from the crust/mantle boundary, has a generally weak appearance with most of its energy concentrated at offsets between 60km and 100km. The refraction from the

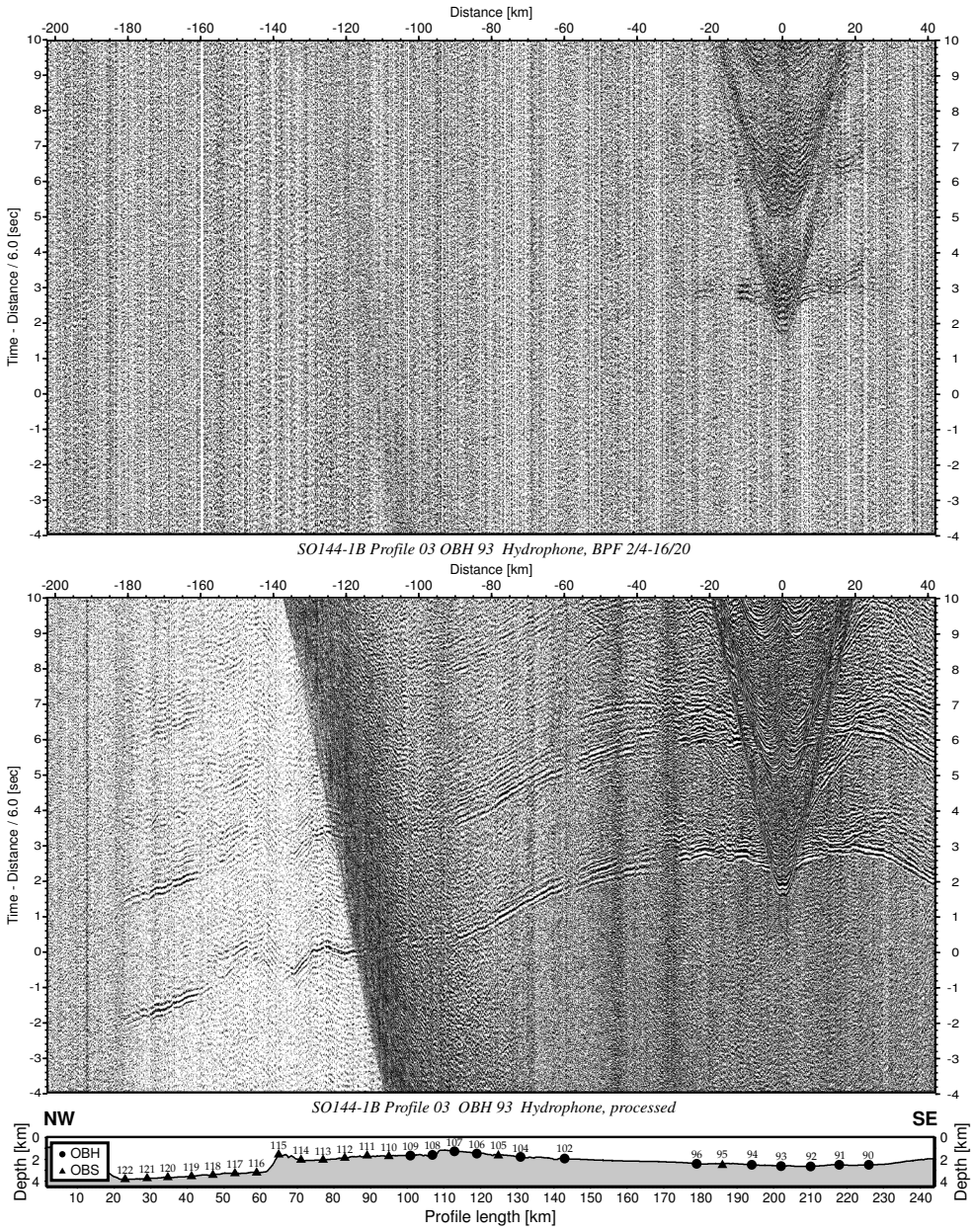


Figure 5.3: OBH 93, situated at the southeastern part of the profile. Upper image displays raw data with a bandpass filter applied. Lower image displays data after time- and offset-dependent filtering and deconvolution. The strong arrival visible between offsets of 140km to 110km is the water wave that reappears on the data due to an aliasing effect.

upper mantle, Pn, can be seen at offsets of 150km to 200km showing strong amplitudes. For the Ocean Bottom Seismometers the vertical component was used for forward modeling of the P-wave velocity-depth model because of the better data quality compared to the hydrophones. The resulting P-wave model is illustrated in Figure 5.11 and will be discussed in the following.

**P-wave velocity-depth model**

Since there is no refracted phase from the sediment observable on the data, a P-wave velocity of 1.68 to 1.7km/s was chosen for the sedimentary layer. This assumption is based on samples collected from dive sites [Lonsdale and Fornari, 1980] and on results from a vertical seismic profile at DSDP Site 504B south of the Costa Rica or Panama Rift [Swift et al., 1998b], where sediment velocities of 1586m/s for the upper 160m of sediments and 1810m/s for the lower section were found. Sediment thicknesses of several 100m were derived from reflections from the basement when available and from the onset of the refraction from the uppermost crust. Sediment thickness is highly variable throughout the profile, following the topography of the underlying basement. Beneath OBS station 113 a sedimentary basin with a maximum thickness of 1km is located, which is associated with the northwestern prolongation of the central graben as described by Lonsdale and Fornari [1980].

The uppermost crust has velocities ranging from 3.7km/s to 4.2km/s at the top and from 4.3km/s to 4.7km/s at the bottom, the lower values are found under the southeast plateau. The average thickness is about 1km, with the exception that northwest off the ridge this layer is completely missing, the basement here starts directly with the upper crust. The upper crust could be modeled with velocities of 5.0km/s at the top and 5.4km/s at the bottom with velocities remaining nearly constant along the profile. Layer thickness ranges from 1.6km to 2km underneath the ridge and is slightly thinner northwest off the ridge (1km). This layer is interpreted as layer 2B, whereas for the underlying layer 2C velocities of 6.0km/s at the top and 6.4km/s at the bottom and thicknesses of 2.0km to 2.5km to the east and 1km northwest off the ridge, fit the data best.

Thickening of the crust is nearly confined completely to the lower crust, with velocities of 6.7km/s at the top and 7.4km/s at the bottom. Whereas in the westernmost 50km of the profile the lower crust has a thickness of 3.5km, a maximum of 15km is reached underneath the central graben. On the eastern end of the profile the lower crust is thinning to 5km thickness. Velocity gradients within the lower crust change from 0.07/s to 0.001/s at a depth of 14km below basement, dividing layer 3 in two distinct layers 3A and 3B. This change in velocity gradients explains the weak but ongoing energy for the refraction from layer 3 at greater offsets.

The Moho is found at depths of 5km and 9km below basement west and east of Malpelo Ridge, respectively. It reaches its maximum depth with 20km at OBS station 110 at 100km, below the central graben. The deepening of the Moho occurs within 45km

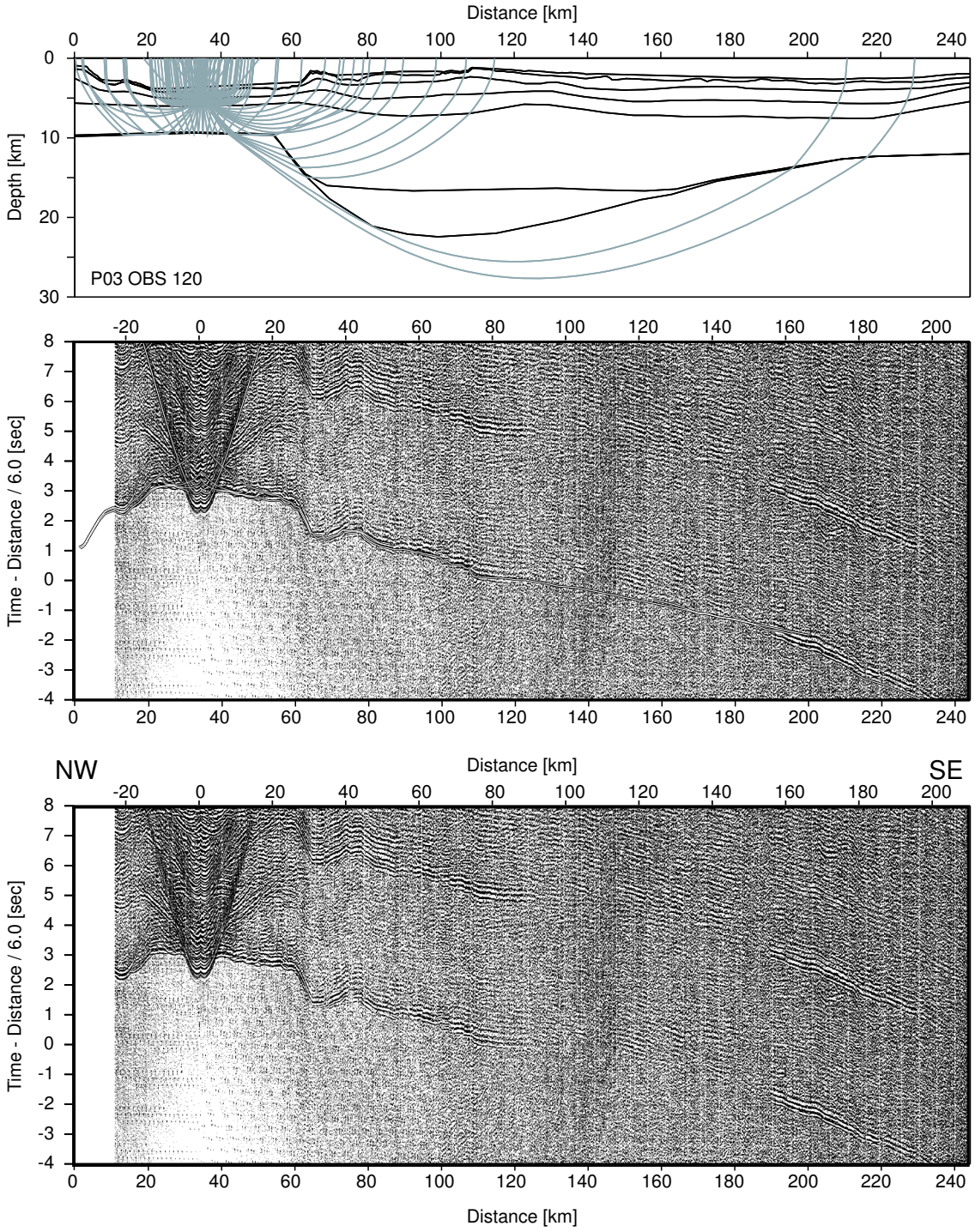


Figure 5.4: OBS 120 is located between Regina Ridge and Malpelo Ridge and is one of the three OBS situated at the northwestern end of the profile. The upper image displays the raypaths through the model subsurface as calculated through geometrical raytracing. The lower image presents the data, a reduction velocity of 6km/s is used for display. The middle image illustrates tha data with superimposed traveltimes as inferred from forward modeling.

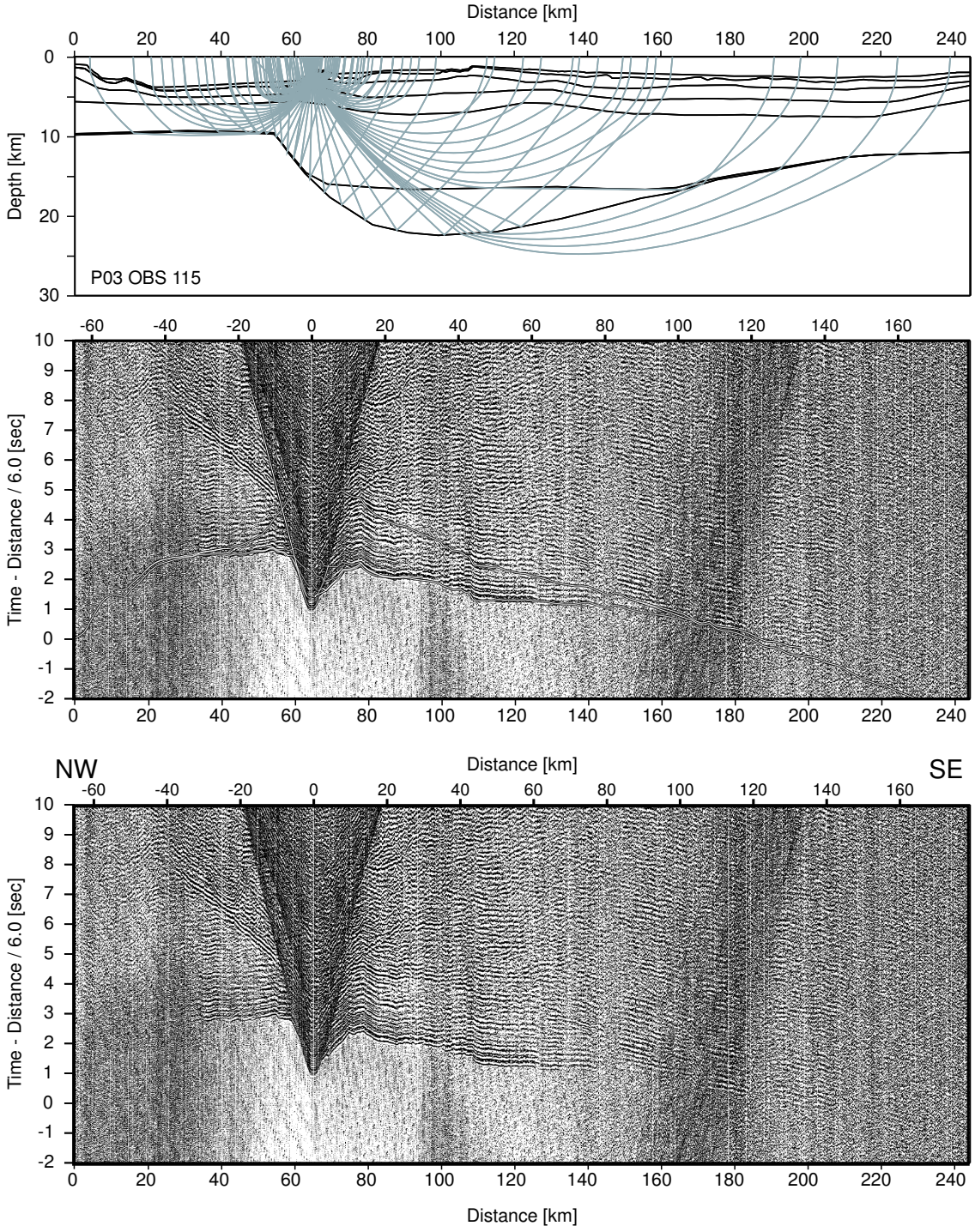


Figure 5.5: OBS 115, situated on the northwest ridge. In this area the lower crust is rapidly thickening and the Moho reaches a depth of 13km below basement.

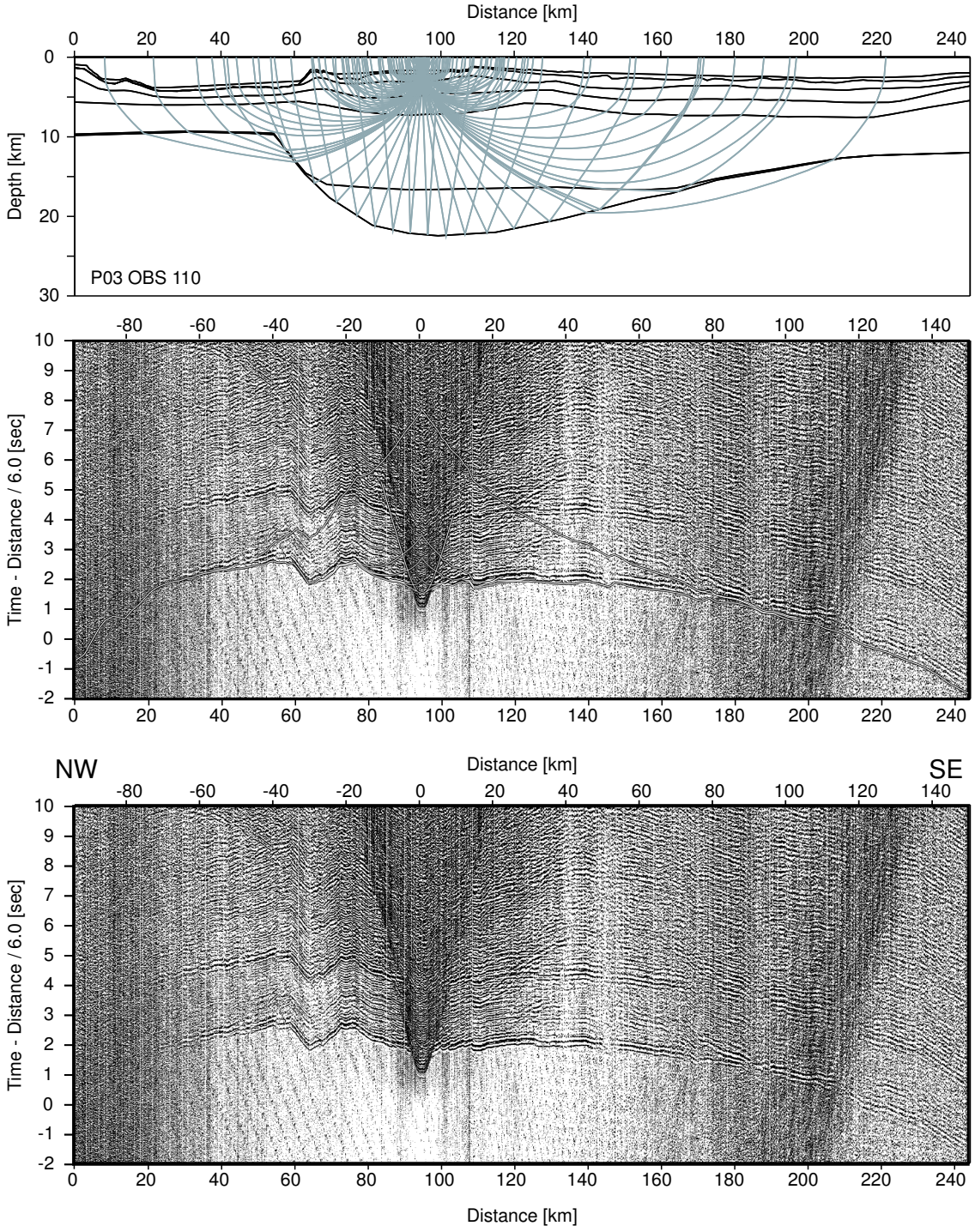


Figure 5.6: OBS 110, situated above the central graben. The Moho reaches its maximum depth of 20km below basement between OBS 112 and OBH 108.

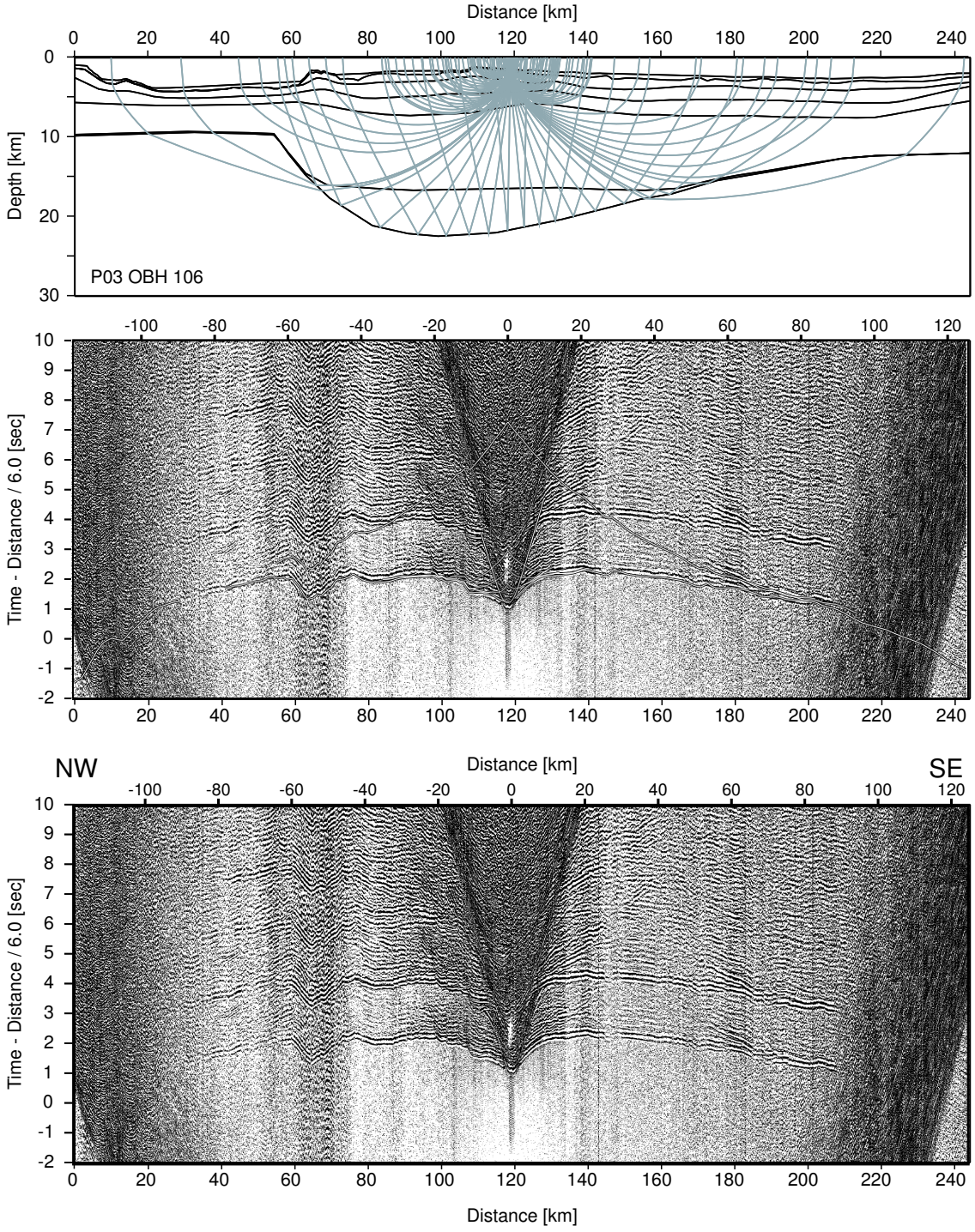


Figure 5.7: OBH 106, situated at the southeastern plateau.

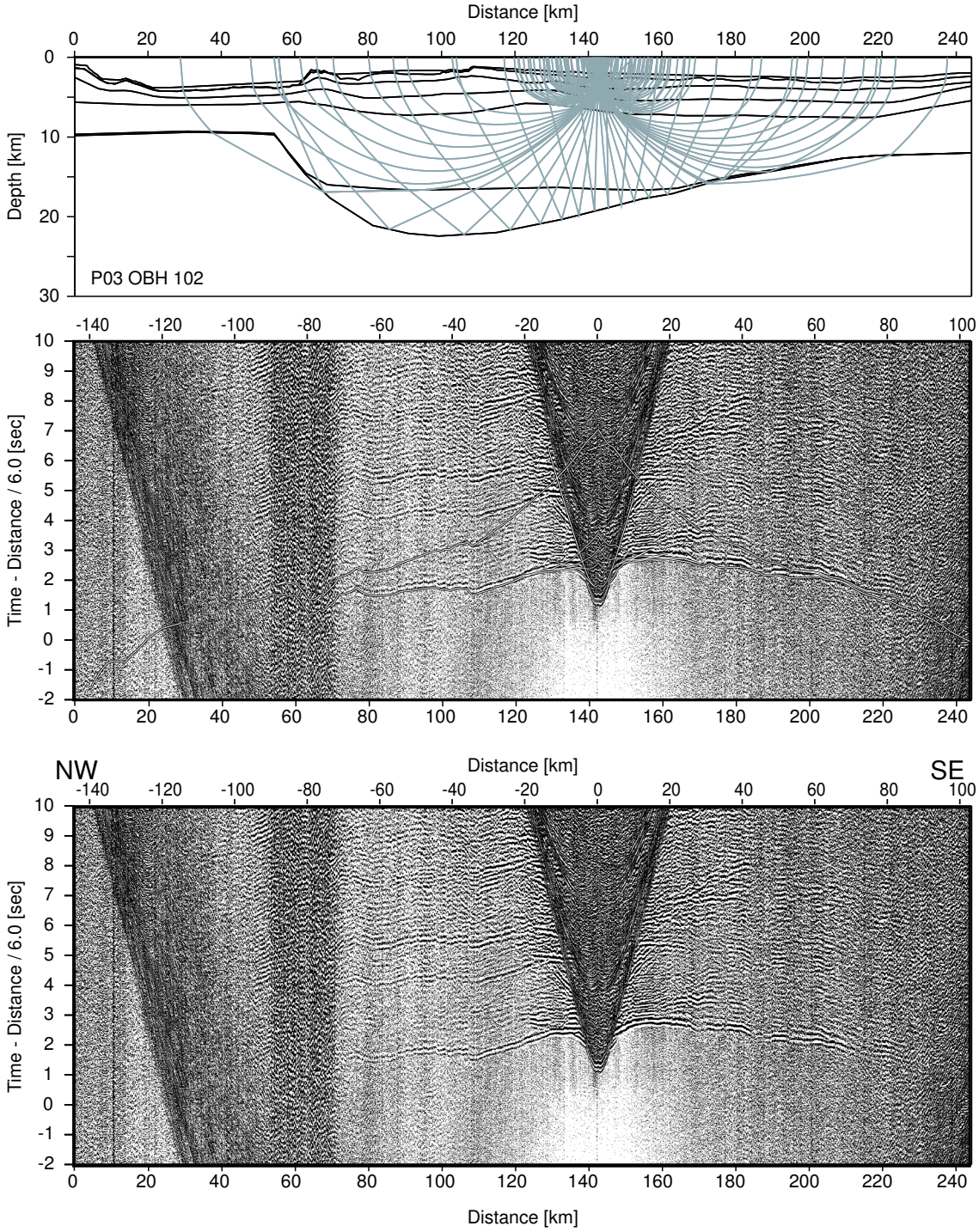


Figure 5.8: OBH 102, situated at the southeastern plateau. Thickening of the lower crust is reduced and the Moho can be found at a depth of 17km below basement.

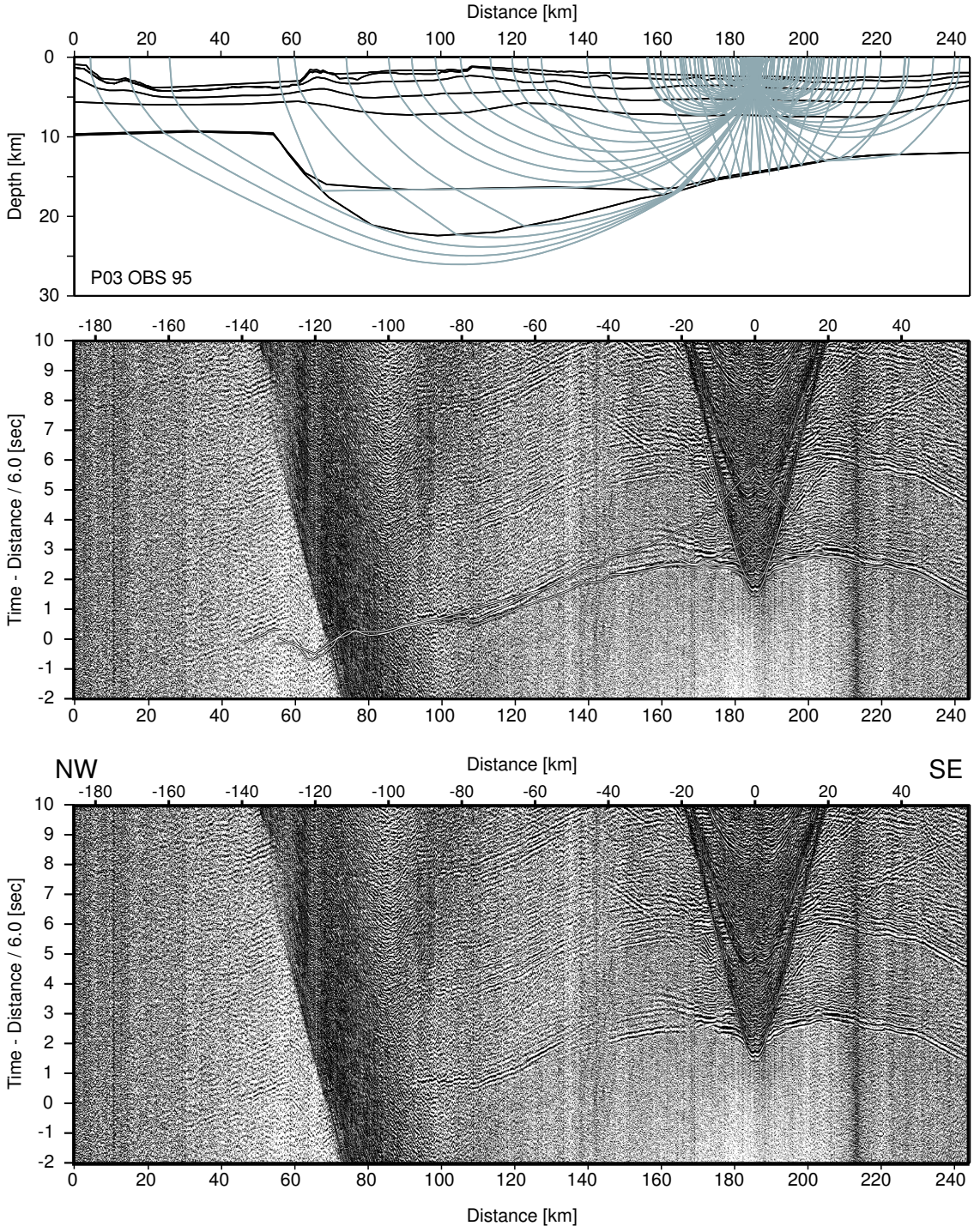


Figure 5.9: OBS 95 is located where the southeastern plateau merges gradually with the surrounding seafloor.

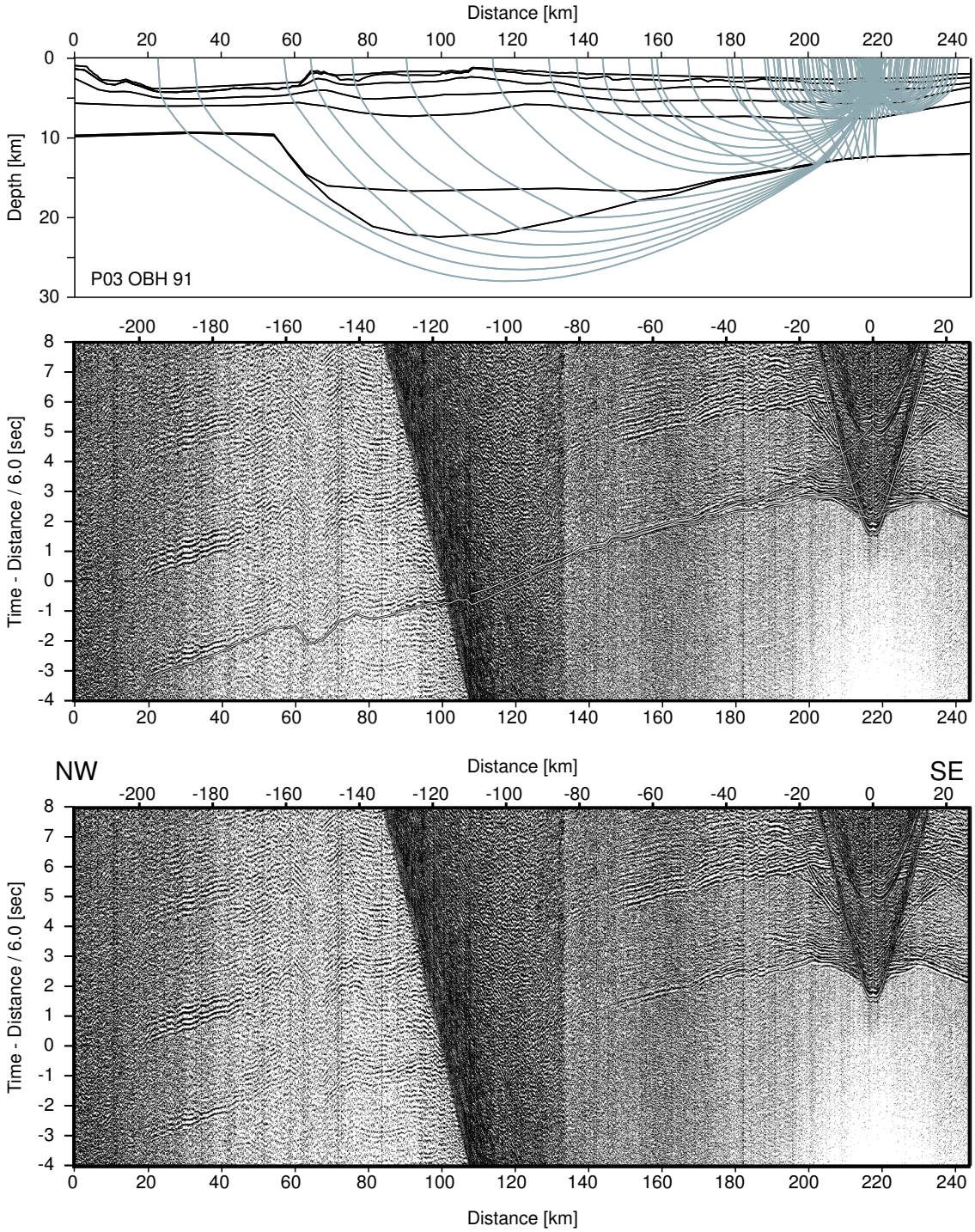


Figure 5.10: OBH 91 is located at the southeastern end of the profile where oceanic crust with a thickness of 9km is observed.

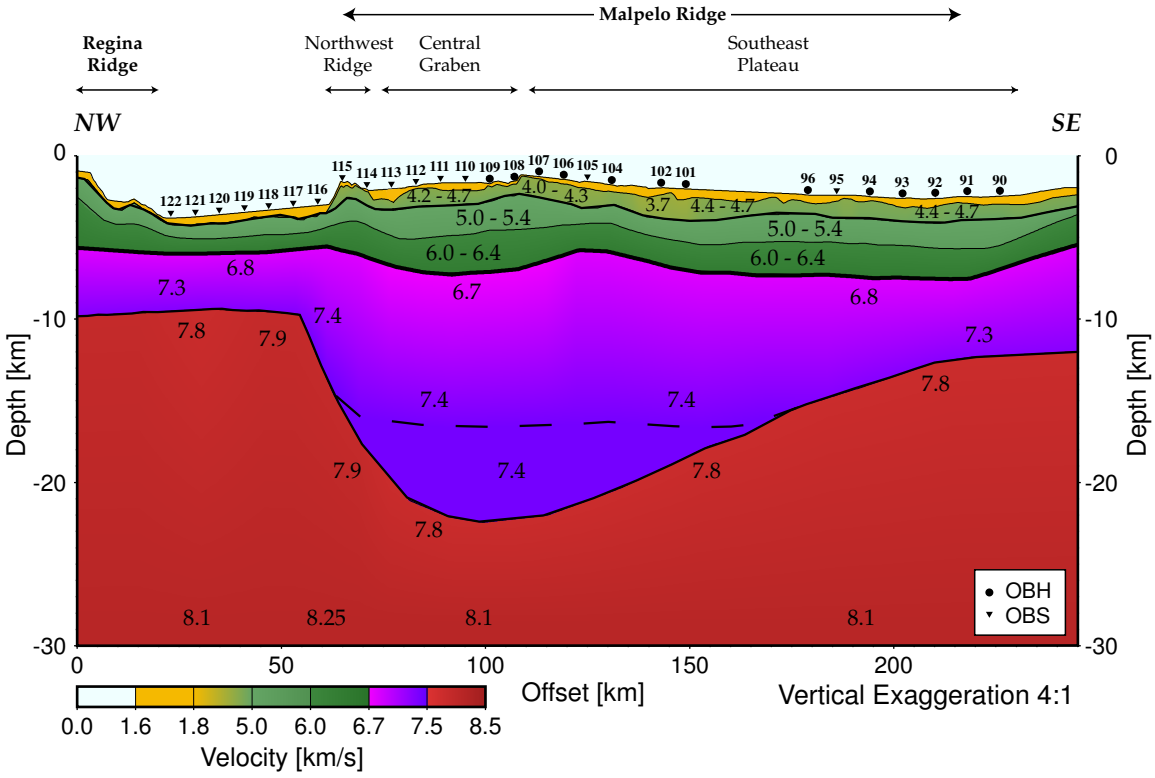


Figure 5.11: 2-D P-wave velocity versus depth model across Malpelo Ridge, Eastern Panama Basin. The dashed line indicates a change in velocity gradient.

at the northwestern margin and within 100km at the southeastern margin. Mantle velocities range from 7.8km/s to 8.1km/s and are slightly higher northwest off the ridge.

## 5.4 Shear Wave Data

One of the main reasons for the recording of shear waves with such a good quality may be that in our study area the observed topographical disturbances are small and within the order of 1/2 seismic wavelengths of the shear waves. As discussed in chapter 3 the coherency of the converted shear phases will be enhanced if the roughness of the topography is small compared to the wavelength of the affected wave modes. Another important aspect are the favorable velocity and density contrasts across the sediment/basement interface along the profile resulting in high reflectivity and transmission coefficients for the converted waves (chapter 3).

### 5.4.1 Wave Modes

In order to identify the observed shear waves the arrivals on the horizontal and vertical components were compared. Identification of different phases were verified through subsequent evaluation of particle motion. The various different wave modes identified are discussed in the following.

Figures 5.12 and 5.13 show all four components of OBS station 117, which is situated between Malpelo Ridge and Regina Ridge, at a water depth of 3270m. For better illustration purposes the data are displayed after rotation of the horizontal components into radial and transversal components and after application of filter and deconvolution parameters (chapter 5.4.2) to enhance the signal-to-noise ratio.

A reduction velocity of 4.62 km/s is used for all four components to ease identification of the shear wave arrivals. Due to this low reducing velocity the first P-wave arrival is running out of the window at an offset of 30km (denoted as P in Figure 5.12). Comparison of the vertical and hydrophone data allows identification of the water wave multiple (Pww in Figure 5.13), though, which can be seen clearly on both components with a time delay of 4.35s compared to the first P-arrival. This time delay can be calculated considering the water depth of the station.

Another arrival visible on the vertical component has the same apparent velocity as the first P-wave arrival. It has a time delay of 2.3s compared to the P-phase and is constantly shifted in time. The same arrival can also be seen on the horizontal components and is in fact the first strong arrival clearly visible on those. Since no shear wave energy is generated by airgun sources and due to the clear appearance on the horizontal components, this arrival is interpreted as a shear wave arrival. It represents a so-called PPS-wave, which gets converted at the sediment-basement interface once. The conversion takes place directly underneath the OBS after the wave has travelled through the underground as a P-wave. The PPS-phase provides useful information about the shear wave velocity of the sediment, in fact, the time delay of 2.3s between the main P-wave refraction and the PPS-phase is equal to the time difference resulting from either a P-wave or a S-wave traveling through the sediment.

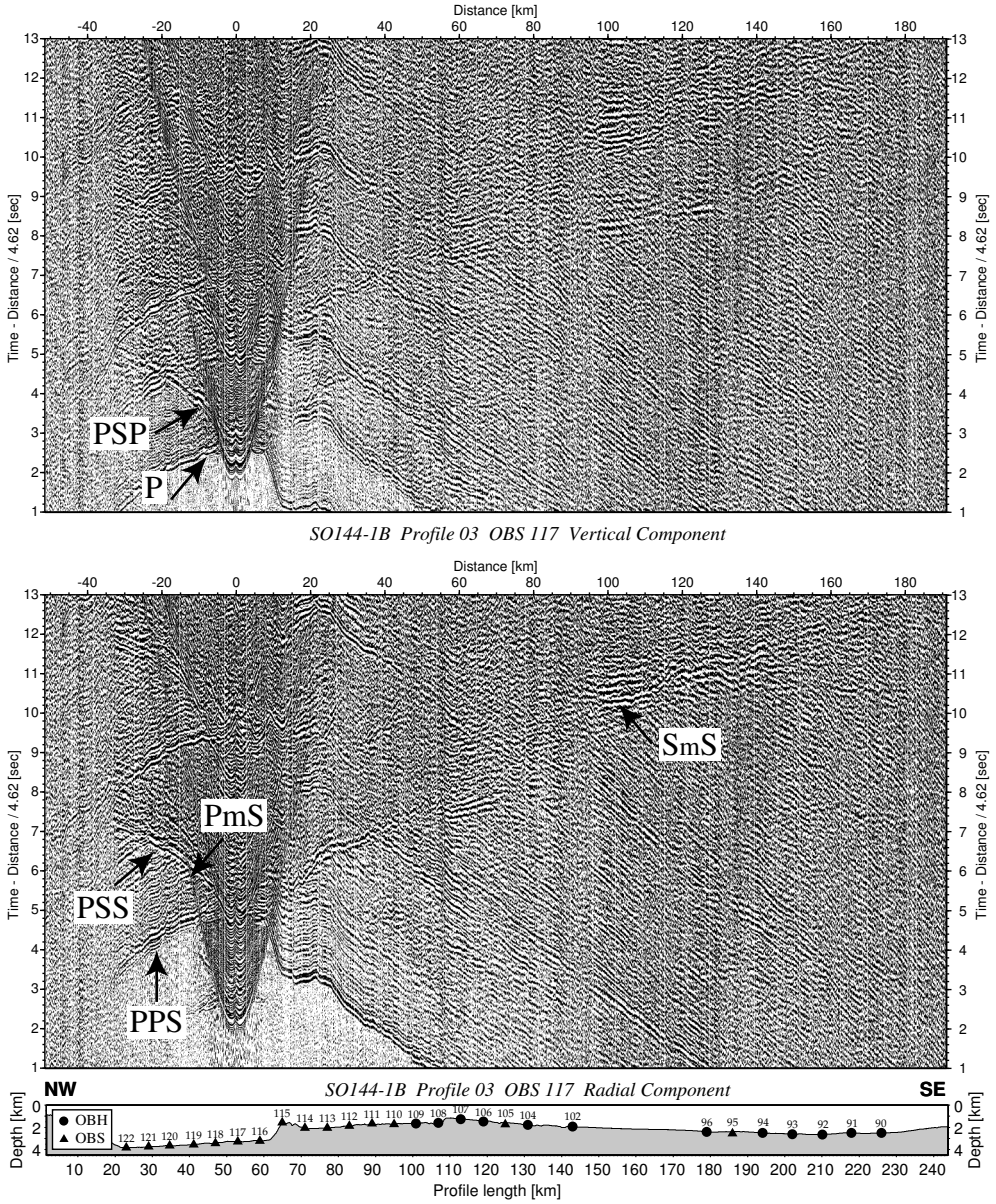


Figure 5.12: Vertical and radial component of OBS station 117. For explanation of the denoted phases please refer to the text. Arrows denote traces for which particle motion ist displayed in Figure 5.14

Another wave mode that can be seen on the vertical and hydrophone components but is hardly visible on the horizontal components is the PSP-phase. It has stronger amplitudes on the negative offsets where it can be traced until 30km offset. On the positive offsets visibility is not so clear, but the arrival can be followed to an offset of 140km. The apparent velocities are in the order of refracted shear waves. The PSP-wave gets converted underneath the shot and travels through the crust as a S-wave but undergoes a conversion back to a P-wave underneath the OBS again. Despite this double conversion there is still a measurable amount of energy of up to 36% of the incident wave energy reaching the OBS

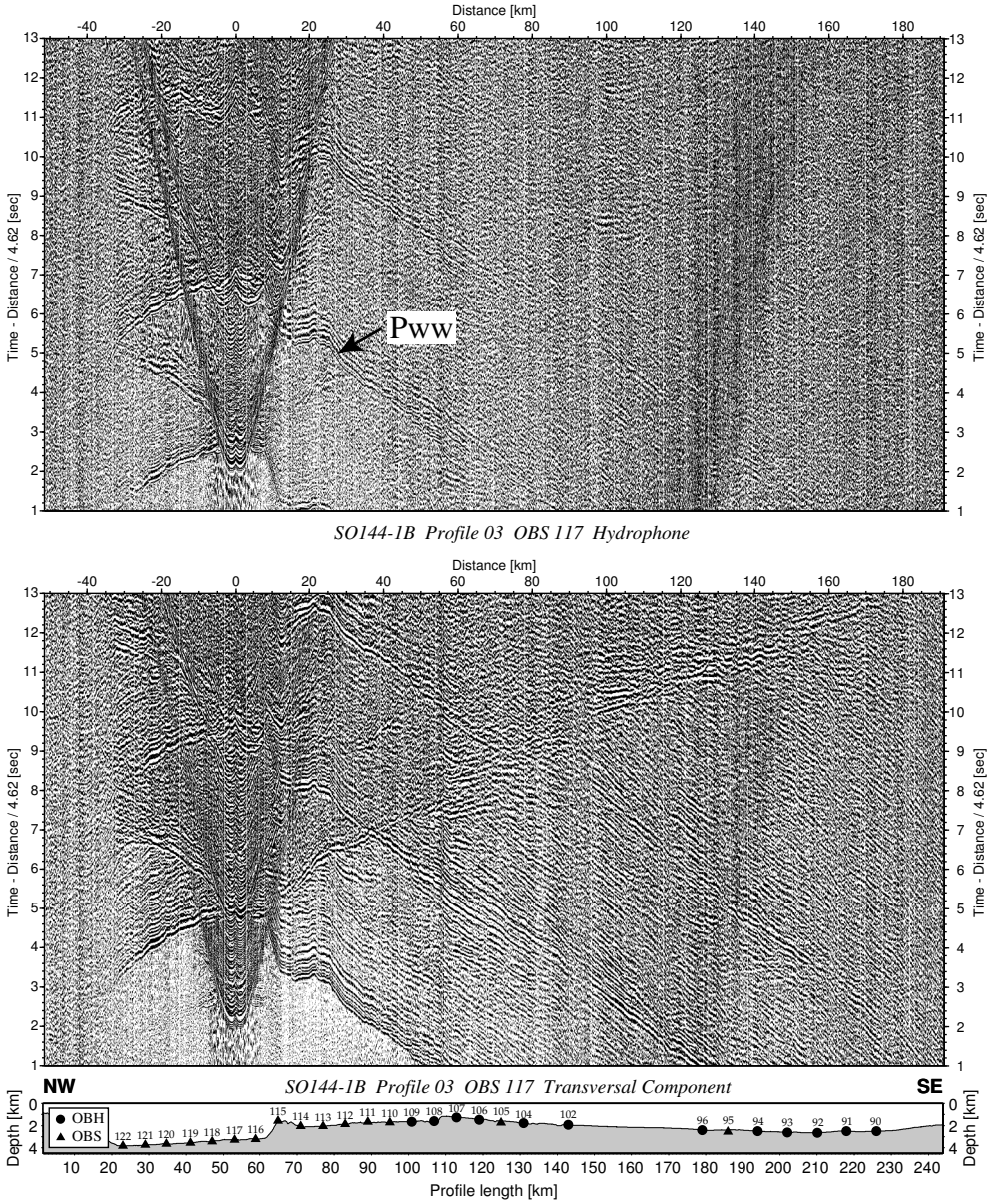


Figure 5.13: Hydrophone and transversal component of OBS station 117.

(chapter 3). As has been discussed in chapter 3 the possibility to record an SPS-phase that would travel through the sediment in S-wave mode and penetrate the crust in P-wave mode is very small and no such phase could be identified on the data.

With the same apparent velocity but constantly shifted by 2.3s a strong PSS-wave can be traced along the whole offset on the horizontal components. This phase is converted only once and travels through the crust as a S-wave. It is the main shear phase and even the SmS-reflection from the Moho is nicely recognizable between 90km and 160km offset.

A wave mode that could barely be detected although its existence was indicated through the occurrence of the SmS-phase is the PmS-reflection. Such energy should be

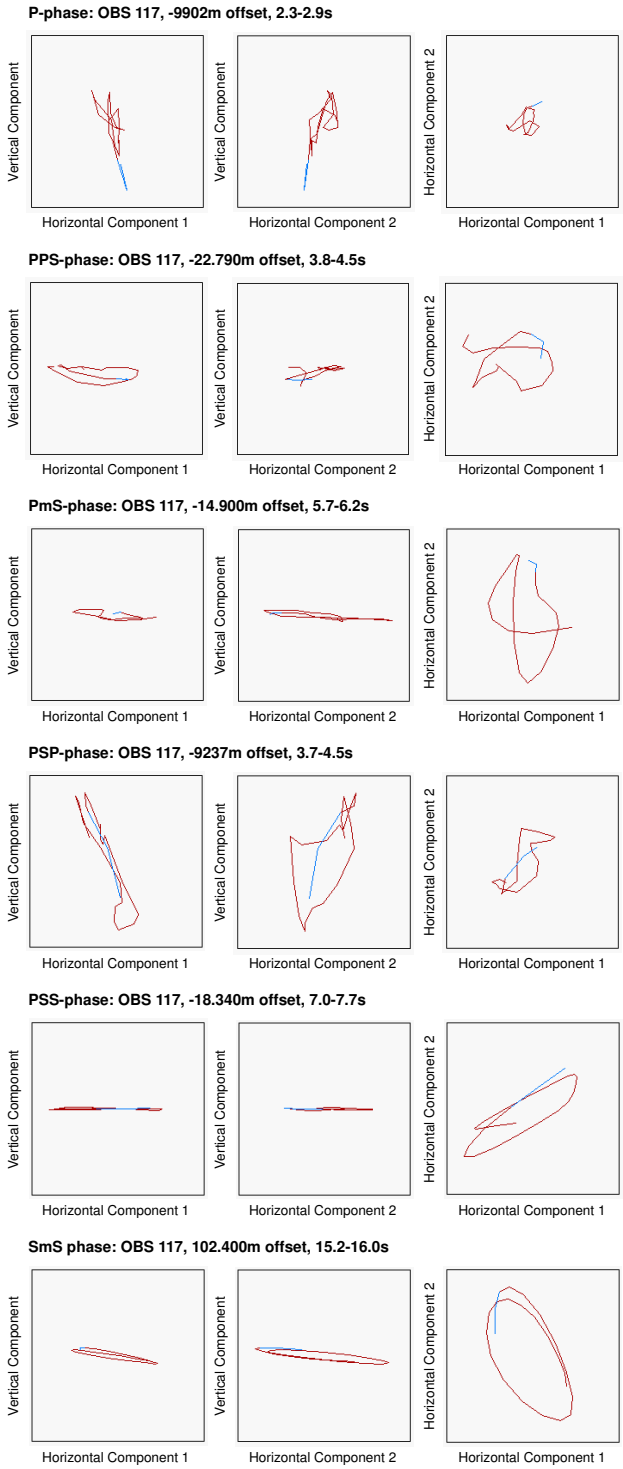


Figure 5.14: Particle motions for the identified phases as discussed in the text. Offset and time windows are calculated for record sections displayed with a reduction velocity of 4.62km/s.

detectable if the Moho is a sharp first-order velocity continuity. This wave mode gets converted at the Moho and also reaches the OBS as a S-wave. Its occurrence at a time window between the PPS-phase and the the water wave multiple of the first P-wave arrival made it difficult to identify. This was further complicated due to its apparent velocities similar to the PPS- and P-phase. The identification was finally confirmed through evaluation of particle motion. The PmS-reflection could be followed up to offsets of 30km on most stations but was difficult to distinguish from other crosscutting wave modes.

That the PPS- and PSS-phases not only occur on the horizontal components but also on the vertical component, indicates either lateral heterogeneity in the underlying basement or a tilted sediment/basement interface at the conversion point. Such a lateral heterogeneity or tilted interface can result in a similar time delay between vertically and horizontally polarized shear waves as would be caused by anisotropy. This topic is discussed in more detail in chapter 5.5.

Figure 5.14 displays plots of particle motion for the identified phases. Particle motions were studied on bandpass filtered and amplitude normalized data after rotation and prior to processing and were used to verify identification of phases. For the P-phase motion is dominantly vertically as would be expected. Its small horizontal component may be due to sub-surface dip of a few degrees or heterogeneities in the velocity structure of the sediment or basement. Particle motion for the PSP-phase resembles that for the P-phase, its stronger complexity is interpreted as a result of interference with reverberations and other converted wave modes. Motion plots for the PPS-, PSS-, PmS-, and SmS-phases show dominantly horizontally motion and hence confirm their interpretation as converted S-wave modes.

### 5.4.2 Data Processing

Data processing included relocation of the instrument position by analyzing the direct arrivals. The rotation of the horizontal components of the OBS into the source-receiver plane as well as a predicitive deconvolution and a time and offset dependent frequency filter are described in the following.

#### Rotation

The Ocean Bottom Seismometers that were used in this study consisted of three geophones mounted perpendicular to each other and an additional hydrophone. The OBS were not equipped with any gyrometric system though, which means that the orientation of the horizontal components was not known beforehand. An estimation of their orientation can be achieved using the data itself, utilising the polarity of the horizontal components. For this purpose the direct water wave arrival is usually chosen since it is not affected by lateral inhomogeneities and has adequate amplitudes for a reliable calculation.

The computation of the orientation from the data is a common processing step in shear

wave processing. It takes advantage of the fact that the water wave is linearly polarized in the source-receiver plane. In more detail for a compressional wave energy source the direction of particle motion will be parallel to the direct arrival ray path. The analysis of the power in a window which includes the first break therefore permits the calculation of the orientation angle relative to a fixed coordinate system.

Knowledge of the orientation of the horizontal geophones allows their rotation into the source-receiver plane, which is an important step for further analysis regarding e.g. shear wave splitting and estimation of anisotropy. The rotation itself is equivalent to rotating the coordinate axes in space and is accomplished through projection of the data onto new coordinate axes. The two horizontal components are then lying in the direction of the direct arrival and perpendicular to it and are called radial and transversal component, respectively. The transverse component is considered to record predominantly horizontally polarized $S_H$-waves and the radial component is considered to record mainly vertically polarized $S_V$-waves. Since conversion of an incident P-wave at a horizontal interface generates only transmitted and reflected P-waves and $S_V$-waves the main shear wave energy is expected to be on the radial component.

Mathematically the coordinate transform that performs a rotation of the horizontal components $H1$ and $H2$ around an angle $\alpha$ into the radial ($R$) and transversal component ($T$) is written as:

$$\begin{aligned} V &= V \\ R &= H_1 * \cos\alpha + H_2 * \sin\alpha \\ T &= -H_1 * \sin\alpha + H_2 * \cos\alpha \end{aligned} \tag{5.1}$$

$V$ denotes the vertical component in Equation 5.1. The axis of rotation is the vertical axis, its orientation is assumed to be and remain vertical for gimbal-mounted geophones (Figure 5.15).

Orientation analysis and rotation was performed using SEISMOS, which provides special modules for analyses of this kind. The water wave was mathematically straightened and its onset shifted to 1.0s using Equation 5.2 to allow picking of a fixed time window for analysis. Symbols are denoted as follows: calculated time ($t_{calc}$), time ($t$), offset ($x$), waterdepth of the OBS ($z$), water velocity ($v_w$).

$$t_{calc}[s] = t - \sqrt{(\frac{z}{v_w})^2 + (\frac{x}{v_w})^2} + 1 \tag{5.2}$$

Figure 5.16 is an example of this straightened water wave, showing an offset from -15km to 15km. The fact that geophones record the wave field depending on direction leads to a so-called ”polarity flip” on the horizontal components with change from positive to negative offsets and vice versa. This effect can be seen clearly on both components in Figure 5.16 between 1.0s and 1.5s. Due to the large impact of the airgun for shots

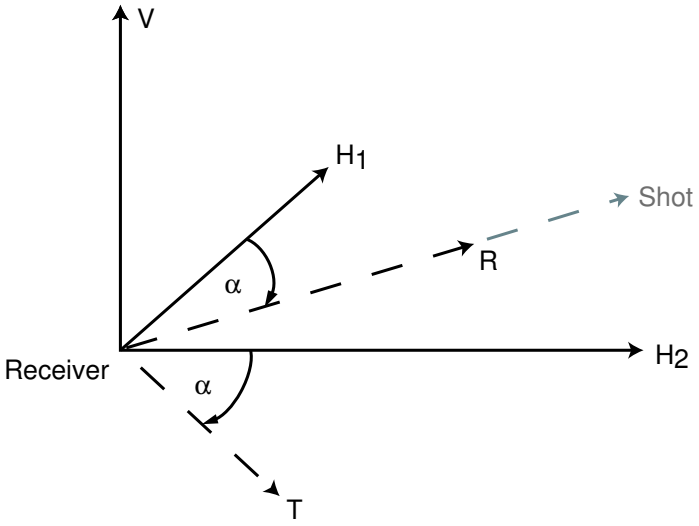


Figure 5.15: Rotation of the horizontal components into the source-receiver plane. The following denotation is used: $H_1$, horizontal component 1; $H_2$, Horizontal component 2; V, Vertical component; R, Radial component; T, Transversal component; $\alpha$, rotation angle.

that were fired directly above the station the traces within the first $\pm$1km offset have skipped amplitudes and do not show any polarity flip. Therefore and to allow better direct comparison of negative and positive offsets the first $\pm$1km are cut out in the plots. Figure 5.17 shows the same detail as Figure 5.16 but after rotating the data by the calculated angle. Since all traces for the now radial and transversal components are rotated into the source-receiver direction and its perpendicular counterpart, respectively, the effect of flipping polarity with positive and negative offsets has been removed.

For the calculation of the rotation angle discrete windowed trace areas with a length of 70ms to 130ms were chosen, depending on data quality at different stations. Since the analysis results are strongly affected by noise contamination, the time window must be carefully chosen. For orientations using the direct water wave arrival wavelet the time window recommended includes exactly the first complete period. The rotation angles could be calculated with an accuracy of $\pm$3 degrees. The most plausible cause for inaccuracies are noise contamination and shallow reflections that are crosscutting the water wave, especially for those stations deployed at less water depth. Another important factor regarding the accuracy of the orientation/rotation angle are phase and frequency characteristics of the horizontal geophones, this also includes that the data are input to orientation analysis prior to any filtering steps.

After rotation of all OBS record sections it was discovered that the transversal component still contained the same amount of shear wave energy as the radial component. This high signal-to-noise ratio on the transversal component implicates that appreciable $S_H$ energy was generated by mode conversion either at the sediment/basement interface or due to heterogeneities in the subsurface. In this context it has to be noted that the terms $S_V$ and $S_H$ are only defined for the two-dimensional case and that the radial and transversal

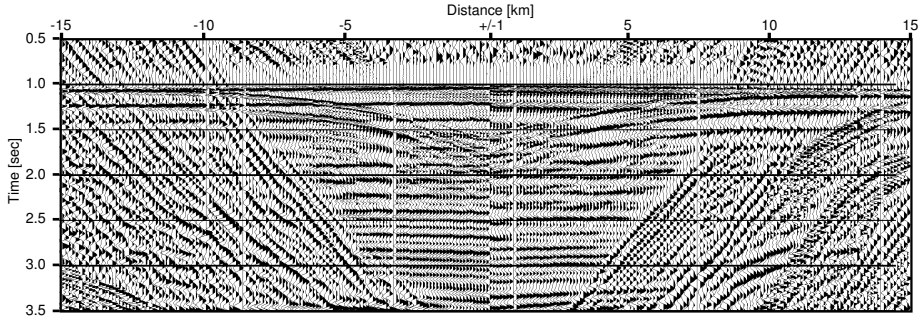


*SO144-1B Profile 03 OBS 117 Horizontal Component 1*

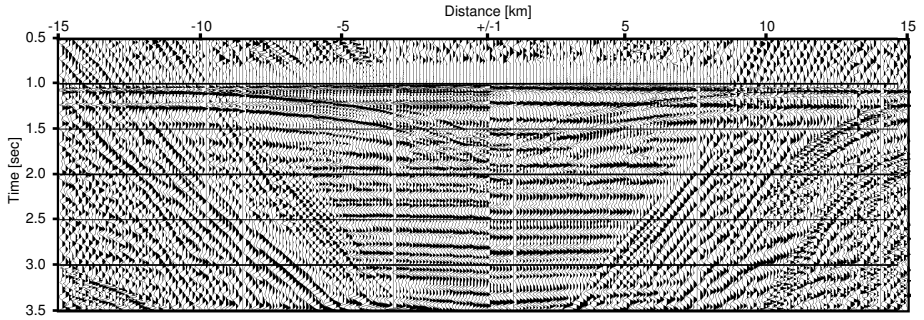


*SO144-1B Profile 03 OBS 117 Horizontal Component 2*

Figure 5.16: Horizontal components of OBS station 117 as input to orientation analysis, before rotation. Time is calculated as given in equation 5.2.

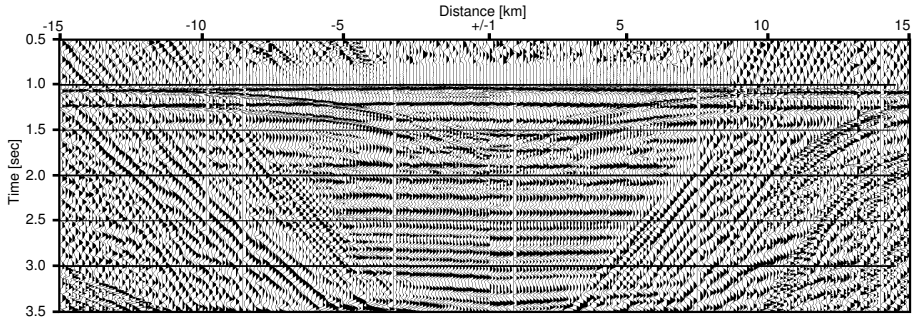


*SO144-1B Profile 03 OBS 117 Radial Component*

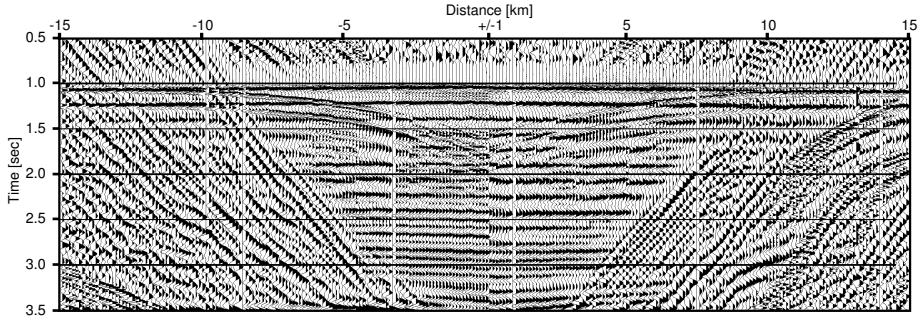


*SO144-1B Profile 03 OBS 117 Transversal Component*

Figure 5.17: Radial and transversal components of OBS station 117, after rotation. Time is calculated as given in equation 5.2.

| offset [km] | time [sec] | lower stop/pass | upper stop/pass |
|---|---|---|---|
| 0 | 1 | 2/4 | 18/24 |
| | 3 | 2/4 | 15/20 |
| | 5 | 2/4 | 12/18 |
| | 8+ | 2/4 | 10/18 |
| 10 | 1 | 2/4 | 18/24 |
| | 3 | 2/4 | 15/20 |
| | 5 | 2/4 | 12/18 |
| | 8+ | 2/4 | 10/18 |
| 20 | 1 | 2/4 | 15/20 |
| | 4 | 2/4 | 12/18 |
| | 7+ | 2/4 | 10/18 |
| 40 | 1 | 2/4 | 12/18 |
| | 5+ | 2/4 | 10/18 |
| 70+ | 1+ | 2/4 | 10/18 |

Table 5.3: Offset and time dependent filter parameters applied to shear wave data.

components can only be considered to record $S_V$- and $S_H$-waves in the absence of three-dimensional structure. The occurrence of shear wave energy on the transversal component therefore indicates three-dimensional complexity within the crust or near the surface [Holbrook et al., 1988]. At DSDP Site 504B scattered shear waves recorded during a VSP survey underlined an observation of Stephen [1988] that the top of the ocean crust is not laterally homogenous on length scales of 100-500m [Swift et al., 1998c].

**Filtering and Deconvolution**

To take the varying frequency content of compressional and shear waves into account, different filter and deconvolution parameters were tested and determined for the horizontal components and for the vertical component and hydrophone data (chapter 5.3.1). Filter parameters were applied on time reduced record sections with a reducing velocity of 3.465km/s for the horizontal sections and are given in Table 5.3.

As for the compressional wave data a predictive deconvolution was applied to further improve temporal resolution. Gate lengths were 3000ms gradually increasing by 1000ms , the last gate had a gate length of 6000ms. The overlap region and merging region had lengths of 1000ms. Parameters are printed in Table 5.4, raw and processed data for OBS station 119 are displayed in Figure 5.18. In the following all shear wave record sections are displayed with a reduction velocity of $\frac{6.0}{\sqrt{3}} = 3.465km/s$. This time reduction corresponds to a reduction velocity of 6.0km/s for the P-wave sections, and for a Poisson's ratio of 0.25 in the crust and upper mantle, arrivals on the P-wave record sections will be easily comparable to the corresponding S-wave arrivals. When the time axis for the

S-wave record sections is compressed by the same factor, corresponding arrivals would perfectly overlay each other.

| Component Type | Operator Length [ms] | Prediction Lag [ms] | Prewhitening [%] |
|---|---|---|---|
| S-wave | 324 | 24 | 0.1 |

Table 5.4: Parameters for predictive deconvolution of shear wave data.

### 5.4.3 Modeling

The program MACRAY [Luetgert, 1992] that was used for forward modeling also permits ray tracing of converted waves and one or more layers at which the conversion takes place can be chosen. For modeling of shear wave velocities the velocity model obtained through forward modeling of the P-wave data was used as a starting model (Figure 5.11). Obviously the quality and accuracy of the P-wave velocity model has a strong influence on the resulting S-wave model (Figure 5.35). During modeling of the shear wave velocities, interfaces were kept fixed and only velocity values were altered in a trial and error approach. This method requires that compressional and shear waves traveling through the crust and mantle get refracted and reflected at the same interfaces. In more detail, it is assumed that P- and S-waves react to the same velocity and density contrasts or, in other words, that a velocity or density contrast that acts as an interface for a P-wave is also strong enough to influence a S-wave and vice versa.

For the northwestern half of the profile (OBS 122 to 110) all different wave modes as described in chapter 5.4.1 were considered in the modeling process. For the rest of the profile (OBH 109 to 90) only PSP wave modes were available for evaluation of S-wave velocities, resulting in a lower accuracy for this part of the profile.

The modeling process was started with the PPS wave mode to constrain the shear wave velocity of the sedimentary layer. This wave mode is traveling through the sediment and basement as a P-wave and gets converted to a S-wave directly underneath the OBS and is then recorded as a S-wave mode. Its time delay to the normal P-wave mode is directly related to the difference in P- and S-wave velocity of the sediment section underlying the recording OBS station. Identification of the PPS phases could be performed with an accuracy of about $\pm$80ms. Since the onset of all arriving converted phases is not as sharp as for the first P-wave arrival, picking errors for the converted phases are higher. The PPS-phases are obscured by other phases, e.g. the P-wave and PSS-wave arrivals. Figure 5.19 presents traveltime picks for the P- and PPS-wave modes as well as traveltimes inferred from forward modeling for OBS station 118. In Figure 5.20 an error evaluation is illustrated: At OBS station 118 a change in shear wave velocity of $22\%$ or 0.05km/s results in a traveltime error of 170ms. The overall accuracy for shear wave velocities of the sedimentary layer is 0.04km/s. It has to be stated, though, that the accuracy for

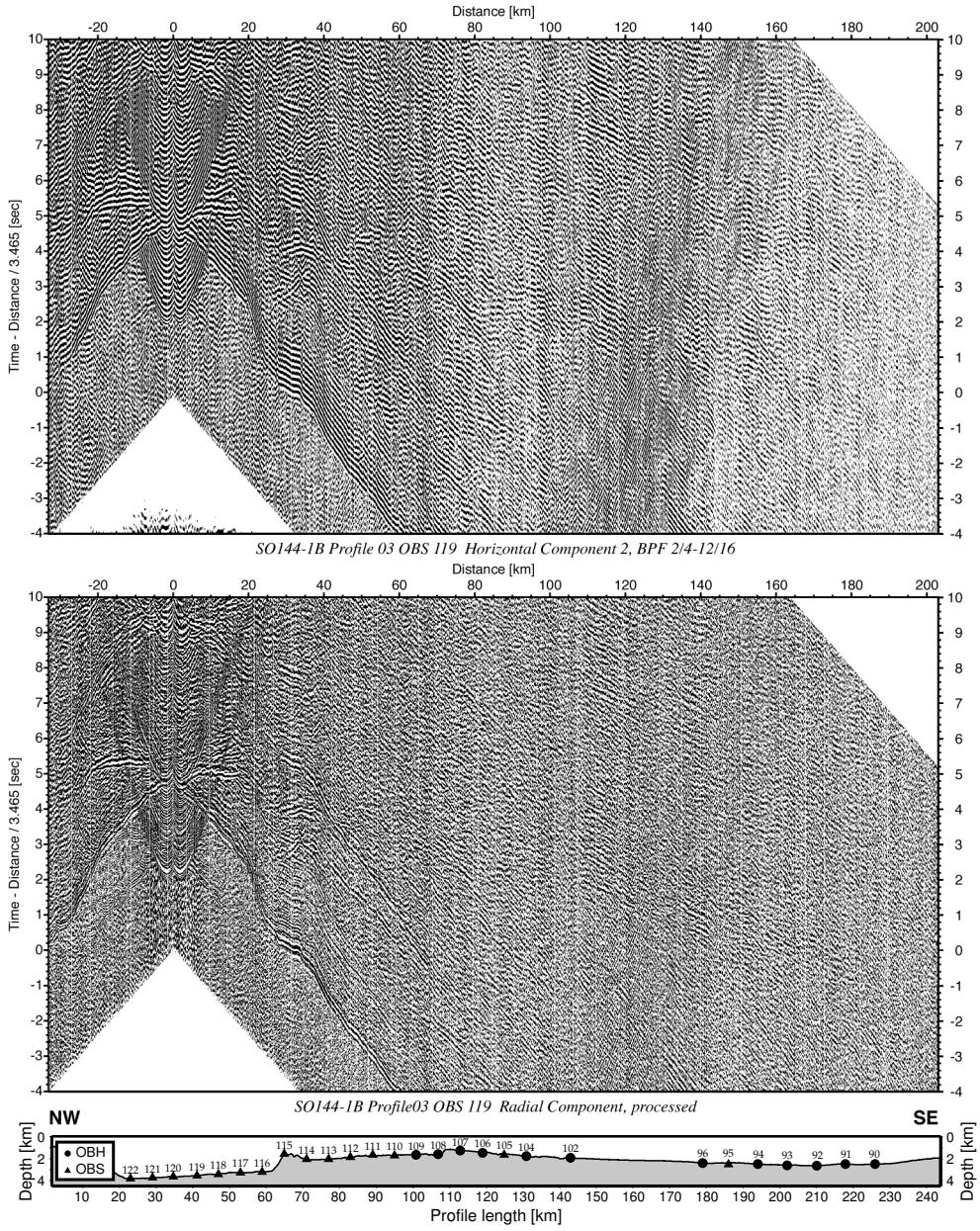


Figure 5.18: OBS119, situated at the northwestern part of the profile. Upper image displays raw data with a bandpass filter applied. Lower image displays data after rotation and time- and offset-dependent filtering and deconvolution.

the S-wave velocities of the sedimentary layer depends strongly on the correct sediment thickness. A change in sediment thickness of 60m results in the same traveltime error of 170ms as illustrated in the example above.

The PSS modes were the main phases for modeling of the shear wave velocities in crust and upper mantle. The events are clear and continuous but partly obscured by mul-

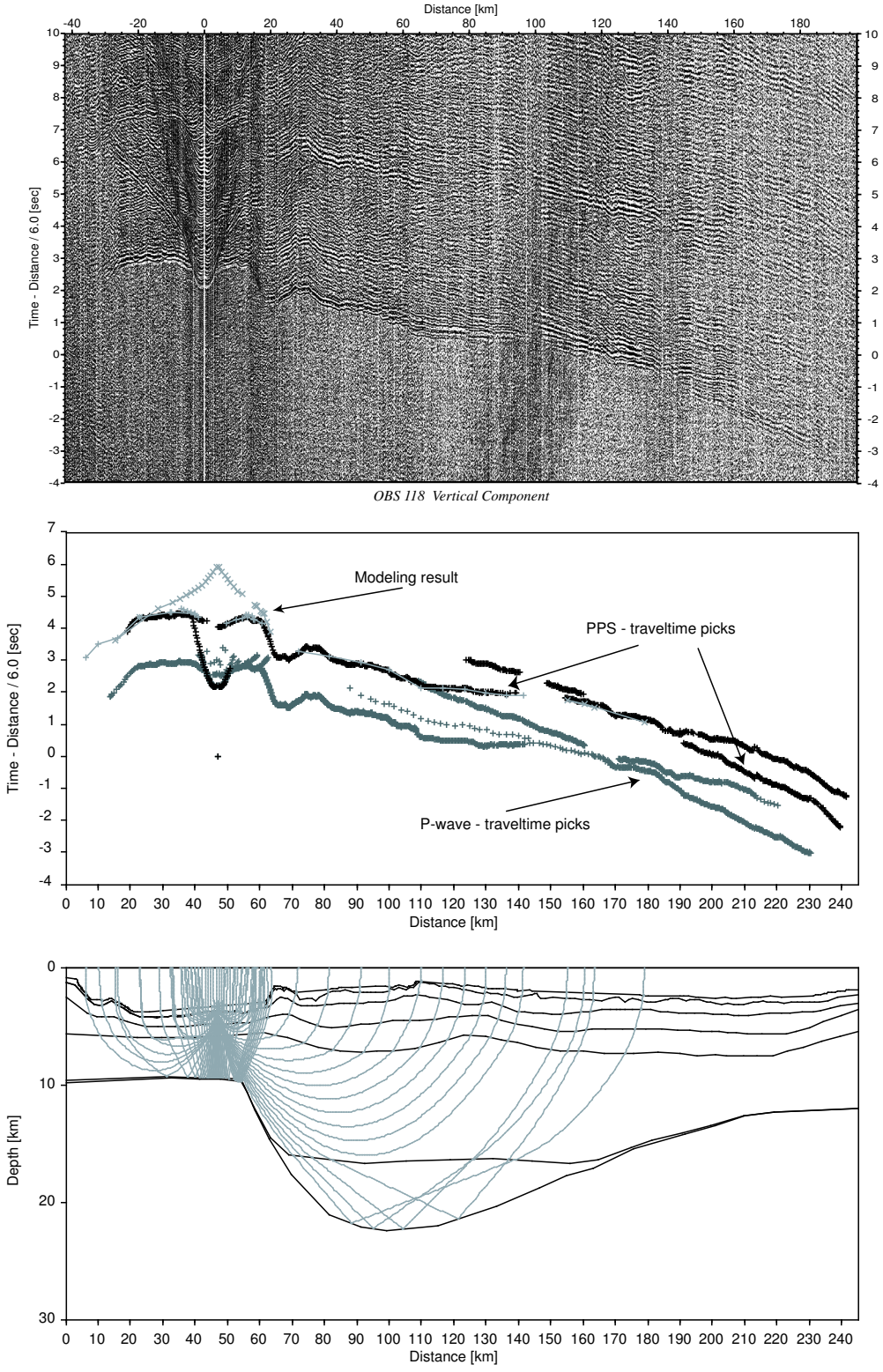


Figure 5.19: OBS 118, situated between Regina Ridge and Malpelo Ridge at the north-western end of the profile. The upper image displays the data, a reduction velocity of 6.0km/s is used for display. The middle image illustrates the picked PPS traveltimes in black overlain by the traveltimes inferred from forward modeling in light grey (solid lines). For comparison the P-wave traveltime picks are shown in grey.

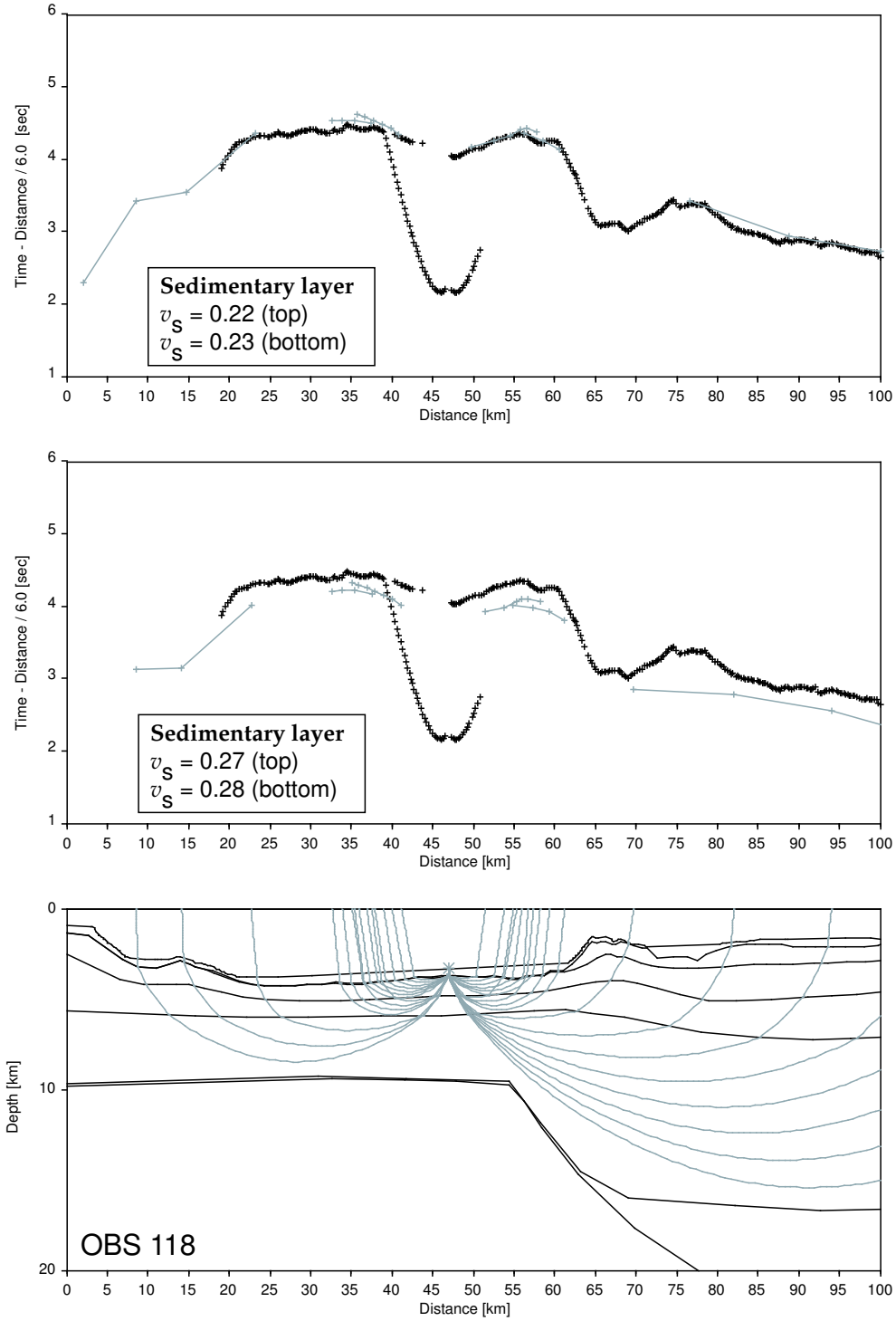


Figure 5.20: Error evaluation for OBS station 118. The upper image displays the PPS traveltime picks overlain by traveltimes inferred from forward modeling. The shear wave velocity underneath the OBS ranges from 0.22km/s at the top to 0.23km/s at the bottom of the sedimentary layer. Changing the velocities by $22\%$ or 0.05km/s results in a traveltime error of 170ms (middle image). The model with the raypaths of converted PPS wave modes is shown in the lower image.

tiples and other phases, resulting in a lower picking accuracy of up to $\pm$100ms. Figures 5.21 to 5.27 display record sections and traveltimes inferred from forward modeling of OBS stations 122, 120, 118, 116, 114, 112 and 110. The incident P-wave was modeled to convert at the sediment/basement interface traveling through the basement and crustal layers and reaching the OBS as a S-wave. Figure 5.28 depicts traveltime errors for the lower crust and upper mantle: Changing the velocity in the upper mantle by $5\%$ or 0.2km/s and leaving the velocities in the crust unchanged results in a traveltime error of 250ms for the refraction from the upper mantle. A change in the velocity in the lower crust by $5\%$ or 0.2km/s results in a traveltime error of up to 900ms for the refraction from the lower crust. Taking the picking error into account additionally, the overall accuracy for the shear wave velocities is 0.2km/s.

In the southeastern part of the profile, where no 4-component data were available, only PSP modes constrained the modeled values. Traveling though the crust and mantle as S-waves but being converted back to a P-wave at the sediment/basement interface underneath the OBS, they are recorded as P-waves and therefore appear on the hydrophone and vertical component. Due to the double conversion amplitudes are not as strong and the signal becomes rapidly weak with increasing offset. A traveltime error of about $\pm$150ms was encountered during identification of the PSP-phases. This results in a lower overall accuracy for the velocities derived from the PSP-phases of about 0.3km/s.

Nevertheless modeling of the PSP-phases confirmed velocities derived from the PSS modes very nicely in the northwestern part of the profile and also strongly contributed to the resulting velocity-depth model where no horizontal components were available.

In Figures 5.29 to 5.34 hydrophone record sections and the calculated traveltimes derived from forward modeling of the PSP-phases are illustrated.

**S-wave velocity-depth model**

The resulting S-wave velocity-depth model is illustrated in Figure 5.35.Shear wave velocities for the sedimentary layer are variable, ranging from 0.15m/s to 1km/s. They are directly related to consolidation and compaction of the sediment and are comparable to published data from Hamilton [1971, 1976].

In the uppermost crust velocities of 1.9km/s to 2.2km/s were found at the top and of 2.1km/s to 2.5km/s at the bottom, respectively. Velocity tends to be lower underneath the central graben and higher in direction of the southeastern end of the profile.The upper crust shows higher velocities below the central graben and southeast plateau (2.7km/s at the top and 3.0km/s at the bottom) and slightly lower velocities (2.6km/s at the top and 2.9km/s at the bottom) west and east off the ridge. In layer 2C velocity values are varying from 3.3km/s at the top to 3.6km/s at the bottom below the central graben and 3.4km/s at the top to 3.7km/s at the bottom at the western and eastern ends of the profile.

Lower crustal velocities range from 3.8km/s at the top to 4.1km/s at the bottom, also encountering a change in velocity gradient as for the compressional wave velocities (chap-

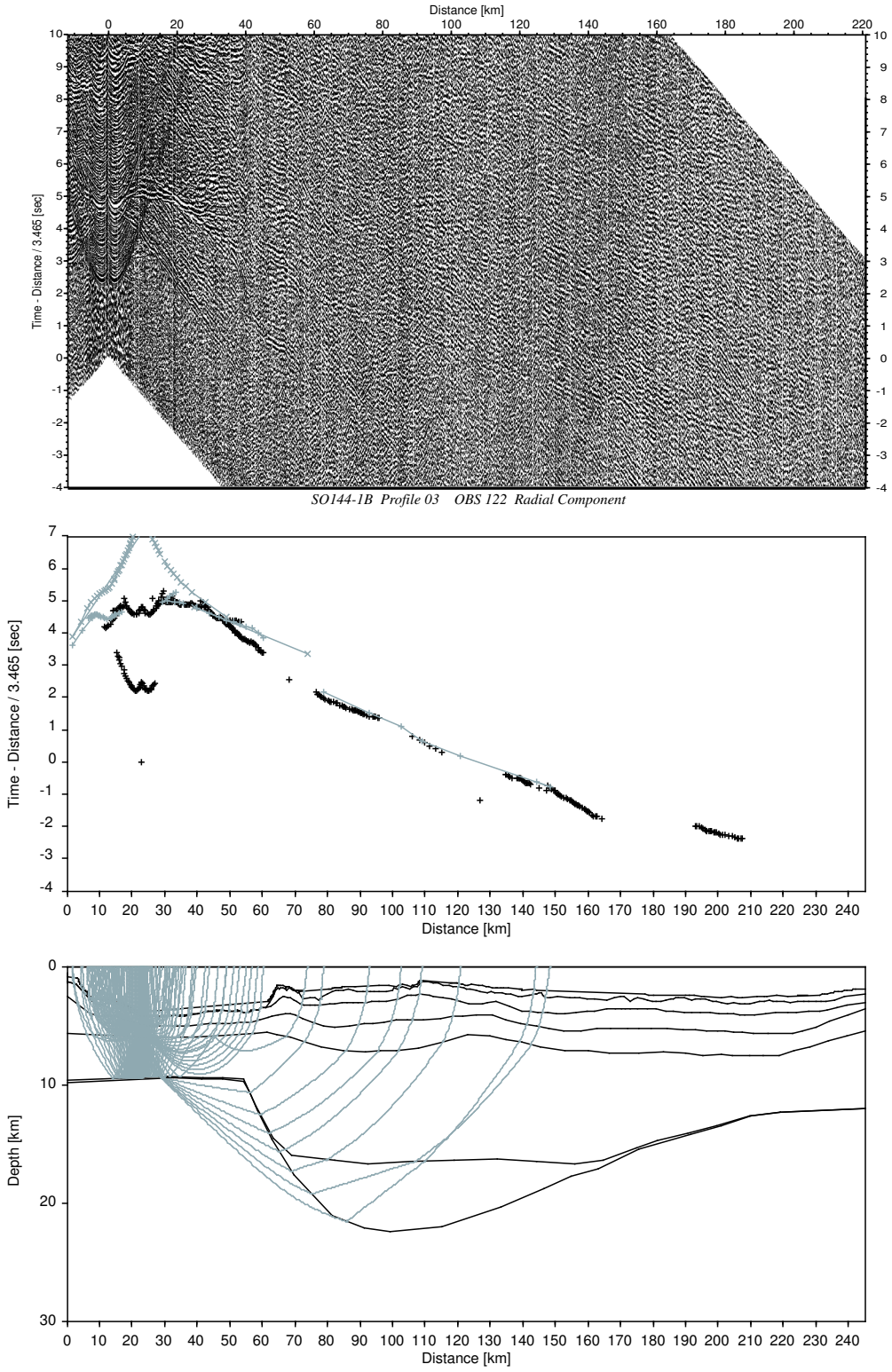


Figure 5.21: OBS 122 is located between Regina Ridge and Malpelo Ridge at the northwestern end of the profile. The upper image displays the data, a reduction velocity of 3.465km/s is used for display. The middle image illustrates the picked traveltimes in black overlain by the traveltimes inferred from forward modeling in grey (solid lines). The lower image shows the converted raypaths through the model subsurface.

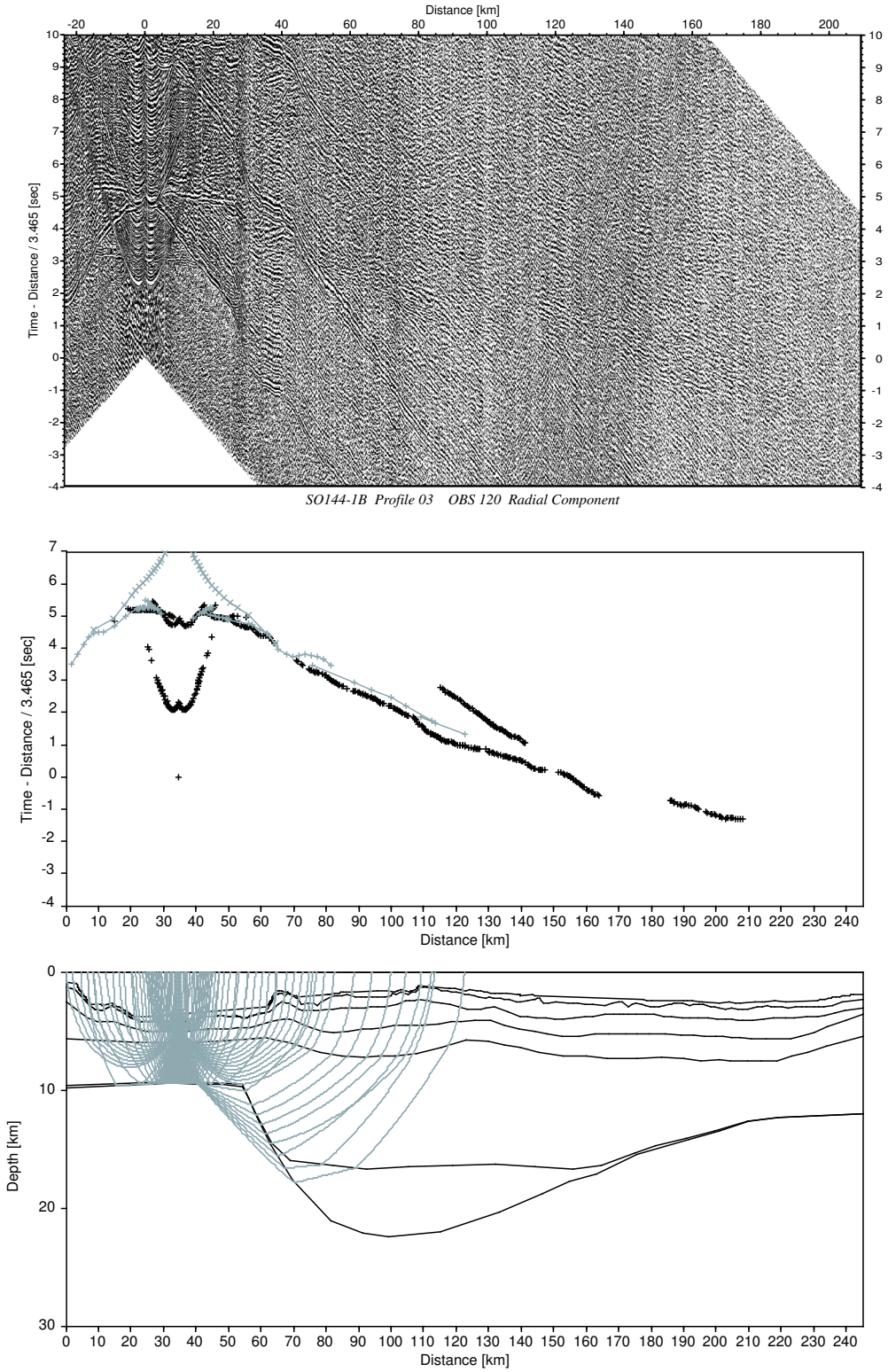


Figure 5.22: OBS 120, situated between Regina Ridge and Malpelo Ridge at the north-western end of the profile.

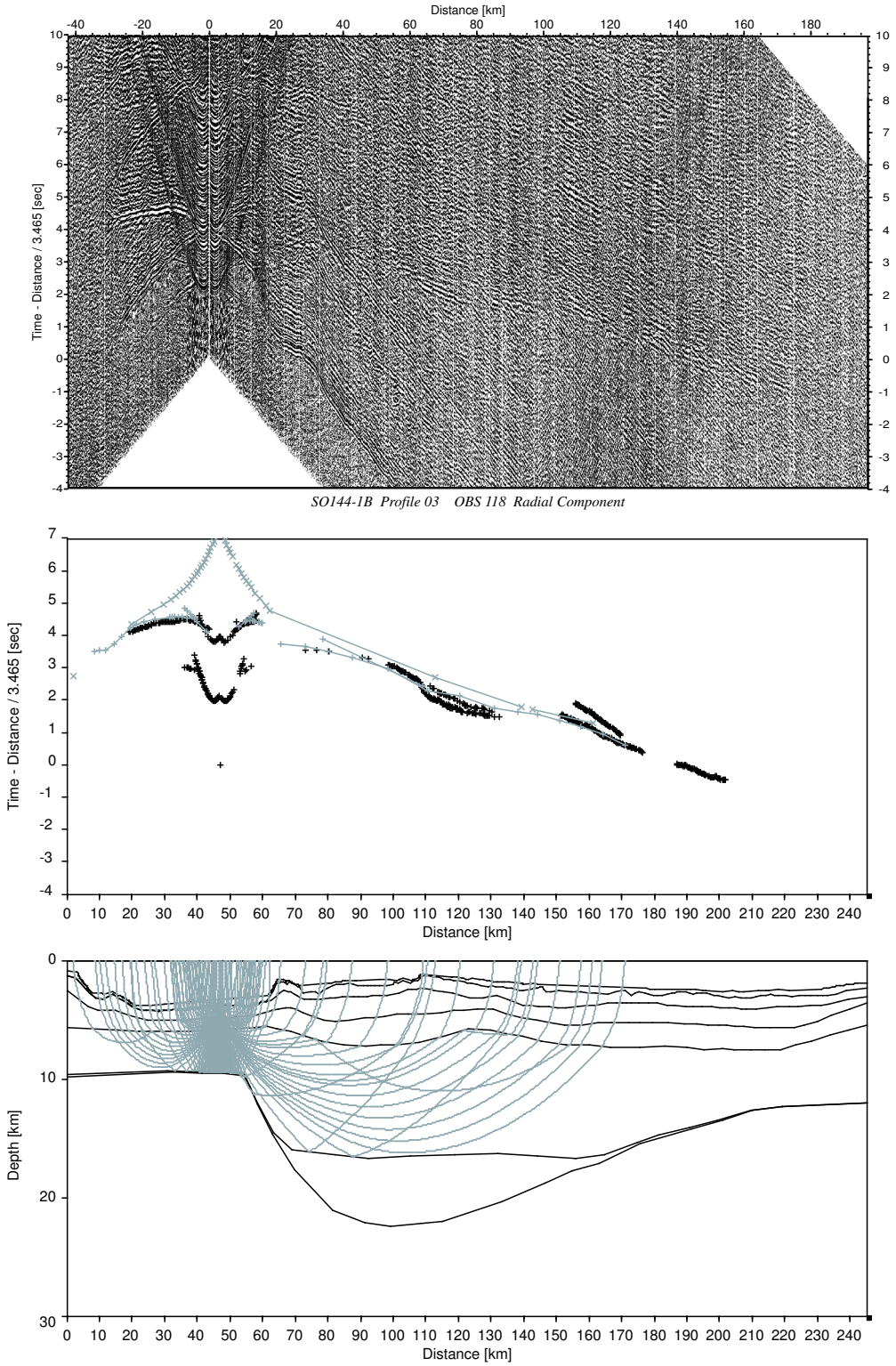


Figure 5.23: OBS 118, situated between Regina Ridge and Malpelo Ridge at the north-western end of the profile.

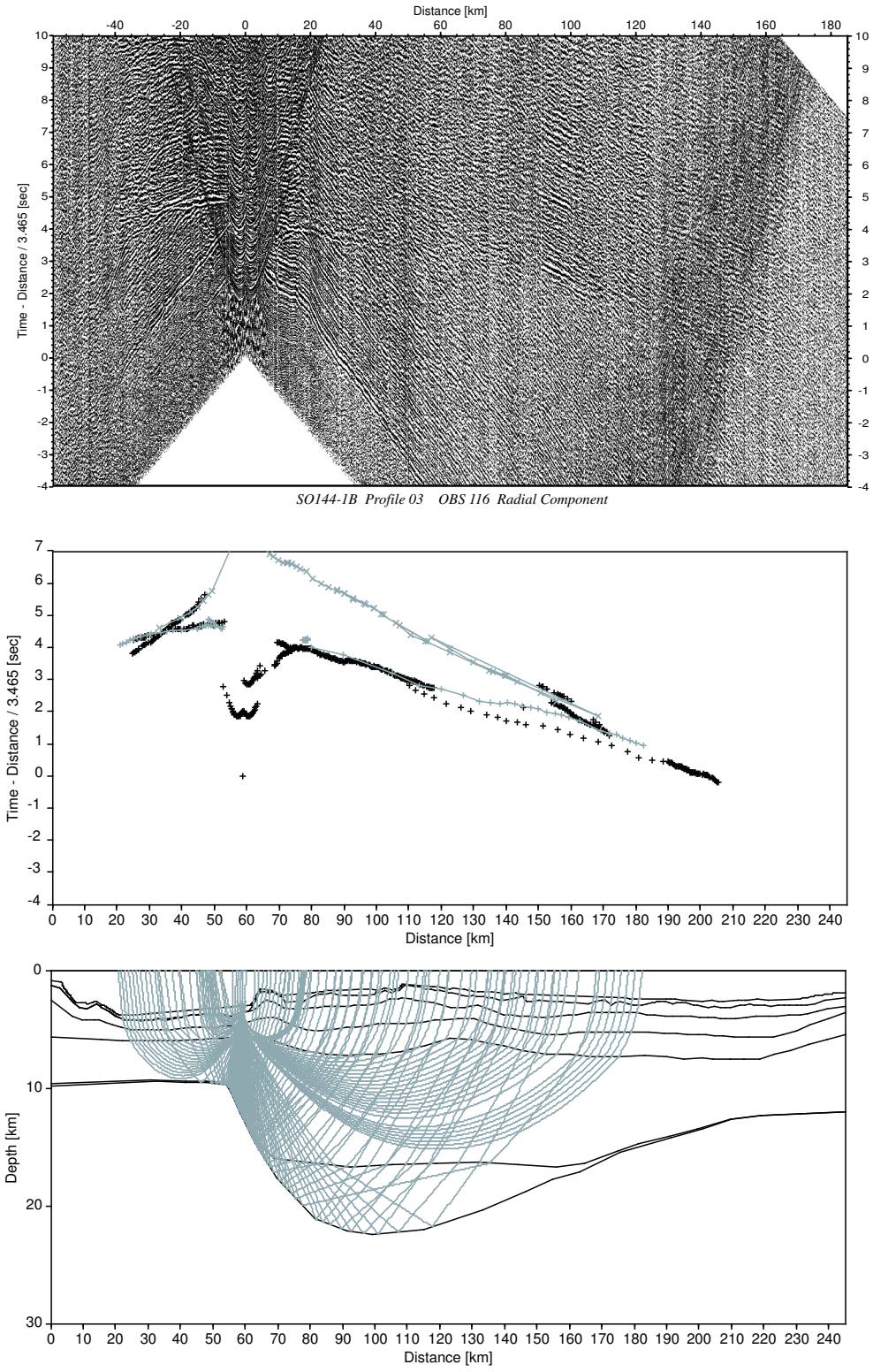


Figure 5.24: OBS 116, situated west of the northwestern ridge.

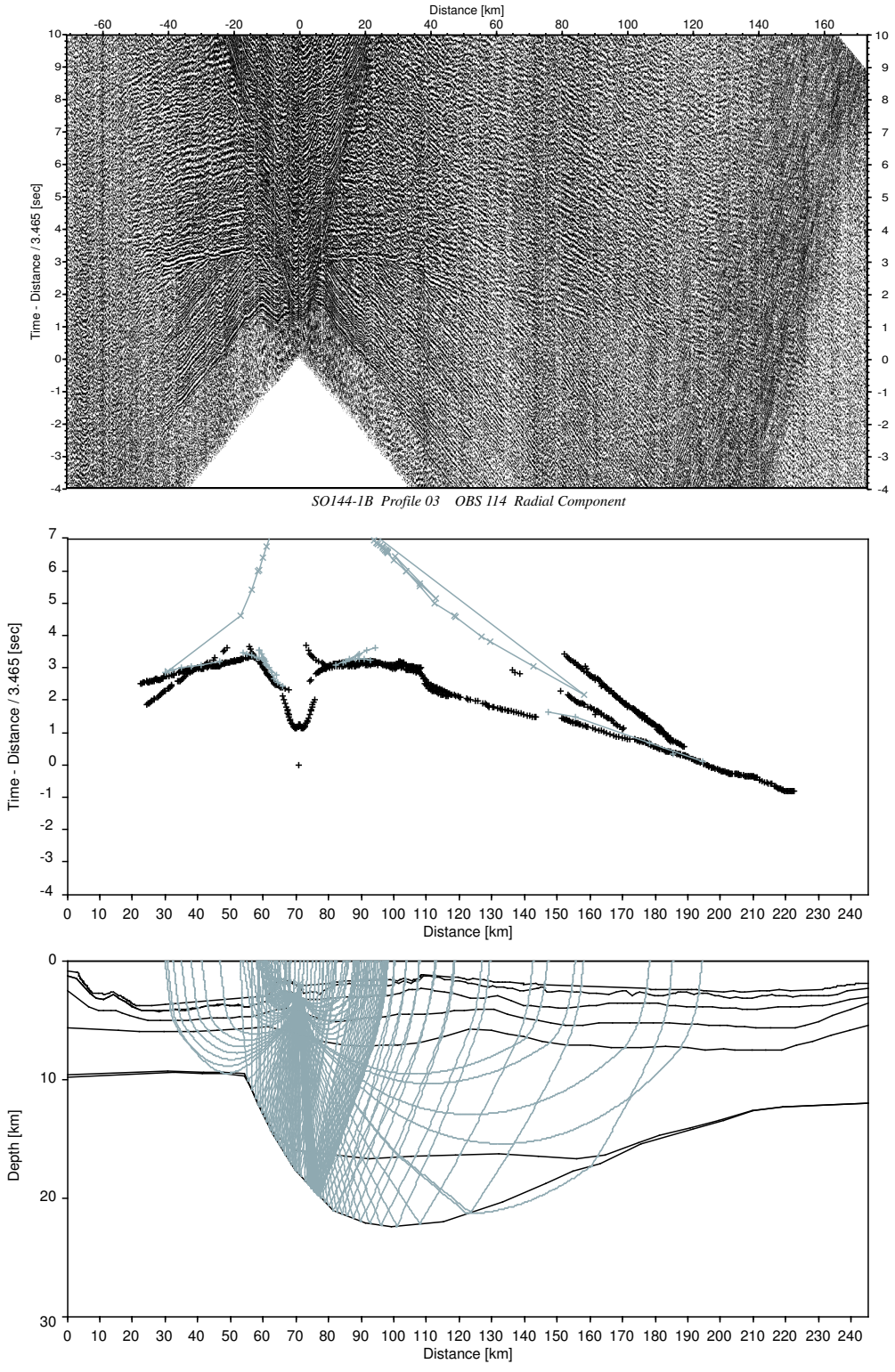


Figure 5.25: OBS 114, situated east of the northwestern ridge.

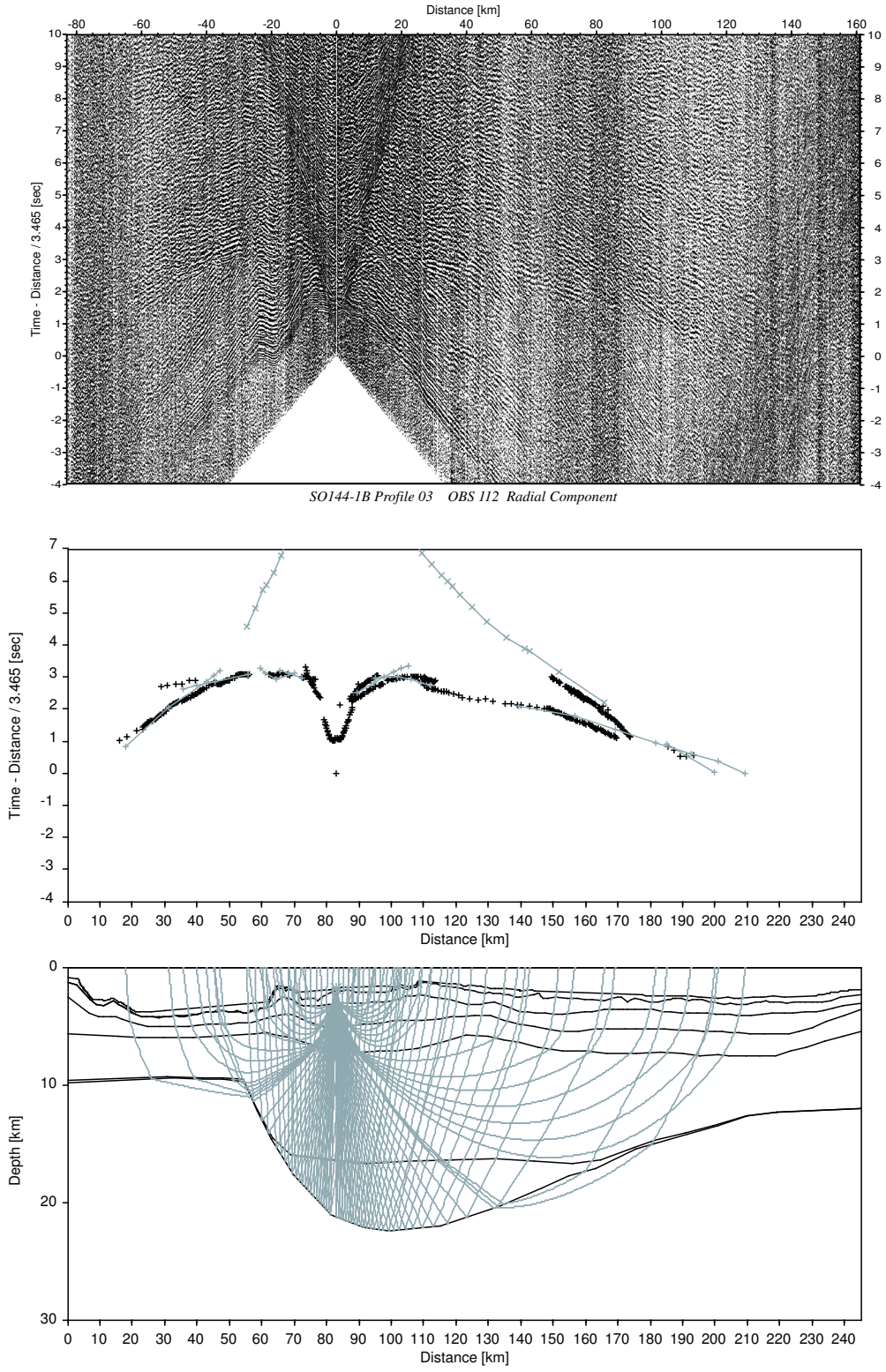


Figure 5.26: OBS 112, situated above the central graben.

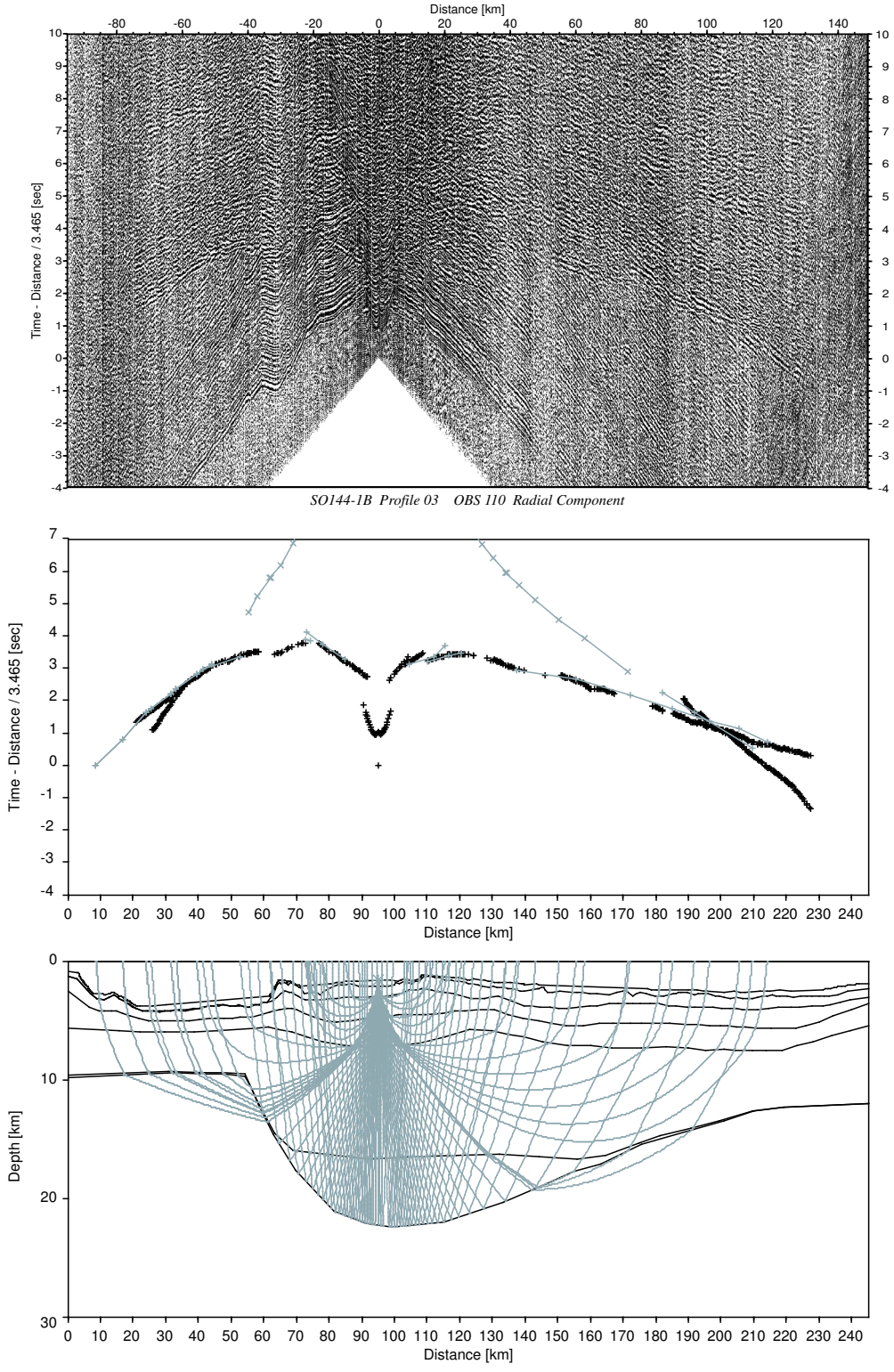


Figure 5.27: OBS 110, situated above the central graben in the midst of the profile.

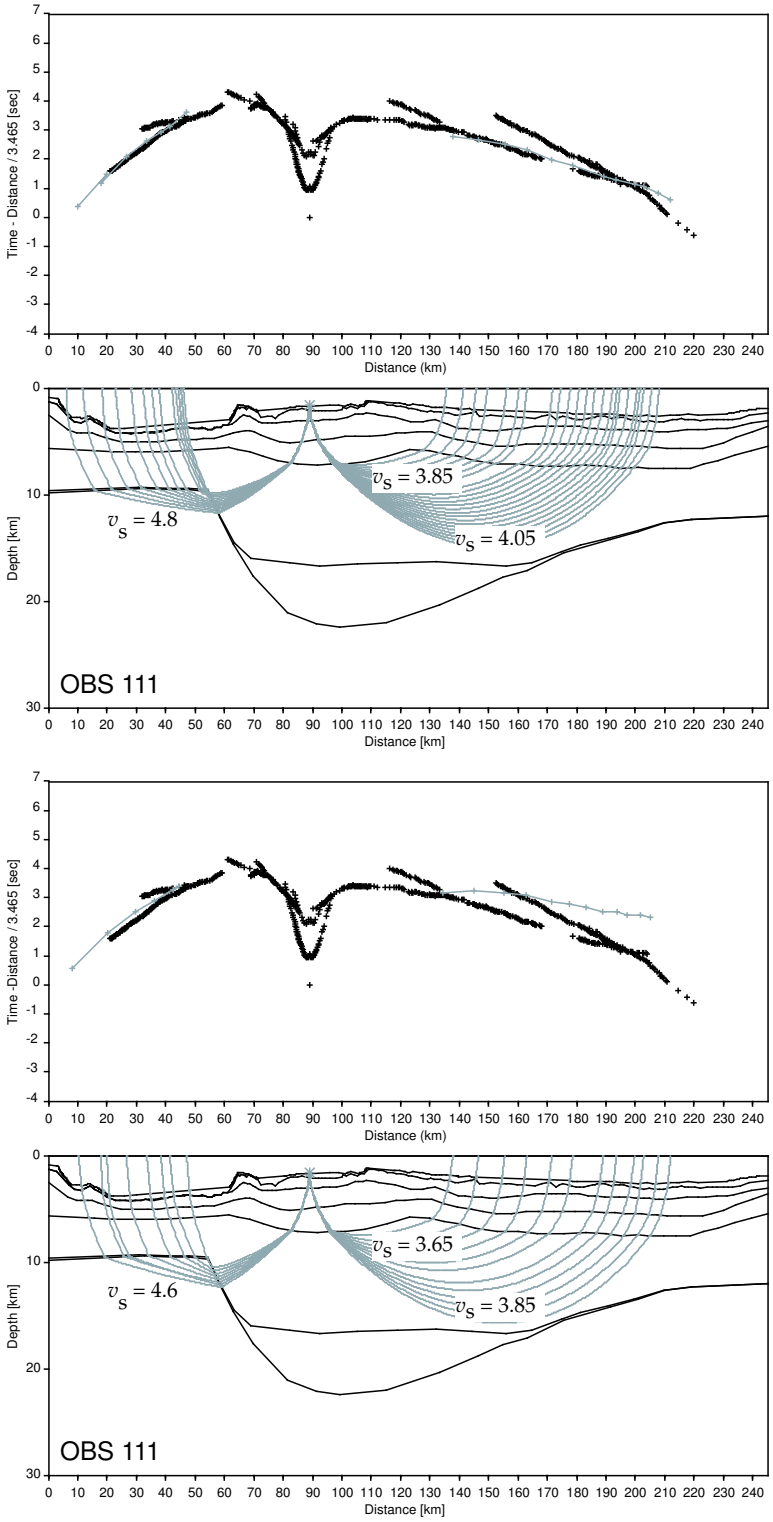


Figure 5.28: Error evaluation for OBS station 111, situated above the central graben in the midst of the profile. The upper two images display picked and calculated traveltimes with the correct velocity-depth model for the refraction through the lower crust and upper mantle. In the lower two images velocities had been changed by $5\%$ resulting in traveltime errors of 900ms for the refraction in the lower crust (to the right) and 250ms for the mantle refraction (to the left).

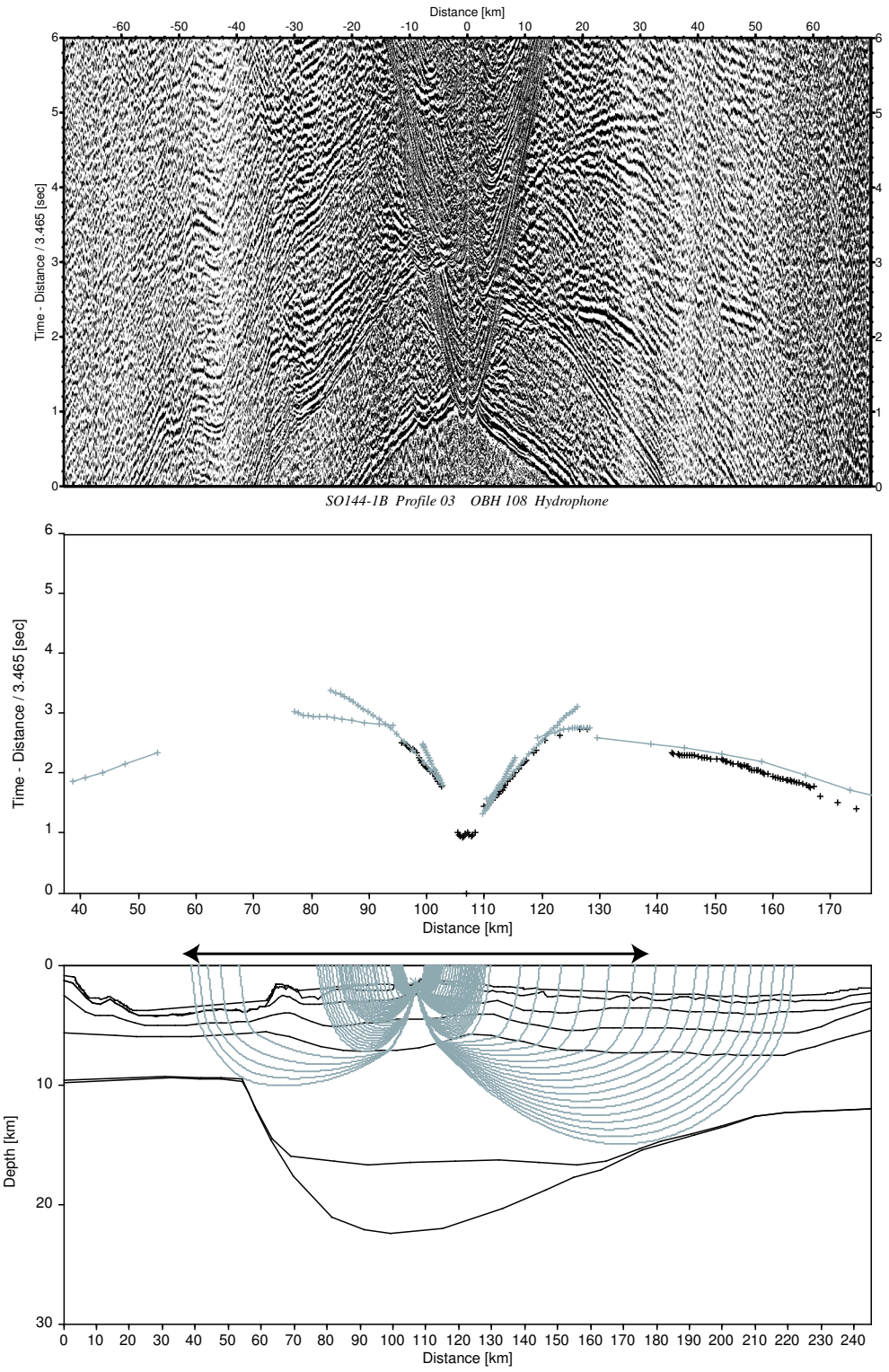


Figure 5.29: OBH station 108, situated northwest of the southeastern plateau. The upper image displays the data, a reduction velocity of 3.465km/s is used for display. The middle image illustrates the picked traveltimes in black overlain by the traveltimes inferred from forward modeling in grey (solid lines). The lower image shows the converted raypaths through the model subsurface. The offset range shown in the upper images is outlined as an arrow above the depth model.

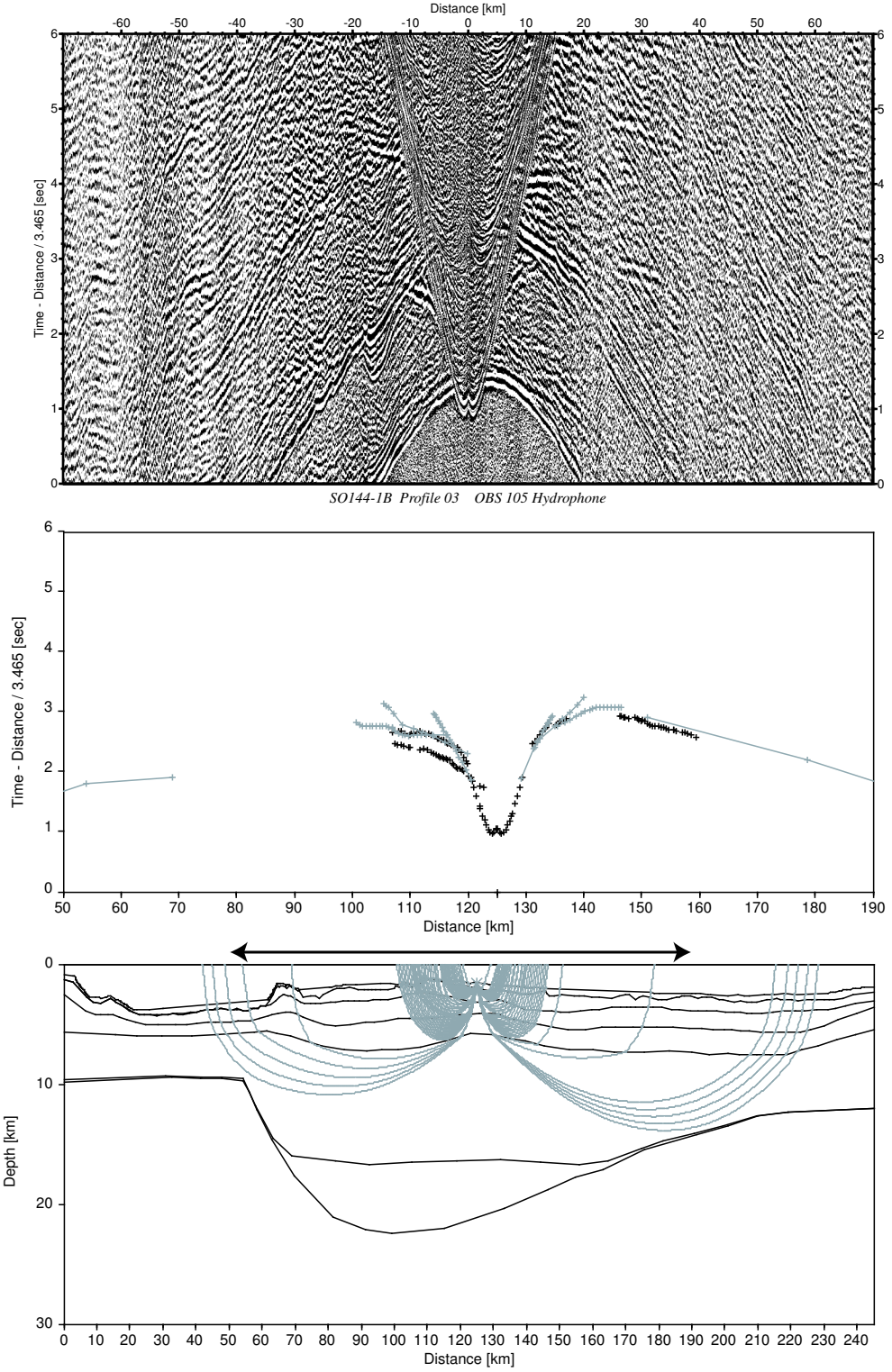


Figure 5.30: OBS station 105, situated on the southeastern plateau.

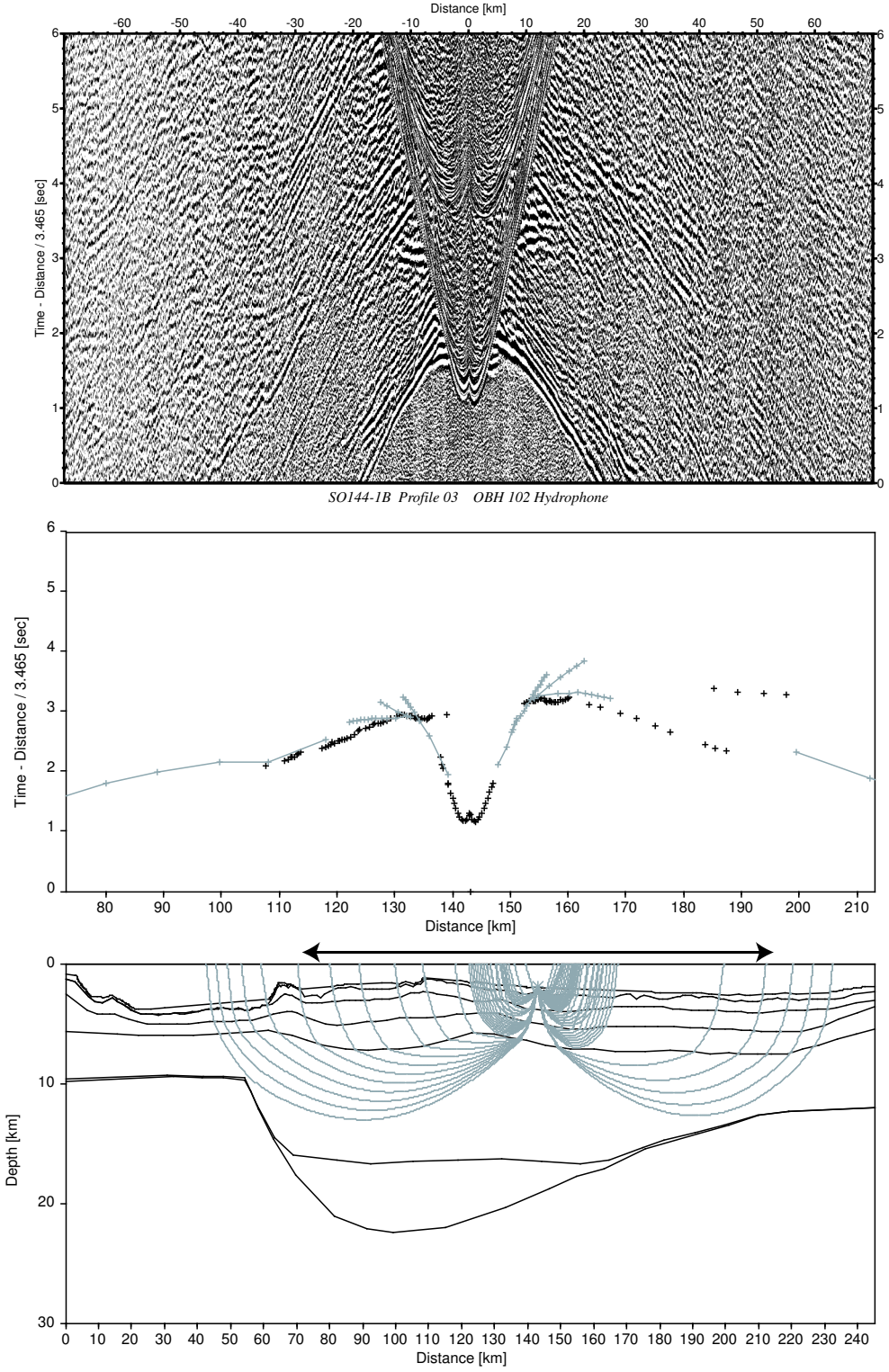


Figure 5.31: OBH station 102, situated on the southeastern plateau.

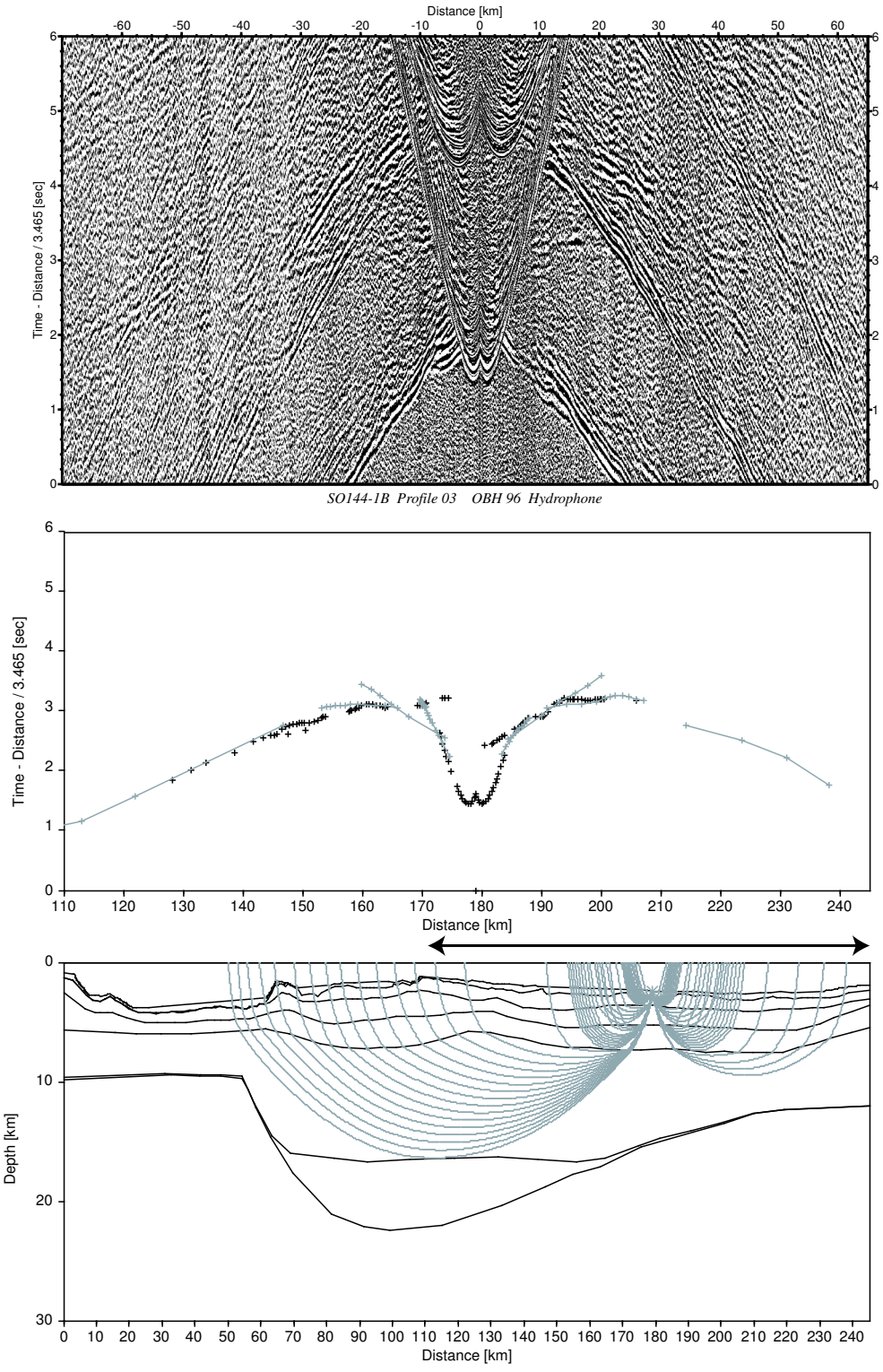


Figure 5.32: OBH station 96, located in the area where the southeastern plateau merges gradually with the surrounding seafloor.

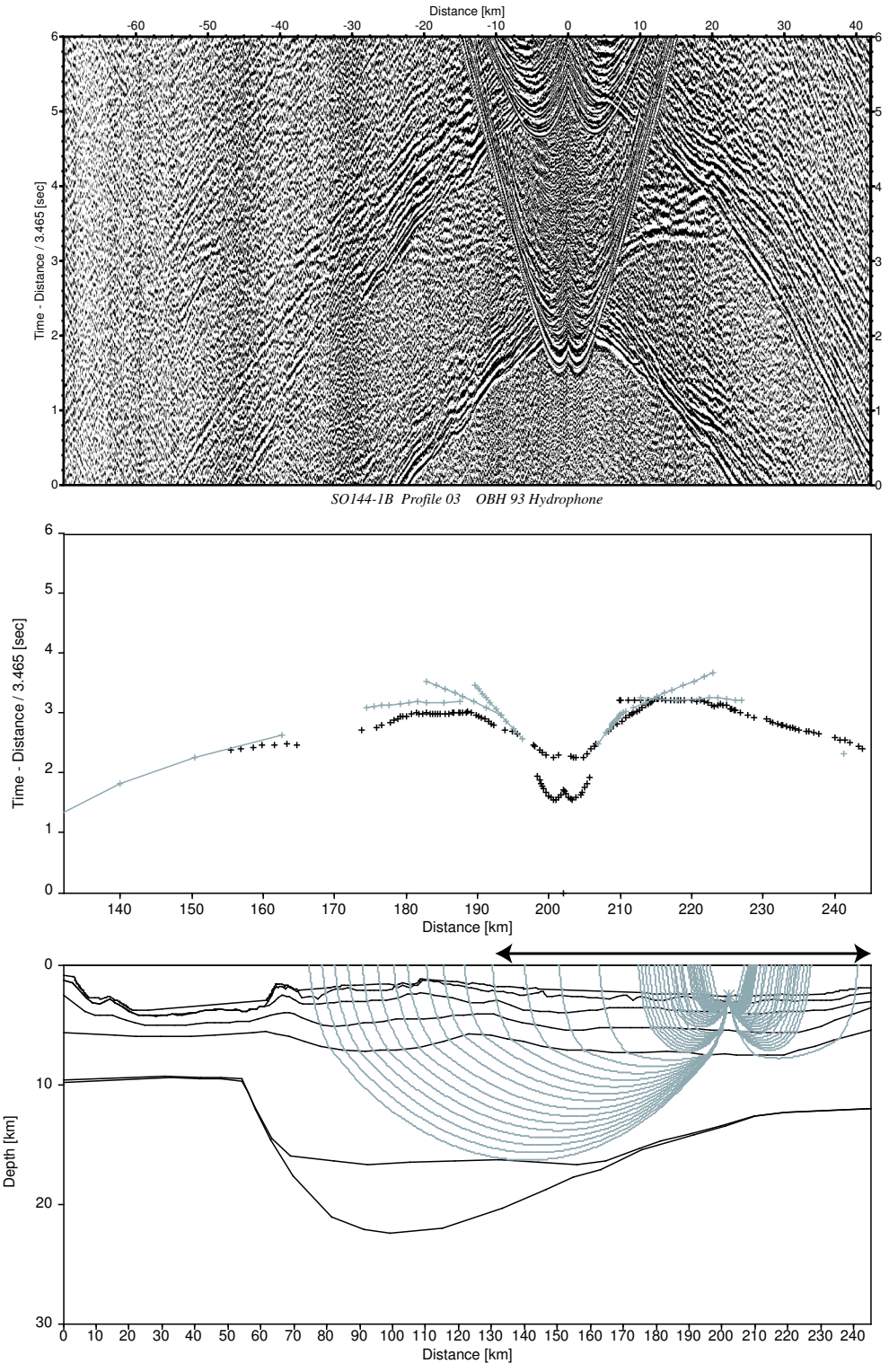


Figure 5.33: OBH station 93, located at the southeastern end of the profile across Malpelo Ridge.

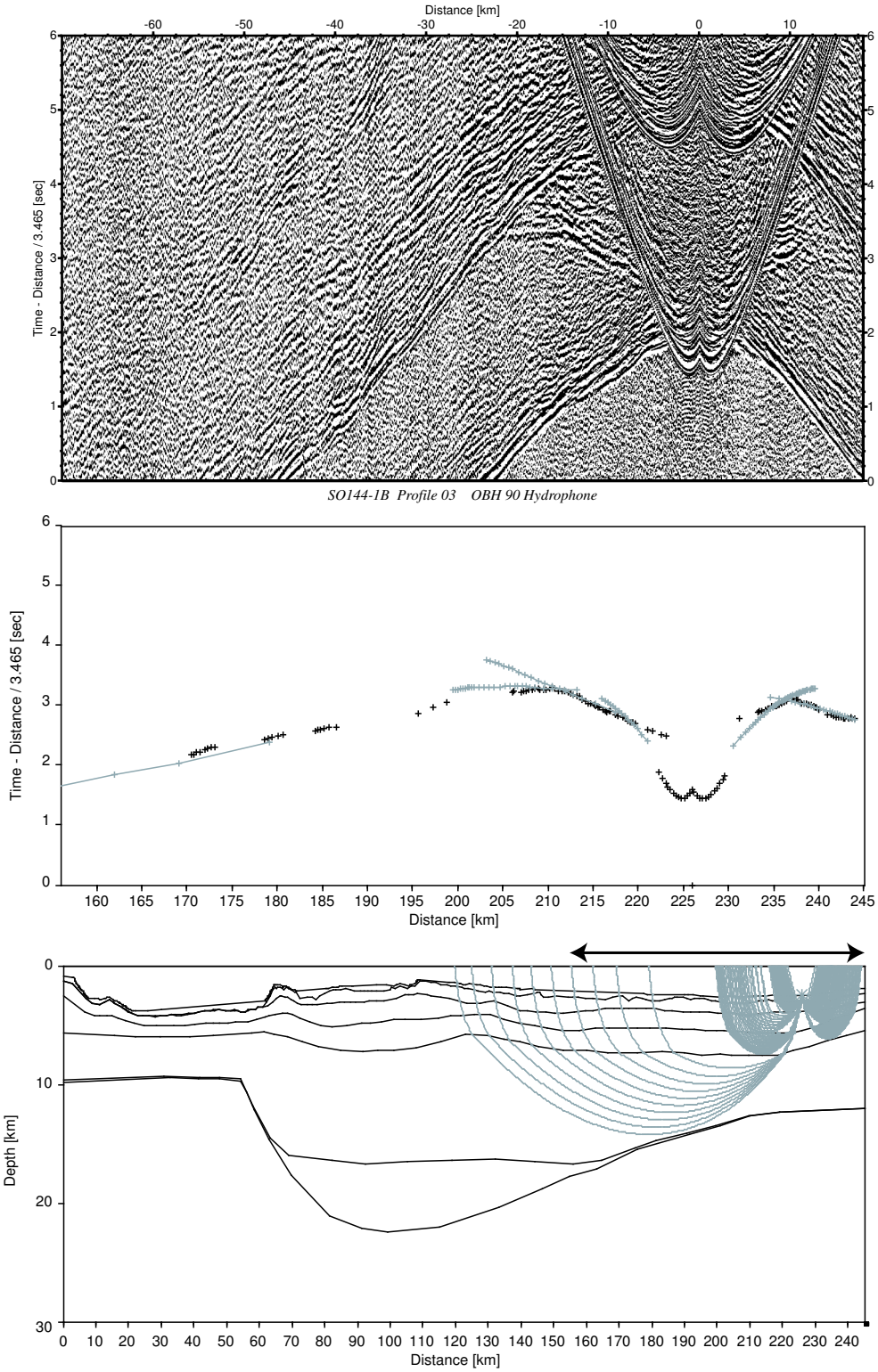


Figure 5.34: OBH station 90, located at the southeastern end of the profile across Malpelo Ridge.

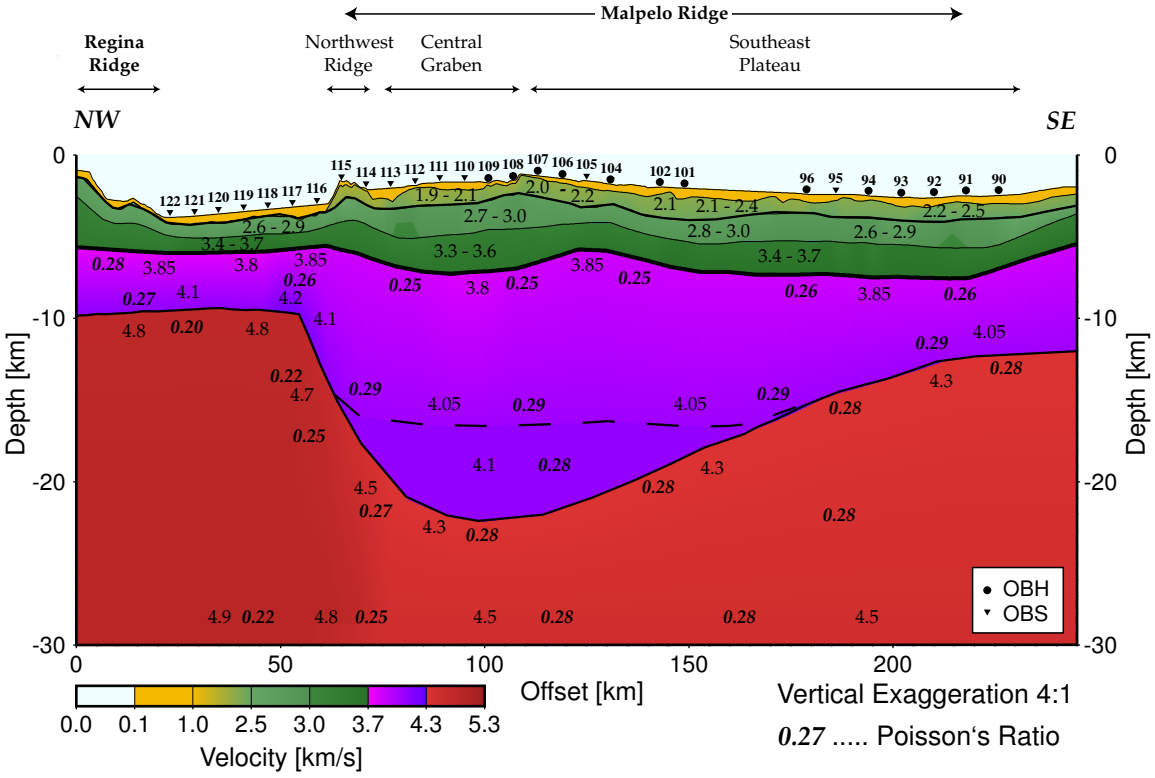


Figure 5.35: 2-D S-wave velocity versus depth model across Malpelo Ridge, Eastern Panama Basin. Values written in *italic* denote calculated Poisson's ratio $\sigma$.

ter 5.3.1). Velocities are slightly higher (4.2km/s) northwest off the ridge.

Mantle velocities show a significant variation throughout the model. In the eastern part of the profile, below the central graben and southeast plateau, values ranging from 4.3km/s to 4.5km/s were found. Northwest off the ridge velocities are much higher with values of 4.8km/s to 4.9km/s.

## 5.5 Anisotropy

In recent years mainly two layers of the oceanic crust have been identified to exhibit anisotropy in an amount detectable by seismic surveys: the uppermost crust and the upper mantle. Anisotropy in the uppermost crust is most probably caused by the preferred orientation of large-scale fissures and fractures, anisotropy in the upper mantle is correlated with the alignment of olivine crystals.

When studying arrival time data it is important to distinguish between anisotropy and lateral heterogeneity. Typically seismic data sets for the ocean crust have too much scatter in arrival time to unambiguously demonstrate anisotropy [Bratt and Solomon, 1984, Stephen, 1985] and the observation of shear wave splitting could be rather attributed to a scattering phenomenon. Stephen [1985] performed a detailed analysis of particle motions of converted shear wave arrivals from explosive sources at various azimuths at DSDP Site 504B and showed that anisotropic structure was required in the upper crust to explain the patterns of particle motion observed. The same experiment was used to study lateral heterogeneity across an area with a diameter of 18km [Stephen, 1988]. Particle motions seemed to be relatively undisturbed by the topography under the source or lateral variations of the ray path and to be controlled primarily by the anisotropic structure at the entry point of the crust. The shear wave particle motions get locked near the conversion point and are not affected by the rest of the path [Stephen, 1988]. Stephen [1985] suggested anisotropy to be restricted to the upper 500m of basement in the area and to be caused by the preferred orientation of fractures and fissures. These fractures were created in the early stages of crustal development by near axis extensional processes and normal block faulting. Their orientation is sensitive to the local stress field, they tend to align perpendicular to the minimum compressive stress. On a scale of kilometers, alignment is generally parallel to mid-ocean ridges, and bathymetric surveys of the seafloor reveal elongated seafloor fabrics that are mainly related to sets of ridge-parallel faults [Dunn and Toomey, 2001]. Shear waves propagating through such a medium will be split into two phases: one polarized along the cracks and one polarized perpendicular to it and propagating with a lower velocity.

The existence of compressional wave velocity anisotropy in the upper oceanic mantle is also well established [Clowes and Au, 1982, Nicolas and Christensen, 1987]. It can be studied through analysis of the refracted Pn-phase or through comparison of P-wave velocities on perpendicular profiles. The direction of maximum P-wave velocity is approximately parallel to the direction of seafloor spreading, due to the preferential alignment of olivine crystals. The strongest anisotropies are thus expected in dunite and harzburgite, which are assumed to predominate in the oceanic upper mantle. Au and Clowes [1980] and Clowes and Au [1982] evaluated P-wave velocities of 7.5km/s and 8.3km/s for two seismic wide-angle profiles perpendicular and parallel to spreading direction, respectively. The calculated P-wave velocity anisotropy is $10\%$. For the same profiles, a very low degree of S-wave velocity anisotropy was found for the upper mantle, indicating that

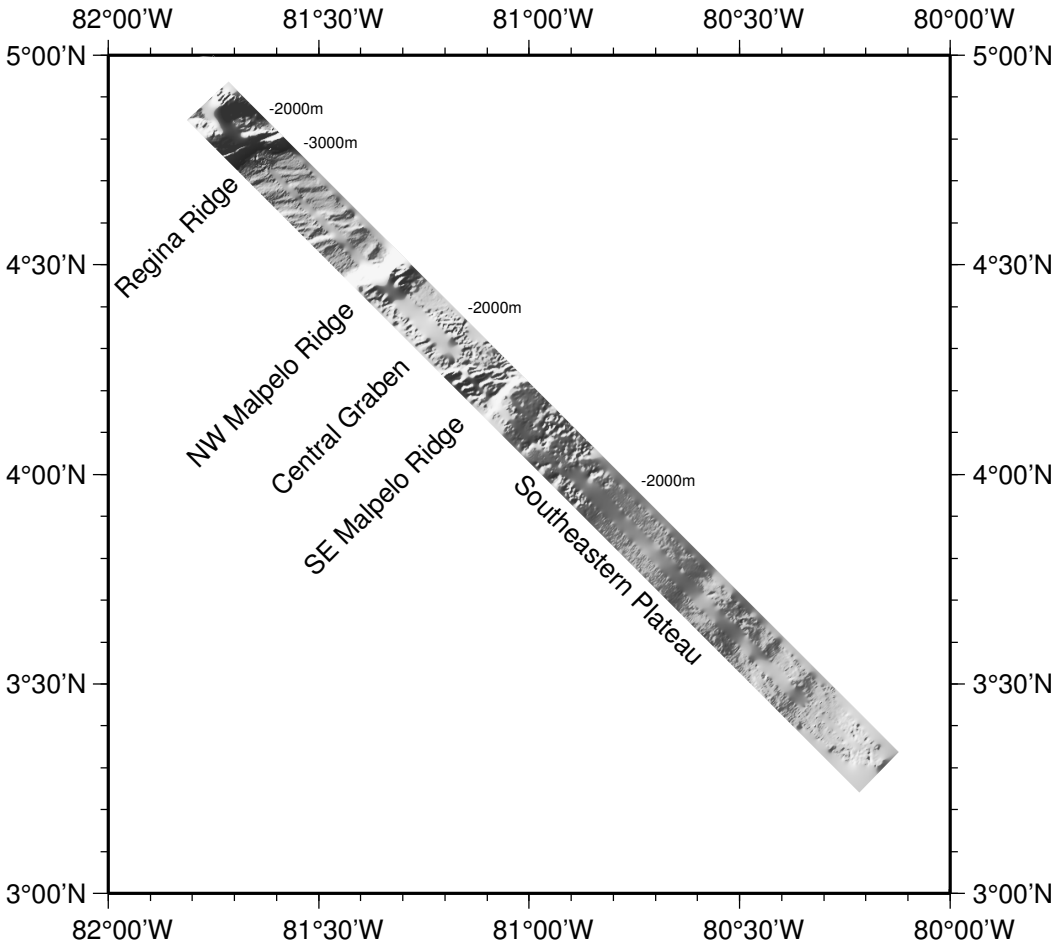


Figure 5.36: Seafloor bathymetry as derived from two adjacent Hydrosweep tracks along Profile P03 across Malpelo Ridge. Small numbers denote depth below sea level.

the upper mantle is nearly isotropic for propagating S-waves. The low degree of S-wave anisotropy is consistent with laboratory measurements [Christensen and Salisbury, 1979]. An important implication is that the upper mantle will be anisotropic in terms of Poisson's ratio, with $\sigma$ being higher in direction parallel to spreading. Clowes and Au [1982] calculated a $\sigma$=0.22 for the profile perpendicular and $\sigma$=0.28 for the profile parallel to the spreading direction.

As has been described in chapter 5.4 elliptical particle motion is observed for the converted shear wave arrivals on the horizontal components of the Malpelo Ridge data, which implies shear wave splitting due to anisotropy along the travelpath [Crampin, 1985]. Figure 5.36 illustrates the seafloor bathymetry along the profile as derived from Hydrosweep measurements. In the area between Regina Ridge and the northwestern tip of Malpelo Ridge, lineations associated with ridges and troughs and striking in EW direction can be observed. These are interpreted as faults perpendicular to spreading direction. For any observed shear wave splitting velocities which are either maximum in direction of spreading, for an anisotropy in the upper mantle, or minimum in direction of spreading, for an

anisotropy in the upper crust, should be observed. This assumption may not be valid for OBS stations 110 to 115 which are located on Malpelo Ridge. Malpelo Ridge may have been formed under a different stress regime than the oceanic crust between Malpelo and Regina Ridges.

Unfortunately the profile intersects the faults at an angle of $45° - 50°$, since it was designed to be perpendicular to Malpelo Ridge. The horizontal components have been rotated into radial and transversal components, which is in direction of the profile and perpendicular to it, respectively. For the case of a shear wave propagating through an anisotropic layer which is oriented at an angle of $45°$ to the profile, the split $S_V$ and $S_H$ phases would arrive nearly at the same time. Consequently the particle motion would be strictly linear [Crampin, 1985]. On particle motion plots for OBS station 117 (Figure 5.14) elliptical motion for the converted phases can be observed, though.

Figure 5.37 displays the picked traveltimes for the radial and transversal components of OBS station 111. The traveltimes are overlain and the observed time delay between the two components ranges from 8-10ms. An unexpected detail is the fact that the radial component is faster than the transversal component in the southeastern direction but slower in the northwestern direction. Similar time delays are observed on OBS stations 111 to 114 and 121, with the radial component showing faster velocities either in direction of positive (OBS 111, 113, 121) or negative (OBS 112) offsets. OBS stations 114, 115, and 121 show a transversal component that is 8-10ms faster than the radial component for positive and negative offsets. On all the other OBS stations, there is only a time delay of 0-2ms observable. This high variation of either the radial or transversal component being faster in different directions or both components appearing simultaneously indicates that not anisotropy but lateral heterogeneity is responsible for the observed time delays.

This lateral heterogeneity occurs most probably in the upper crustal layers near the OBS station, a non-horizontal interface between sediment and basement is one possibility. The occurrence of strong converted arrivals on the vertical component is also attributed to lateral heterogeneity in the upper crust or tilted sediment/basement interfaces (chapter 5.4.1), which supports this interpretation. The time delays observed on the various stations remain constant along the whole offset, in either positive or negative profile direction. This indicates that the lower crustal layers are more homogenous, otherwise a variation in the time delay would be observed for higher distances from the OBS.

The elliptical particle motion that is observed for the converted shear wave arrivals on the horizontal components (see chapter 5.4) can also be attributed to lateral heterogeneity. If shear wave anisotropy is existent in the upper crustal or upper mantle, it would have to be smaller than detectable from the data, since no corresponding time delays could be identified, especially not for the upper mantle.

The observed time delays of 8-10ms are associated with a change in velocity of 0.1km/s in the upper crust, which is within the error estimate for the S-wave model. An anisotropy of $2 - 3\%$ would be associated with a difference in velocity of 0.05km/s, and could not be resolved from the data without more extensive evaluation of particle motion

plots. Similarly no upper mantle anisotropy exceeding $3 - 4\%$ was detected.

Nevertheless the possibility remains that the layout of the profile in a direction perpendicular to Malpelo Ridge and at an angle of $45° - 50°$ to the spreading direction between Malpelo and Regina Ridges has unfortunately diminished the ability to interpret the data in terms of anisotropy. Also the oceanic crust between Regina and Malpelo Ridges and the thickened crust underneath Malpelo Ridge could exhibit anisotropy with different amounts or orientations. Additionally anisotropy in the uppermost crust and in the upper mantle could have a contrary effect, at least to some extent. A more detailed study of anisotropy including a rotation of the data into the direction of seafloor spreading and a more extensive evaluation of particle motion diagrams could possibly clarify these questions, but was not attempted within this study.

For the profile across Malpelo Ridge no S-wave anisotropy in the upper mantle higher than $2 - 3\%$ was detected, and no evaluation of P-wave anisotropy was performed. The lack of a higher amount of anisotropy justifies the means of two-dimensional raytracing, which assumes isotropy, and enables the interpretation of changes in Poisson's ratio as the consequence of mineralogical changes [Holbrook et al., 1988].

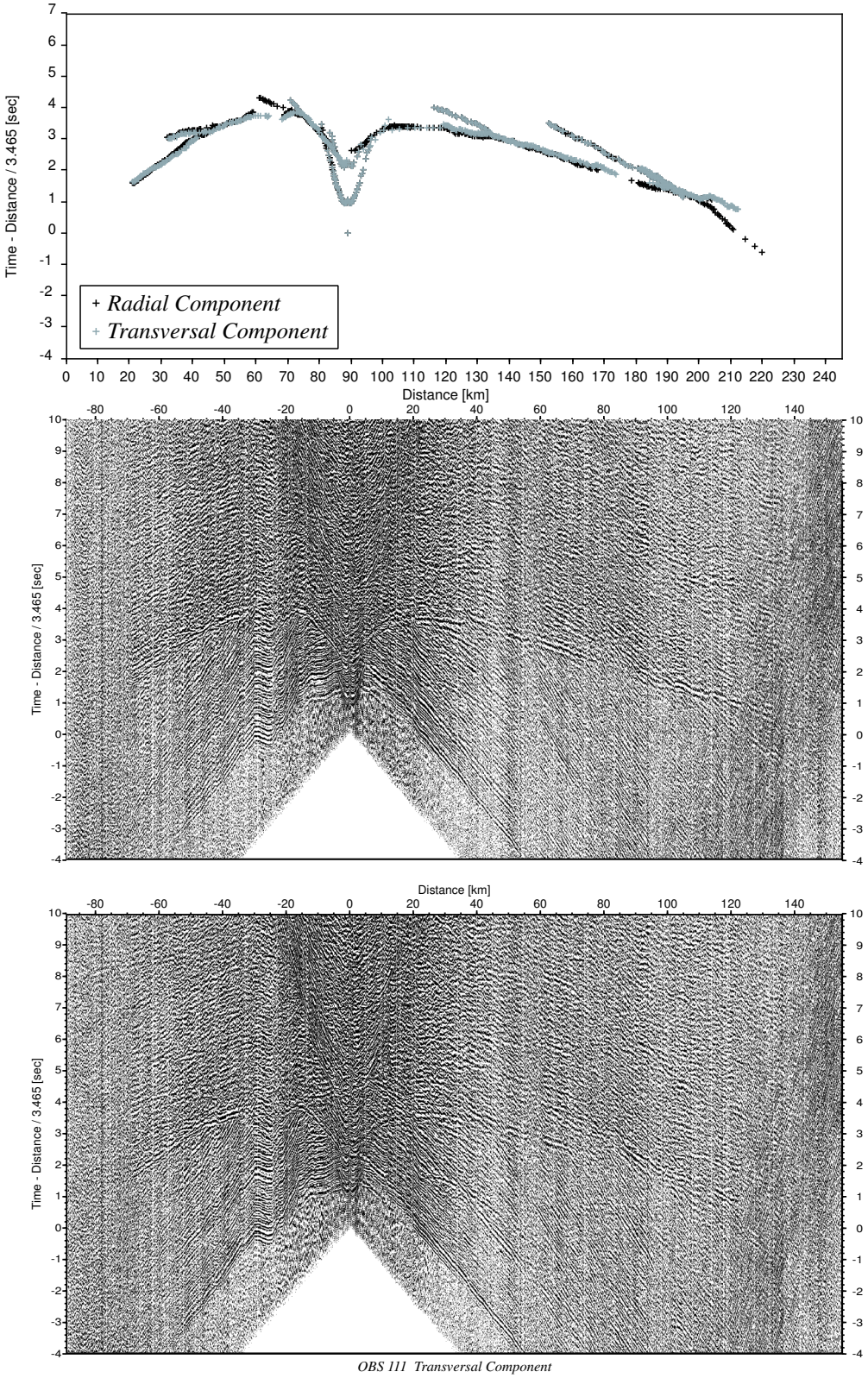


Figure 5.37: Record sections and traveltimes picks of the PSS-phase for the radial and transversal component of OBS station 111. Data are displayed with a reduction velocity of 3.465km/s.

# Poisson‘s Ratio across Malpelo Ridge

# 6

In this section a petrological interpretation of the derived model of Poisson's ratio $\sigma$ along the profile across Malpelo Ridge will be given. Values for $\sigma$ will be compared to published data aiming at determination of the average type of rock or mineral assemblage present at various depths across Malpelo Ridge. In order to correlate an elastic parameter as Poisson's ratio obtained through forward modeling of seismic refraction data with laboratory measurements and in order to develop a reasonable interpretation, a view general assumptions should be considered first.

Since the seismic waves used in this study have wavelengths of 400m to 1400m a P-wave velocity of 6.0km/s in the crust is merely defined as the P-wave velocity averaged over several wavelengths. If this velocity (and the corresponding shear wave velocity and Poisson's ratio) can be correlated to a velocity measured for a rock sample under a certain pressure equivalent to a certain depth, this may only indicate that the average crustal composition in a depth interval of several wavelengths may resemble that of the rock sample. To enhance the probability of the interpretation and in the attempt of constraining the geological possibilities the resulting model is compared to rock samples from an ophiolite sequence [Salisbury and Christensen, 1978], to published data from similar surveys performed on oceanic crust [Spudich and Orcutt, 1980, Au and Clowes, 1984], and to available data from Deep Sea Drilling Projects [Swift et al., 1998a, Collins et al., 1989, Iturrino et al., 1991, Dick et al., 1992, Dick et al., 1999].

Salisbury and Christensen [1978] presented a detailed investigation of the Blow-Me-Down Massif, Bay of Islands Complex, where they measured compressional and shear wave velocities across an ophiolite sequence. Measurements of velocities were performed under elevated hydrostatic pressures equivalent to a depth at which certain rock complexes would be expected for oceanic crust. This enabled the reconstruction of a possible velocity column through the ophiolite complex that should be comparable to observed velocity structures of the oceanic crust. It also allows to compare their measured values for $v_p$, $v_s$, and $\sigma$ directly with the values obtained at the northwestern end of the Malpelo profile where crustal thickness is about 6-7km. Underneath Malpelo Ridge crustal thickness has a maximum of 20km, and assuming a density of $\rho$=2.9km/m$^3$ laboratory measurements undertaken at pressures about 1-2kbar higher would be needed to compare Poisson's ratio for the lower crust and upper mantle in this area more exactly. Since the change in $\sigma$ with an increasing pressure of 2kbar is only about 4-5% (chapter 4) the resulting error is assumed to be negligible. Similar assumptions were made for changes in temperature.

Deep Sea Drilling Project (DSDP) Holes 504B and 735B are two of the deepest pene-

trating boreholes into ocean crust, both of them reach into sections with the properties of seismic layer 3. Hole 504B lies on 6.6ma Nazca Plate crust south of the Costa Rica Rift and has a total depth of 2111mbsf (meters below sea floor) or 1836m into basement. The crustal stratigraphy consists of 274.5m mostly pelagic nannofossil ooze overlying 571.5m of basaltic pillows and flows and a 209m thick transition zone of pillows, flows, and dikes overlying a diabase unit extending to the base of the borehole [Swift et al., 1998b]. Hole 735B is located at the very-slow spreading Southwest Indian Ridge and reaches a depth of 1508m below seafloor. The drilled sequences consist mainly of metagabbro, olivine gabbro, and oxide-rich gabbro and differs in many respects from known ophiolite sequences and samples taken at fast spreading ridges [Dick et al., 2000]. Related publications comprise compressional and shear wave velocities measured from borehole samples and borehole logging, and results from accompanying VSP surveys and wide-angle reflection and refraction surveys.

During the last few decades various publications and especially those related to DSDP site 504B have stressed that the velocity structure of the crust is more closely related to changes in porosity and metamorphic grade than to its igneous structure. E.g. the transition from layer 2A to 2B occurs within the extrusive pile and the top of layer 2C is associated not only with the top of the sheeted dike complex but also with the first appearance of greenschist facies alteration products and with an abrupt reduction in porosity. The boundary between layers 2 and 3 had been placed within the sheeted dike complex in various ophiolite complexes and the upper part of layer 3 was suggested to consist predominantly of dolerites and metadolerites rather than gabbro [Carlson and Herrick, 1990, Detrick et al., 1994], a proposal which was confirmed at DSDP site 504B.

In Figure 6.1 the observed P-wave and S-wave velocity paths for three OBS stations are plotted in the $v_p - v_s$ plane. Plotting P-wave and S-wave velocities on the $v_p - v_s$ plane is a very convenient approach for purposes of comparison with velocities derived from laboratory samples or other deep seismic sounding profiles. Paths of constant Poisson's ratio form straight lines in the $v_p - v_s$ plane and are plotted for values of $\sigma$=0.20 to $\sigma$=0.34 in Figure 6.1.

OBS station 120 is representative for the area northwest off Malpelo Ridge, OBS station 110 illustrates the velocity-depth distribution below the central graben, OBH 92 is located at the southeastern end of the profile. For comparison laboratory measurements [Salisbury and Christensen, 1978] as well as data obtained from refraction measurements on oceanic crust [Au and Clowes, 1984, Spudich and Orcutt, 1980] are included in the figure. The velocities modeled for Malpelo Ridge compare well to the published values, e.g. $v_p-$ and $v_s-$velocities at the top and bottom of layer 3 bound an area of pyroxene and olivine gabbros, which are expected to build part of seismic layer 3. The different layers building the crust at Malpelo Ridge are discussed in more detail in the following sections.

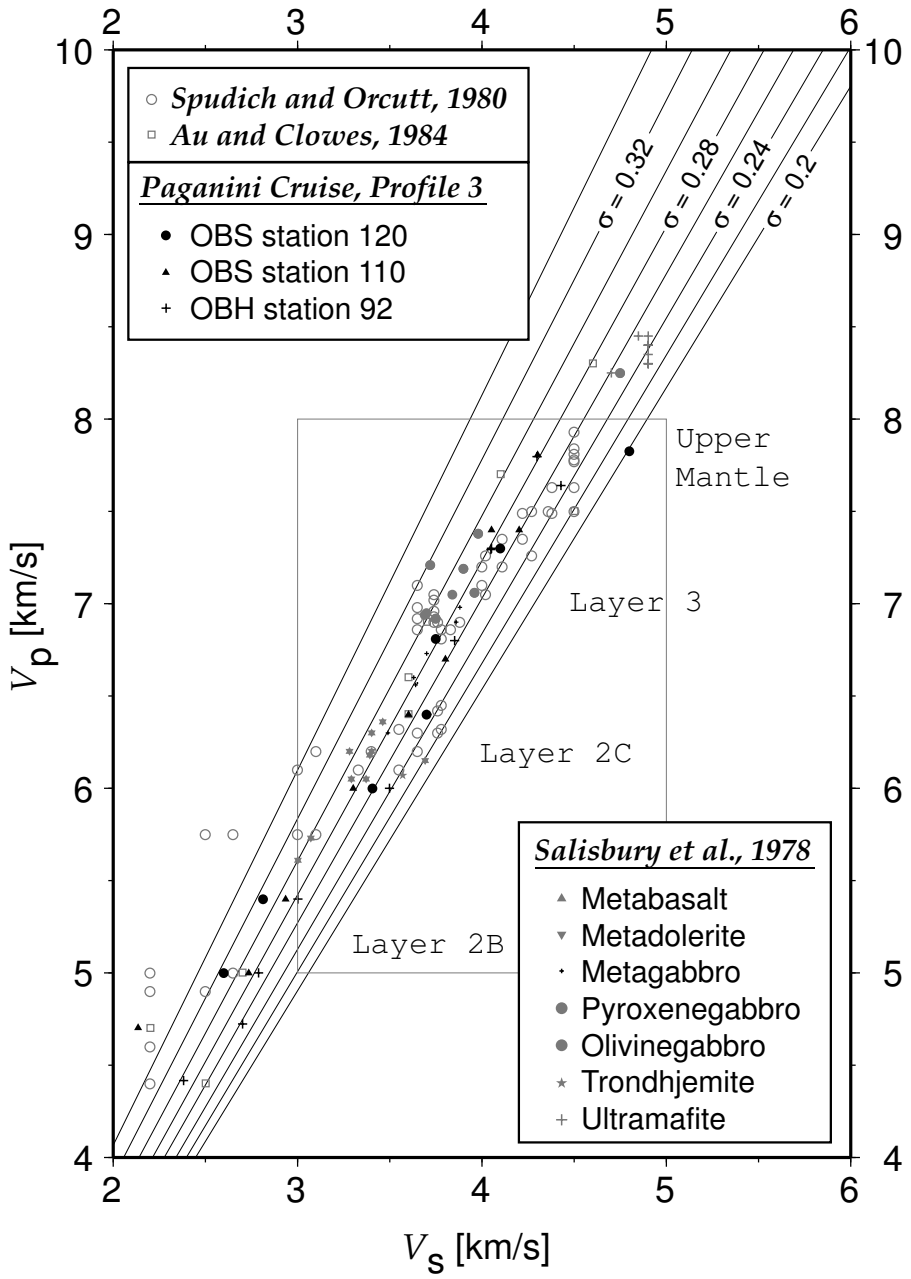


Figure 6.1: The $v_p - v_s$ paths of three representative OBS stations along Paganini Profile P03 across Malpelo Ridge. The inlay represents the area illustrated in Figures 6.2 and 6.3. For comparison the following are shown: Laboratory measurements from samples taken from the Bay of Islands Ophiolite Complex, after Salisbury and Christensen [1978]; values derived from seismic refraction measurements, after Spudich and Orcutt [1980], Au and Clowes [1984].

### 6.0.1 Sedimentary layer

Possible parameters that influence Poisson's ratio of sedimentary layers are not only percentage of porosity, pore structure, and possible filling with fluids and/or cement, but

| | $v_p$[m/s] | $v_s$[m/s] | Poisson'sRatio | Reference |
|---|---|---|---|---|
| **coarse sand** | 1836 | 250 | 0.491 | Hamilton [1971] |
| **silty sand** | 1677 | 457 | 0.457 | Hamilton [1971] |
| **sandy silt** | 1552 | 379 | 0.461 | Hamilton [1971] |
| **clayey silt** | 1535 | 312 | 0.477 | Hamilton [1971] |
| **clay** | 1505 | 196 | 0.491 | Hamilton [1971] |
| **calcareous ooze** | 1680-1920 | 800-850 | 0.35-0.39 | Wilkens et al. [1992] |

Table 6.1: Compressional and shear wave velocities and Poisson's ratios for marine sediments. Data are taken from Hamilton [1971] and Wilkens et al. [1992].

also lithology and degree of consolidation. Values of Poisson's ratio of the sedimentary layer are consistently high throughout the model, ranging from 0.44 to 0.49, indicating a low degree of consolidation. This interpretation is consistent with samples taken from various dive sites across Malpelo Ridge, which were recognized as pelagic calcareous ooze [Lonsdale and Fornari, 1980]. At DSDP sites 501 and 504 drilled sediments also were described as "primarily nannofossil oozes with changes in induration at $\sim$150m below seafloor to siliceous chalk and at $\sim$225mbsf to limestones interbedded with chert" [Swift et al., 1998a]. The reduced carbonate dissolution is probably attributed to the high sediment accumulation rates in the Panama Basin of 40-60mm/a as a result of high equatorial surface water productivity. At site 504B sediment thickness was 274.5m and this thick cover of pelagic ooze is made responsible for the high heat flow rates of averaged 215mW/m$^2$ in the area [Swift et al., 1998a].

An important implication in the interpretation of Poisson's ratio of the sedimentary layer is the fact that the modeled S-wave velocities for the sedimentary layers are constrained through the accuracy with which the sediment thickness was estimated from refracted and reflected P-wave arrivals (chapter 5.3.1). Also it has to be considered that calculated values of Poisson's ratio as well as the modeled velocities in the velocity-depth model are average values over a few hundred meters. Poisson's ratio for the uppermost sediment might be even higher than the illustrated values. Likewise the sediment directly above the basement may have reached a higher degree of compaction resulting in lower values for $\sigma$ than indicated. In Table 6.1 compressional and shear velocities as well as Poisson's ratios for various common sediment types are given. Values from Hamilton [1971] were measured on samples taken from the seafloor at sites with waterdepths of up to 1200m. Wilkens et al. [1992] performed inversion of acoustic logging data from DSDP site 613.

Poisson's ratios obtained for sedimentary layer at the profile across Malpelo Ridge are interpreted as unconsolidated calcareous ooze with a possible higher degree of compaction at depths exceeding 150-200m below seafloor.

### 6.0.2 Upper and Middle Crust

Poisson's ratio in the uppermost crust shows an extreme high of 0.4 at the northwestern ridge and varies from 0.38 to 0.34 below the central graben for layer 2A. Along the southeastern plateau values are lower, ranging from 0.36 to 0.28. This layer extends not along the whole profile but only to the northwestern end of Malpelo Ridge. Within layer 2B $\sigma$ ranges from 0.30 to 0.31 northwest off Malpelo Ridge. Underneath the central graben and southeast plateau values are differing between 0.28 to 0.29 with local maxima of 0.31 and minima of 0.25.

Salisbury and Christensen derived average values of $\sigma$=0.29 for metabasalts in the prehnite-pumpellyite facies and $\sigma$=0.30 for brecciated dikes in the Greenschist facies, supposed to build layer 2 of normal crust. It is a well known fact that Poisson's ratio for the upper crustal layers derived from seismic measurements are significantly higher than those calculated from laboratory measurements, e.g. Spudich and Orcutt [1980] determined Poisson's ratios of 0.32-0.38 for the uppermost crust. The higher values are attributed to a higher fracture porosity than detectable at a smaller scale. Collier and Singh [1998] calculated a porosity of 30% for the upper 500m of the basement at the East Pacific Rise. At DSDP site 504B also high porosity and permeability for the upper 200-300m of extrusives with $\sigma$ decreasing from 0.43 to 0.28 are reported [Swift et al., 1998a].

The low velocities and high values for Poisson's ratio in the uppermost layer 2A are attributed to high porosity and a high degree of alteration which indicates that the basalts have been erupted at shallow depths. A similar conclusion has been drawn by Lonsdale and Fornari [1980], who described samples taken from Malpelo Ridge as highly vesicular basalts. Since layer 2A only extends across the ridge the upper crust northwest off the ridge is suggested to have been formed at deeper levels or in a different environment.

Layer 2B is also interpreted as extrusives. With increasing depth porosity decreases and values of Poisson's ratio are becoming consistent with laboratory measurements for metabasalts. The slightly higher values northwest off the ridge are a consequence of the absence of layer 2A in this area, with the top of layer 2B exhibiting a higher porosity. The extreme high of Poisson's ratio at the northwestern ridge may be related to the steep-sided graben structures that have been described by Lonsdale and Fornari [1980] and that probably extend into this depth of the crust. Another explanation could be that the northwestern ridge is more highly weathered.

For layer 2C Poisson's ratio is 0.28 at the top and 0.26 at the bottom underneath the central graben. Values are lower east off the ridge ranging from 0.26 at the top to 0.24 at the bottom and northwest off the ridge with values ranging from 0.25 to 0.24.

These Poisson's ratios are somewhat lower than the measurements for metadolerite in the greenschist facies from the Bay of Islands Ophiolite Complex by Salisbury and Christensen [1978], ranging from 0.3 to 0.28. Spudich and Orcutt[1980] found $\sigma$ as low as 0.24 in a depth of 1.5km below basement which they also compared to measurements from the Bay of Islands Ophiolite. The only velocities which did correspond to their

values were quartz-rich trondhjemites, which they found to be an unsatisfactory explanation since trondhjemites are rarely found in sea floor dredge hauls. An alternatively suggested pore fluid effect did also not yield a reasonable result. At DSDP site 504B Poisson's ratio decreases below 0.25 at a similar depth. Swift et al. [1998] attributed this low Poisson's ratio zone to intermediate-scale (<1cm) and small-scale (<1mm) cracks with random or horizontal orientation that have been caused by by rapid expansion of circulated seawater by the intrusion of hot dikes. It is an important aspect that this zone of low Poisson's ratio is found directly above the decrease in compressional wave velocity marking the boundary between seismic layers 2 and 3. In the same depth interval the lithologic transition zone from extrusives to sheeted dikes occurs at DSDP site 504B where pillow lavas and flow basalts occur interchangeably with sheeted dikes. The zone with very low values of Poisson's ratio is assumed to mark the bottom of layer 2 and therefore the transition from seismic layer 2 to seismic layer 3. The seismic layer 2/3 boundary has been previously interpreted as the transition from sheeted dikes to gabbro or as an increase in metamorphic grade from greenschist to amphibolite facies [Salisbury and Christensen, 1978, Detrick et al., 1994]. At DSDP site 504B the layer 2/3 boundary occurs within the sheeted dike section and is associated with gradual changes in porosity and alteration [Detrick et al., 1994, Swift et al., 1998a]. Comparison of VSP reflectors and lithology in borehole DSDP 735B indicates also that the reflectors do not coincide with major changes in the physical properties of the drilled gabbros but in the presence of faults and fractures [Dick et al., 1999].

The introduction of water filled cracks, decreasing P-wave and S-wave velocity by disproportional amounts, results not only in low Poisson's ratios but also in abundant local extrema. Shearer [1988] found that Poisson's ratio for a rock with thick cracks with an aspect ratio $\alpha > 0.01$ is smaller than for the original rock whereas Poisson's ratio of a rock with thin cracks ($\alpha > 0.01$) is larger than for the original rock. The aspect ratio defines the ellipticity of pores, with an aspect ratio of $\alpha = 1$ representing a sphere and an aspect ratio of $\alpha = 0.01$ representing an ellipsoid with a ratio of the minor axis to the major axis of $1 : 100$ [Wilkens et al., 1991]. For the example of an oceanic basalt ($v_p$=6.28km/s, $v_s$=3.42km/s) the addition of $0.06\%$ porosity with aspect ratios of $\alpha = 0.001$ increases Poisson's ratio from $\sigma$=0.29 to $\sigma$=0.31.

Shaw [1994] introduced a porosity model for the upper crust consisting of populations of thin ($\alpha = 0.001$) and thick ($\alpha = 0.1$) cracks that vary independently with depth and represent porosities of 0.1% and 4%, respectively. At low depths both populations of cracks are present and the tendency to decrease $\sigma$ caused by thick cracks is balanced by the tendency to increase $\sigma$ by thin cracks. Poisson's ratio should remain within the normal bounds in this area. At greater depth thin cracks seal preferentially and thick cracks dominate the variation the $\sigma$ resulting in an anomaly characterized by low values. At even greater depth both thin and thick cracks are sealed, causing Poisson's ratio to return to values as published from ophiolite measurements. Calculations of Poisson's ratio in dependence of the amount of thin and thick cracks is illustrated in Figure 6.2 for a gab-

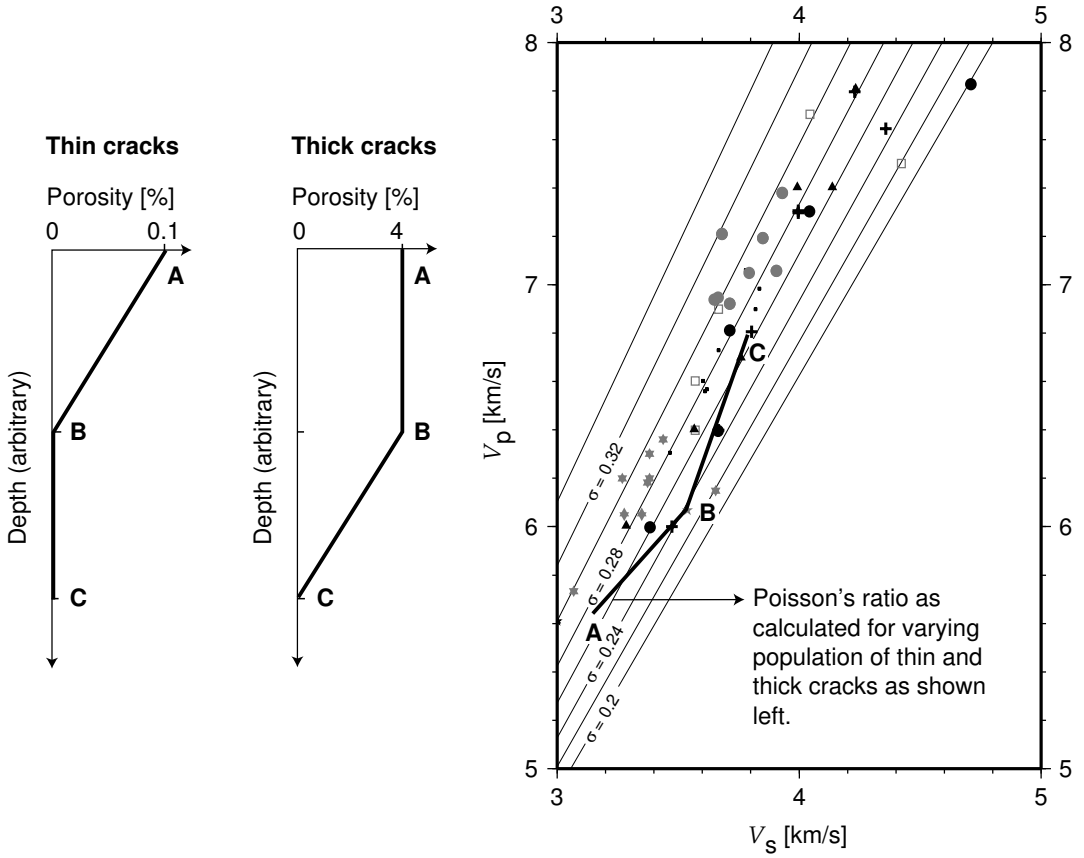


Figure 6.2: Effects of two populations of cracks on $v_p$ and $v_s$, and Poisson's ratio, using the theory of Kuster and Toksöz [1974]. At depth A thin and thick cracks are both present and the corresponding $\sigma$=0.276 agrees with laboratory values. At depth B, only the thin cracks have sealed, Poisson's ratio is anomalous $\sigma$=0.24. At depth C all cracks have sealed and velocities are that of the host rock (gabbro with $v_p$=6.21km/s, $v_s$=3.82km/s, $\sigma$=0.27. Symbols as in Figure 6.1. Modified after Shaw[1994].

bro host rock. The upper crust at OBH 92 displays a minimum of $\sigma$=0.24 at nearly the same velocity regime. Shaw [1994] additionally suggests that this model is only valid for young oceanic crust with ages younger than 15ma. In old crust, with ages of more than 60ma, cracks would be filled with secondary deposits and values for Poisson's ratio are more consistent and higher since closing of all cracks by the age of 60ma would cause seismic velocities and Poisson's ratios to return to agreement with laboratory measurements. Rock samples from Malpelo Island which have recently been dated, provide an age of 15.8 to 17.3ma [Hoernle et al., 2002], samples from Malpelo Ridge are dated at 10.7ma to 15.7ma [O'Connor et al., 2002]. Considering the tectonic history of Malpelo Ridge (chapter 2) crack porosity in the lower crust is likely to be preserved much longer than would be the case for undisturbed oceanic crust. Sealing of cracks could have been prevented due to a possible long-term influence by the Galapagos Hotspot or during the lateral displacement of Malpelo Ridge when separation from Cocos or Carnegie Ridge took place. Another possibility is a more recently reactivation of crack porosity due to

tectonic processes in the area (chapter 2.1).

Velocities and Poisson's ratios within layer 2C are comparable to metadolerites in the greenschist facies as described by Salisbury and Christensen [1978] and layer 2C is interpreted as the transition from pillows and basalt flows to sheeted dikes. The decrease in Poisson's ratio to values as low as $\sigma$=0.24 at the bottom of layer 2C is seen as a porosity effect marking the transition to layer 3.

### 6.0.3 Lower Crust

Along the profile values of Poisson's ratio in the lower crust vary significantly, dividing the profile into three distinct areas: the northwestern part northwest off the ridge, the central graben and southeastern plateau, and the area east off the ridge where OBH stations 96 to 90 are located. In this last area Poisson's ratio within the lower crust is nearly constant with values of 0.26 at the top and 0.29 at the bottom. Underneath the central graben values reach a minimum of 0.25 at the top and have a value of 0.29 at the bottom. The constant velocity area at the bottom of layer 3 (see also Figures 5.11 and 5.35) has a constant value of $\sigma$=0.28. Northwest off the ridge the gradient for Poisson's ratio is becoming negative, with higher values for $\sigma$ at the top and lower values at the bottom. Underneath OBS station 117 a $\sigma$ of 0.27 and 0.25 was found ath the top and bottom, respectively. Values are increasing in northwesterly direction with increasing distance to the ridge to $\sigma$=0.28 at the top and $\sigma$=0.27 at the bottom at OBS station 122.

Layer 3 was previously assumed to consist of gabbroic rocks of the amphibolite facies, e.g. metagabbro, pyroxene- and olivine-gabbro, with the olivine content increasing with depth. Data from DSDP site 504B show that the layer 2/3 boundary occurs within the sheeted dike section and is associated with gradual changes in porosity and alteration. It seems that at least the upper 400-800m of seismic layer 3 consist of dolerites and metadolerites [Detrick et al., 1994], with metagabbro, pyroxene- and olivine gabbro as expected subsequent lithologies. Salisbury and Christensen [1978] derived values of 0.26 to 0.31 for such a composition from top to bottom. Christensen [1996] reported average velocities $v_p$=6.98km/s, $v_s$=3.96km/s, and a Poisson's ratio of 0.263 for an amphibolite. Similar values and increasing Poisson's ratio with depth were reported form Au and Clowes [1984] for the upper part of layer 3 (layer 3A) as the $v_p - v_s$-path moves from metadolerite and metagabbro to pyroxene gabbro and olivine gabbro to a value of $\sigma$=0.29. They noted a decreasing Poisson's ratio with depth for layer 3B with increasing velocities. Decreasing $\sigma$ with depth has also been published from Collins et al. [1989] for a combined wide-angle refraction/reflection survey at DSDP site 504B. They derived $v_p$-velocities of 6.7-7.1km/s and $v_s$-velocities of 3.8-4.1km/s for the middle and lower crust, which is equivalent to Poisson's ratios of 0.26-0.25. Their preferred velocity-depth model contained a low velocity layer at the bottom of the lower crust, , for which no evidence could be found in the data across Malpelo Ridge.

Christensen [1996] described changes in Poisson's ratio with metamorphic grade.

Mafic rocks in the greenschist and amphibolite facies exhibit a $\sigma$=0.26 that increases to $\sigma$=0.28 when granulite facies, which appears at temperatures between 700-800°C and pressures between 2-10kbar, becomes stable. At DSDP Hole 735B high-temperature granulite to amphibolite facies alteration was the most important of various alteration stages preserved in the drilled sections [Dick et al., 2000]. Results from various ocean drilling projects show that alteration of oceanic crust generally follows a certain sequence of events. Plastic deformation and metamorphism at high temperatures is followed by brittle deformation and the circulation of fluids, which is associated with cooling and further alteration at lower temperatures, e.g. in the greenschist and amphibolite facies. It is suggested that the lower crust becomes impermeable as it is transported away from the spreading ridge which forces alteration to cease at temperatures of between 80-300°C [Humphries, 1995].

For the thickened crust originated at the Galapagos Hotspot, cessation of alteration probably occurred at higher temperatures since the closing of possible cracks and hence the impermeability of the crust would be reached at shallower depths than the bottom of layer 3. The data underneath the central graben and the southeastern plateau are consistent with a transition from metadolerites to gabbros to mafic granulites. Metamorphism of mafic rocks in the granulite facies at low pressures produces granulites consisting of mainly orthopyroxene, clinopyroxene, plagioclase, hornblende and olivine, with $v_p$=7.29km/s, $v_s$=4.04km/s, and $\sigma$=0.278 [Christensen, 1996]. Such a low pressure granulite facies regime would be found at depths between 10-15km below basement, with pressures ranging from approximately 3-5kbar. The Malpelo Ridge model shows nearly the same velocities and slightly higher values for $\sigma$ in the lower crust (layer 3A) between OBS stations 90 and 115, where the crust is thickened. Layer 3B, which is found at depths between 15-20km below basement, has a slightly decreased Poisson's ratio of 0.28. For mafic rocks formed in medium-grade granulite facies with pressures between 5-7kbar, garnet ($\sigma$=0.27) becomes one of the main constituents, which forces Poisson's ratio to decrease [Christensen, 1996].

The decreasing Poisson's ratio with depth in the area northwest off the ridge is more difficult to explain. At the top of layer 3 below OBS stations 116-122 values for $\sigma$ correlate well to the values from the Bay of Islands Ophiolite Complex. Figure 6.3 shows the same data points as Figure 6.2 in relation to a velocity trend for gabbro/diabase after Carlson and Miller [1997]. As can be observed the velocities at the top of layer 3 for $v_p \geqslant$6.8km/s plot within the error limit of the trend. Values at the bottom of layer 3 deviate for OBS 121 for P-wave velocities higher 7.2km/s. In this area northwest off the ridge, a total crustal thickness of 5-6km was modeled, indicating normal oceanic crust. Poisson's ratio of 0.25, as encountered at the bottom of the lower crust underneath OBS station 117, are usually attributed to ultramafic rocks like dunites and peridotites that are assumed to build the upper mantle. Crustal rocks with Poisson's ratio $<$0.25 have mostly quartz-rich compositions, e.g. Kern and Richter [1981] published a value of $\sigma$=0.243 for an amphibole gneiss sample at 6kbar pressure and a temperature of 710°C. For oceanic

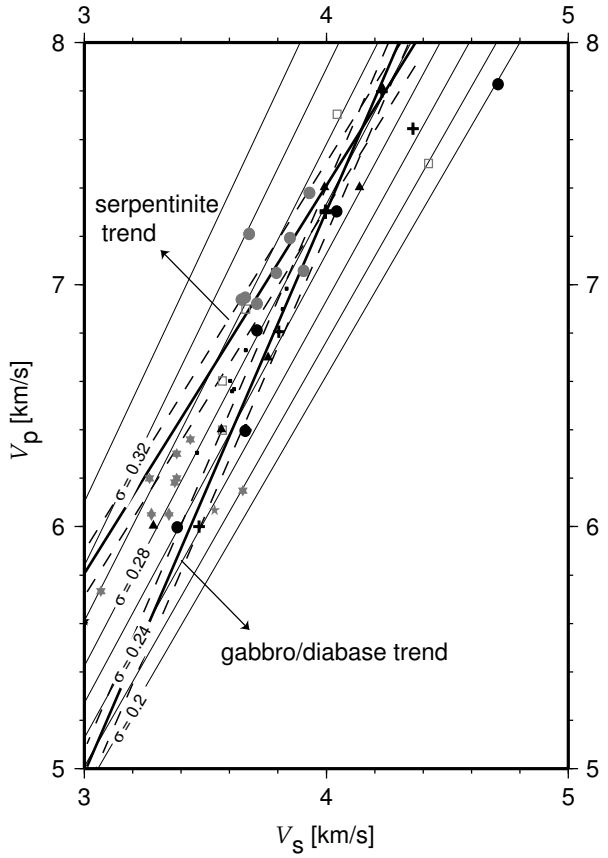


Figure 6.3: Gabbro/diabase trend and serpentinite trend for oceanic crust, taken from Carlson and Miller [1997]. Symbols as in Figure 6.1. Dashed lines denote the error limit of the trends.

crust such a lithology is not reasonable. Although at DSDP site 735B a variety of felsic rocks was described within the gabbronorites and olivine gabbros, they did not contribute more than 0.5% of the core composition [Dick et al., 1999]. A more plausible explanation can be inferred from the relation between Magnesium (Mg) content, Iron (Fe) content, and Poisson's ratio. An increase in Mg content in pyroxenes and olivines due to iron-magnesium (Fe-Mg) substitution will increase $v_p$ and $v_s$ disproportionally, resulting in a decreased Poisson's ratio. Within the orthopyroxene family with its Mg-rich and Fe-rich endmembers enstatite ($Mg_2Si_2O_6$) and ferrosilite ($Fe_2Si_2O_6$) Poisson's ratio increases from 0.209 for enstatite to 0.28 for orthoferrosilite. Similar values have been published for the olivine series ranging from $\sigma$=0.24 for forsterite ($Mg_2SiO_4$) to $\sigma$=0.336 for fayalite ($Fe_2SiO_4$) (chapter 4).

Gabbros contain a high amount of pyroxenes and olivine and an enrichment in the Mg-rich endmembers of the orthopyroxene and olivine families after crystallization can probably explain the low values of $\sigma$ observed in the lower crust between the Malpelo and Regina Ridges. Chemical analyses of samples from Malpelo Ridge taken from Lonsdale and Fornari [1980] are described as iron-rich tholeiitic basalts (Figure 6.4) with MgO ranging between 5.7-7.1%, measurements on samples taken during PAGANINI Cruise SO144-3 resulted in similar values [Werner et al., 2002]. Diabase samples from DSDP site 504B were classified as olivine tholeiites (Figure 6.4) that were characterized by

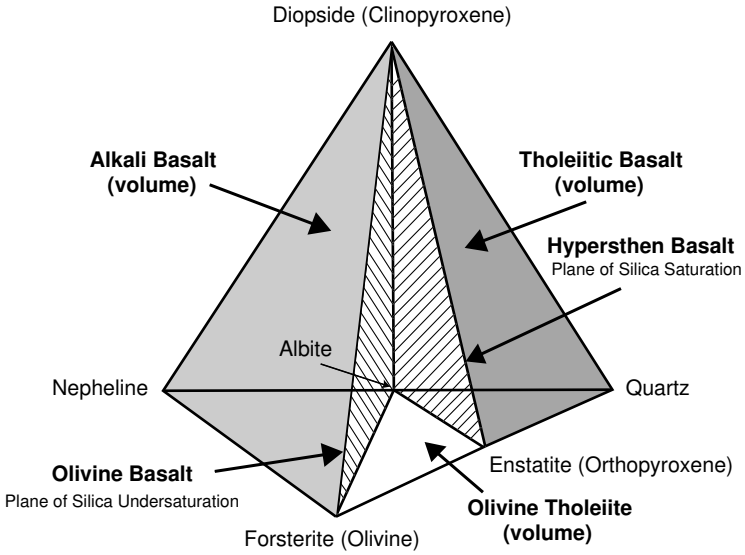


Figure 6.4: Mineralogical classification of basalt after Yoder and Tilley [1962].

7.7-10.1% MgO, and the chemical composition does not vary significantly with depth throughout the sampled crustal sections [Dick et al., 1992]. Mid-Ocean-Ridge Basalt usually has MgO levels in the 9% range and it has to be expected that most magma undergoes fractionation due to separation of olivine crystals. The magma which makes its way to the sea floor is primarily the residual melt produced by this fractionation process and the MgO content in the lower crust and upper mantle may be higher than the values measured from samples taken from the seafloor.

Published values for the Mg-number (Mg#), which is the magnesium content normative to the magnesium and iron content ($Mg\# = Mg/(Mg + Fe^{2+})$), range from 0.6 to 0.75 for DSDP site 504B [Dick et al., 1992]. At DSDP site 735B Mg-numbers for gabbro and olivine gabbro range between 0.72 to 0.79 with a corresponding MgO content of 7.38-10.23% [Dick et al., 1999]. For the samples taken at Malpelo Ridge during PAGANINI Cruise SO144-3 [Werner et al., 2002], no values for the Mg# have been published yet, but the MgO content of 4.5-8% indicates a lower Mg# than for DSDP site 504B. Under the assumption that the oceanic crust northwest off the ridge, where OBS stations 116-122 are located, had been formed at the Galapagos Spreading Center, it should display a similar chemical characterization as the crust at DSDP site 504B. The difference in MgO content between the two types of crust of a few percent is sufficient to account for the generally lower Poisson's ratio northwest off the ridge, which decreases with increasing depth as pyroxenites and olivine become more abundant. A higher MgO content in this part of the crust than the published values for DSDP site 504B seems unlikely. White and McKenzie [1989] showed that the MgO content is indicative of the temperature in the asthenosphere where the melt originated. Asthenosphere with a normal potential temperature of about 1280°C produces melt with the composition of Mid-Ocean-Ridge Basalts (MORB) as at DSDP site 504B. Increasing the temperature by 200°C increases the percentage of MgO from about 10% to 18%, but also results in a thickened crust as is illustrated in Fig-

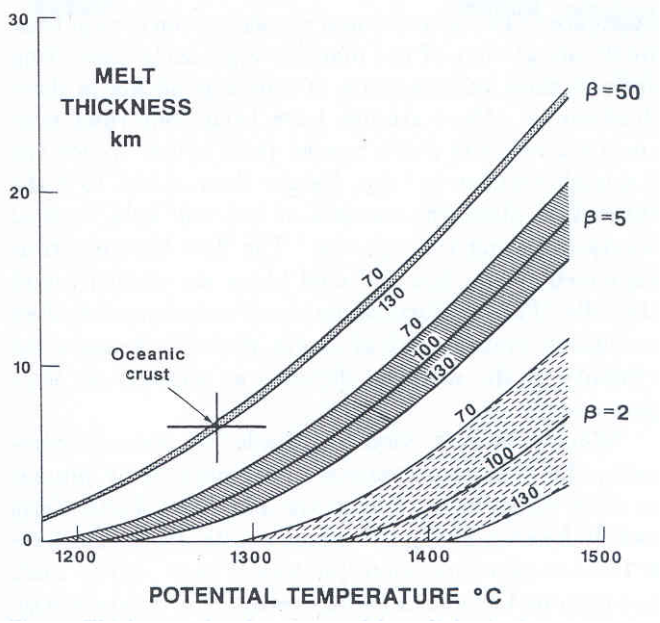


Figure 6.5: Thickness of melt generated by adiabatic decompression of asthenospheric mantle over a range of potential temperatures. Curves are shown for initial thicknesses of the mechanical boundary layer of 70, 100, and 130km, with thinning factors $\beta$ of 2, 5, and 50. Stretching factors of 50 are representative of the upwelling of asthenosphere which occurs beneath oceanic spreading centers. Cross shows limits on normal asthenospheric temperatures. From White and McKenzie [1989].

ure 6.5. Thinning the lithosphere by a factor 2 above the asthenosphere with 1480°C would produce alkali basalts passing to tholeiitic basalts as stretching is increased further [White and McKenzie, 1989]. As mentioned earlier, samples taken from Malpelo Ridge, which is supposed to originate from the Galapagos Hotspot, had been described as tholeiitic basalts. The average crustal thickness northwest off the ridge is 5-6km, which falls within the range for normal oceanic crust produced at temperatures between 1262°C and 1295°C.

The estimated temperature anomaly in the asthenosphere for the Galapagos Hotspot is about $+200$°C. Today the hotspot is located 170km south of the Cocos-Nazca Spreading Center with a transform fault at $91°W$ being the point closest to the hotspot. Ito and Lin [1995] estimated a temperature anomaly of $+50\pm25$°C for the spreading center near this point from variations in mantle Bouguer anomalies and bathymetry. The associated temperature gradient is 0.74-1.03°C/km. The temperature influence for a distance of 10km to 40km as in the area northwest off Malpelo Ridge would be associated with temperature anomalies of 159-192°C and crustal thicknesses of about 20km. If the oceanic crust northwest off the ridge and Malpelo Ridge have been formed simultaneously an off-axis distance of the hotspot of about 170km would be needed to account for the observed crustal thicknesses of 5-6km.

It has to be noted that although Ito and Lin [1995] related the observed gravity anomalies in terms of increased temperatures and a thickened crust of $3\pm1$km they also stated the possibility that a decreased Fe/Mg ratio towards the transform fault could similarly influence gravity measurements resulting in a significant decrease in their estimates for temperature and crustal thickness.

In consistency with findings from DSDP site 504B that the upper part of seismic layer 3 consists of metadolerites of the sheeted dike section, the top of the lower crust in the

Malpelo model is interpreted as such, underlain by metagabbros, pyroxenegabbros and olivinegabbros (from top to bottom). Beneath the central graben and southeast plateau, where thickness of the upper and middle crust reaches 5km, a higher degree of metamorphism is proposed that ranges from the amphibolite facies at the top of layer 3 to the granulite facies at depths between 10-15km below seafloor. Layer 3B, which was modeled at a depth of 15-20km below basement, is suggested to comprise higher amounts of garnet as found in granulite facies at higher pressures.

The decreasing Poisson's ratio with depth in the area northwest off the ridge is attributed to a generally higher Mg content for this part of the crust. As orthopyroxene and olivine become more abundant with increasing depth, Poisson's ratio tends to decrease. The gradually increasing Poisson's ratio towards the northwestern end of the profile may be associated with a decreasing Mg content and increasing Fe content, which can be related to a gradually cooler melt with increasing distance from a high temperature source, which is probably the Galapagos Hotspot.

### 6.0.4 Upper Mantle

Below the southeastern plateau and central graben Poisson's ratio is nearly constant with a value of $\sigma$=0.28, ranging from 0.282 at the top of the layer to 0.278 at a depth of 30km. Again, there is a significant change northwest off the ridge, which is also accompanied by a gradient change. From OBS station 117 to 122 values of 0.20 at the top and 0.22 at higher depth are observed. These values are rather low, Collins et al. [1989] derived a value of 0.23 ($v_p$=8.1km/s, $v_s$=4.74km/s), they could not identify any Pn or Sn arrivals on their data and had to estimate upper mantle velocities indirectly. A decrease of Poisson's ratio across the Moho is normally observed, though [Spudich and Orcutt, 1980, Cheung and Clowes, 1981, Au and Clowes, 1984]. In Table 6.2 compressional and shear wave velocities as well as obtained Poisson's ratios for the upper mantle published from various authors are given. Unfortunately most of them could not utilize Sn-refractions to obtain mantle S-wave velocities and had to rely on indirect estimates. While Cheung and Clowes [1981] identified a Sn-phase on their data, the transition from lower crust to upper mantle was only accompanied by a change in velocity gradient. They interpreted the upper mantle to have an average P-wave velocity of 7.4km/s and an average S-wave velocity of 4.3km/s, resulting in $\sigma$=0.24 with extremal bounds of $\sigma$=0.2-0.3. Mjelde [1992] reported $v_p$=8.2km/s and $v_s$=5.1km/s, obtained through forward modeling of an refracted mantle phase Sn, resulting in a Poisson's ratio of 0.18 from a refraction experiment on the continental shelf in Norway.

Salisbury and Christensen also obtained Poisson's ratios of 0.23 to 0.25 for the ultramafics compiling the upper mantle. The samples were classified as serpentinized dunite and harzburgite. Velocities were calculated from modal analysis to obtain values for unaltered samples for a pressure equivalent to a depth of about 7km below seafloor. Kern and Richter [1981] obtained $\sigma$=0.29 for a dunite sample with $v_p$=7.9km/s and $v_s$=4.3km/s

| | Profile | **v $_p$[km/s]** | **v $_s$[km/s]** | **Poisson's ratio** |
|---|---|---|---|---|
| **Spudich & Orcutt** | FF2 | 7.84 | 4.5 | 0.25 |
| | FF4 | 7.93 | 4.5 | 0.26 |
| **Cheung & Clowes** | | 7.4 | 4.3 | 0.24 |
| **Au & Clowes** | EX2 | 7.5 | 4.5 | 0.22 |
| | EX3 | 8.3 | 4.6 | 0.28 |
| **Mithal & Mutter** | NE9B5 | 8.4 | 5.05 | 0.22 |
| **Collins et al.** | | 8.1 | 4.74 | 0.23 |

Table 6.2: Oceanic mantle velocities and Poisson's ratios from published data. Data are taken from Spudich and Orcutt[1980], Cheung and Clowes [1981], Au and Clowes[1984], Mithal and Mutter [1989], and Collins et al. [1989].

and similar values for eclogite with $v_p$=7.7km/s, $v_s$=4.2km/s and $\sigma$=0.28 at 6kbar pressure and 710°C.

The near constant value for Poisson's ratio of 0.28 and the modeled velocities of $v_p$=7.8km/s and $v_s$=4.3km/s underneath the central graben and southeastern plateau are within the range of published values for dunites and peridotites. An interpretation as eclogite is not favoured, since metamorphism in the eclogite facies needs pressures higher than 10kbar which are, in the oceanic environment, usually only encountered in subduction zones. Figures 6.6 and 6.7 display the classification after Streckeisen [1978] for ultramafic rocks consisting essentially of olivine, orthopyroxene, and clinopyroxene. Dunite and harzburgite belong to the olivine and orthopyroxene rich members, dunite with an olivine content of more than 90%. As for the lower crust, a melt enriched in Mg can be invoked to explain the low Poisson's ratios observed northwest off the ridge, at least to some extent. The lowest possible value of Poisson's ratio for a dunite consisting purely of the Mg-rich endmember forsterite of the olivine series has a $\sigma$=0.24. Harzburgite may reach lower values due to its higher orthopyroxene content, but values as low as the encountered $\sigma$=0.20-0.22 are unreasonable. The crucial point in the interpretation of the low Poisson's ratios in the upper mantle northwest off the ridge are the high shear wave velocities of 4.8-4.9km/s modeled there in combination with relatively low P-wave velocities of 7.8-7.9km/s. Shear wave velocities of 4.8-4.9km/s have been published from Simmons [1964] for dunite samples at pressures up to 10kbar, but no accompanying measurements of P-wave velocities are available for these data. Calculation of P-wave and S-wave velocities of dunite, peridotite and eclogite at various pressures and temperatures using pressure and temperature derivatives from Kern and Richter [1981] did also not yield comparable values.

Instead of interpreting the observed values of $\sigma$ in terms of petrological composition possible fracturing and porosity have to be considered as well. Spencer and Nur [1976] showed that the presence of fluids at low pore pressure at elevated temperatures tends to decrease Poisson's ratio significantly. Increasing the temperature of a sample that con-

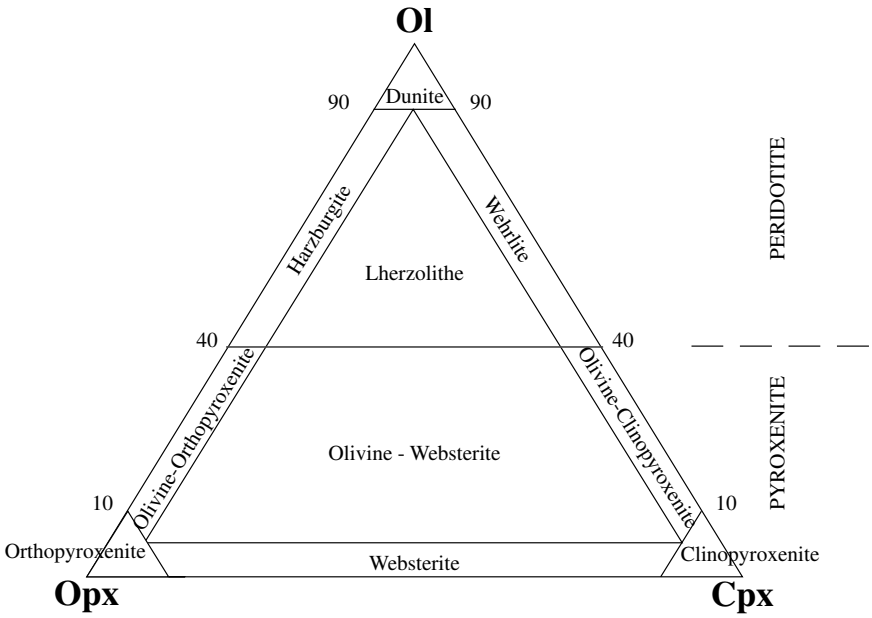


Figure 6.6: Classification and nomenclature of ultramafic rocks based on the proportion of olivine (Ol), orthopyroxene (Opx), clinopyroxene (Cpx) after Streckeisen [1978].

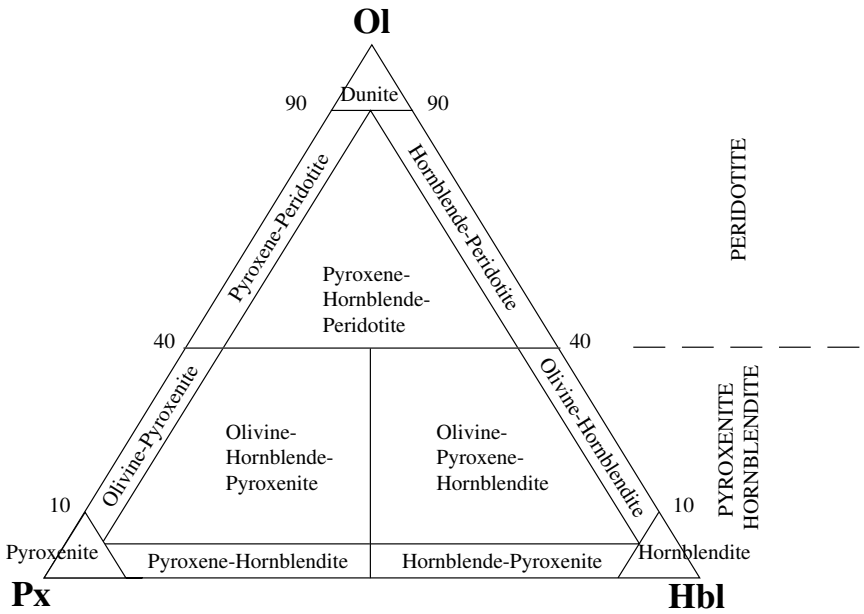


Figure 6.7: Classification and nomenclature of ultramafic rocks based on the proportion of olivine (Ol), pyroxene (Px), and hornblende (Hbl) after Streckeisen [1978].

tains pore water at low pressure decreases $v_p$ while $v_s$ remains nearly unchanged. It is only sensitive to the temperature of the matrix. For high pore pressures $v_p$ is less affected while $v_s$ is decreased, resulting in a higher Poisson's ratio. Measurements were done at confining pressures of 1kbar and at temperatures up to 300°C and lowered Poisson's ratio of a granite sample from $\sigma$=0.245 to $\sigma$=0.173 [Spencer and Nur, 1976]. A similar effect

could lower Poisson's ratio in the upper mantle from 0.23-0.25, as would be expected for a dunite with a high Mg-content, to 0.2-0.22, as observed in the model. Crustal thickness in the area northwest off the ridge ranges from 5-6km with pressures of about 2kbar. Open cracks and fractures should be closed at pressures higher than 2kbar, a pressure which is reached at a depth of about 7km below seafloor. Hydrothermal circulation of seawater in the upper crust is believed to control thermal heat flow from oceanic lithosphere [Kearey and Vine, 1999], but it is not known exactly how far this convection penetrates into the crust. A tectonic mechanism could maybe explain the existence of porosity in the upper mantle. Another point that has to be considered is that if fluids would be present in the upper mantle serpentinization of peridotites and dunites would be expected. Since serpentinization of a dunite causes Poisson's ratio to increase significantly up to values of 0.36 [Christensen, 1996] the contrary effect of an increasing Poisson's ratio would be observed. O'Reilly et al. [1996] showed that a water column of 200-400m at low temperatures of about 500°C is necessary to hydrothermally alter a mantle peridotite with $\sigma$=0.25 to a serpentinized peridotite ($\sigma$=0.28) consisting of 15-20% serpentinite. Heat flow distribution in the Eastern Panama Basin shows values of about 3 H.F.U., which is equivalent to about 120mW/m$^2$, near and across Malpelo Ridge [Andel et al., 1972]. At DSDP site 504B heat flow was average 215mW/m$^2$ and temperatures in the borehole reached 150°C at 1400mbsf with a thermal gradient of 61°C/km [Dick et al., 1992, Swift et al., 1998a]. For the oceanic crust northwest off Malpelo Ridge a similar thermal conductivity can be assumed as for the lithology observed at DSDP site 504B which results in temperatures as low as 200-300°C at the top of the upper mantle northwest off the ridge. Since the low Poisson's ratios observed in the data imply that no serpentinites are existent in the upper mantle, the conclusion has to be drawn that either porosity does not extend into this depth or that the temperatures in this region may be higher.

Low P-wave velocities in the upper mantle are sometimes considered to be indicative of partial melt, but apart from the fact that heat flow measurements do not indicate any asthenospheric upwelling in this region of the Eastern Panama Basin, the associated high S-wave velocities disqualify this possibility. The existence of partial melt in the upper mantle would lower S-wave velocities by a higher amount as the corresponding P-wave velocities, resulting in increased Poisson's ratios [Hammond and Humphreys, 2000].

This raises the question of how reliable the data in this depth are. Mjelde [1992] observed a S-wave mantle reflection SmS that propagated with different velocities for near vertical to wide angle incidence. As possible explanation for this deviation, besides lateral heterogeneity or the existence of an S-wave Moho that does not coincide with the P-wave Moho, he considered anisotropy in the lower crust causing S-wave velocity to increase with increasing angle of incidence. He calculated a value of 14% anisotropy for the lower crust. In the data across Malpelo Ridge no evidence for anisotropy higher than 3% in the lower crust or upper mantle was found, but the data along the profile could be misleading (chapter 5.5). Anisotropy in the upper mantle has been reported from various authors [Clowes and Au, 1982, Holbrook et al., 1988, Clement et al., 1994] and is related

to the preferred orientation of olivine crystals with the direction of maximum P-wave and S-wave velocity being approximately parallel to the direction of seafloor spreading. E.g. Au and Clowes [1984] derived Poisson's ratios of 0.22 and 0.28 for two profiles oriented perpendicular and parallel to spreading direction which was attributed to anisotropy in the upper mantle (Table 6.2 and chapter 5.5). If such anisotropy would exist in the data across Malpelo Ridge and be not detectable due to the orientation of the profile (chapter 5.5), the observed velocities in the model would represent average velocities and the observed Poisson's ratios would represent average Poisson's ratios, respectively. This means that values for $\sigma$ in the upper mantle would be possibly higher on a profile perpendicular to spreading direction, but even lower for a profile parallel to spreading direction. During the discussion an anisotropy of 1-3% for the upper mantle was assumed, with values of Poisson's ratios representing average values that may be interpreted in terms of petrological or lithological composition of the crust and mantle.

The upper mantle is interpreted to consist of ultramafic rocks as dunite and peridotite in the granulite facies underneath the central graben and southeastern plateau. Northwest off the ridge an enrichment in Mg content, suggesting a different melt in this area, is proposed. There is no indication of serpentinization which is associated with the lack of porosity in the upper mantle. The very low Poisson's ratio of $\sigma$=0.20 can not be explained completely.

# Discussion and Outlook 7

The oceanic crust of Malpelo Ridge is divided into four distinct layers: Layer 2A is interpreted as extrusives with a high porosity due to their probable eruption at shallow depths. This layer does not extend into the area northwest off Malpelo Ridge which is considered as the first indication that the crustal layers between Regina and Malpelo Ridges (Figure 7.4) have been formed in a different environment. Layer 2B extends along the whole profile and exhibits a decrease in porosity with increasing depth, which is attributed to the progressive filling of cracks with alteration minerals, and Poisson's ratios can be correlated with extrusive metabasalts as pillows and lava flows. Layer 2C shows very low Poisson's ratios that are proposed to mark the beginning transition to layer 3 and is accordingly interpreted as a transition zone to the sheeted dike complex in the Greenschist Facies, composed of intermixing extrusives and intrusive dikes.

Figures 7.1 to 7.3 display velocity-depth profiles accompanied by the interpreted lithology for the three representative stations (chapter 6, Figure 6.1) along the profile across Malpelo Ridge. The position of the OBS stations on the profile is also shown in Figure 7.4.

Modeling of layer 3 further confirmed the assumption that the crust beneath the central ridge and southeastern plateau has a different origin than the oceanic crust northwest off the ridge. This is not only indicated by the abnormal thickened crust below Malpelo Ridge but also by differences in the chemical composition of the interpreted lithology. Layer 3 is proposed to consist of metadolerites of the sheeted dike complex that are underlain by metagabbros, pyroxene gabbros, and olivine gabbros. The transition from the metadolerites of the sheeted dike section to gabbros is not evident from the seismic data and is assumed to occur within the upper 1km of layer 3 [Detrick et al., 1994]. Beneath Malpelo Ridge an increasing grade of metamorphism from amphibolite to low-grade granulite facies with increasing depth is suggested, which is consistent with results from DSDP Hole 735B [Dick et al., 2000]. Layer 3B, which only extends beneath the central ridge, is interpreted to represent gabbros in the medium-grade granulite facies (Figure 7.2). The upper mantle also exhibits differences in chemical composition between Malpelo Ridge and the area northwest off the ridge. It is proposed to consist of ultramafites, as would be expected, but again with a higher Mg content northwest off the ridge (Figure 7.1). Northwest off the ridge the overall crustal thickness ranges from 5km to 6km and layer 3 is suggested to contain a higher amount of Mg which decreases with increasing distance from Malpelo Ridge.

The upper mantle beneath Malpelo Ridge (Figures 7.2 and 7.3) is proposed to contain a lower Mg content in favour of an increased Fe content and may exhibit a different mineralogical composition additionally, e.g. higher amounts of hornblende and clinopyroxenite

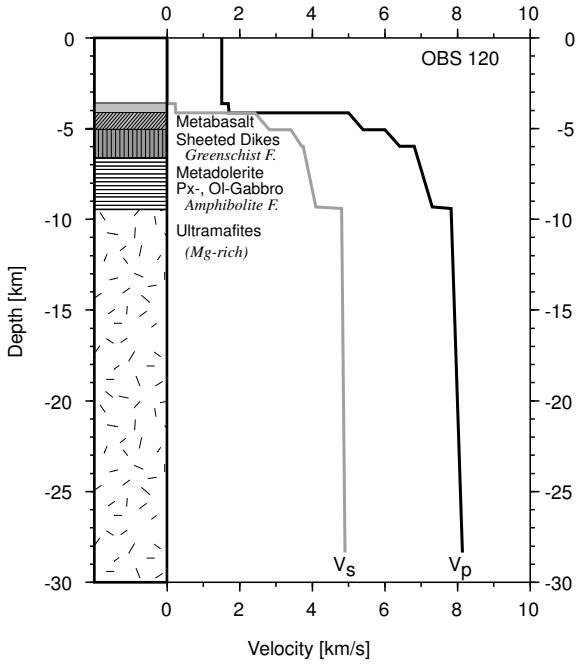


Figure 7.1: Velocity-depth profile and interpretation of layering at the location of OBS 120, situated in the area between Malpelo and Regina Ridges. The ultramafic section is suggested to consist mainly of orthopyroxenite and olivine-orthopyroxenite due to the low Poisson's ratios in the upper mantle. Magnesium(Mg)-rich is defined as compared to the area beneath Malpelo Ridge (Figures 7.2, 7.3). Location of the OBS is shown in Figure 7.4.

instead of olivine and orthopyroxenite. The degree of alteration also varies between these two areas due to the difference in crustal thickness observed. No evidence for serpentinization or porosity was found in the upper mantle.

The emplacement of large volumes of magma originating from hotspot volcanism in intraplate settings is often associated with magmatic underplating. Evidence for underplating has been detected e.g. from Charvis et al. [1999] and Grevemeyer et al. [2001]. No similar evidence was found in the data across Malpelo Ridge. Compressional and shear wave velocities and resulting Poisson's ratios in the thickened crust underneath the central ridge and southeastern plateau are not varying significantly along the profile and the lower crustal anomaly is only expressed by thickness, therefore it is assumed that the petrological composition in this area is laterally homogenous. As for the lower crust underneath Cocos Ridge, no underplating as defined by "magmatic material added at the base of a pre-existing crust" [Walther, 2001b] is suggested. That no P-wave velocities higher 7.5km/s were encountered in the lower crust supports this interpretation, since underplating is generally considered to be associated with velocities higher 7.5km/s.

Thickening of the crust is nearly confined completely to the lower crust, the Moho reaches its maximum depth of 20km below basement beneath OBS 110. The maximum crustal thickness occurs directly below the central graben, which is suggested to be indicative of thermal buoyancy of the hotspot mantle plume and uplifting of the thickened lower crust during its emplacement. The existence of a very similar central graben along Cocos Ridge that is also centered above thickened lower crust [Walther, 2001b] has been first described by Lonsdale and Fornari [1980]. That the maximum depth of the Moho at Malpelo Ridge is also found below the central graben supports the interpretation of the origin of the central graben of Walther [2001a] in terms of uplifting instead of a relation

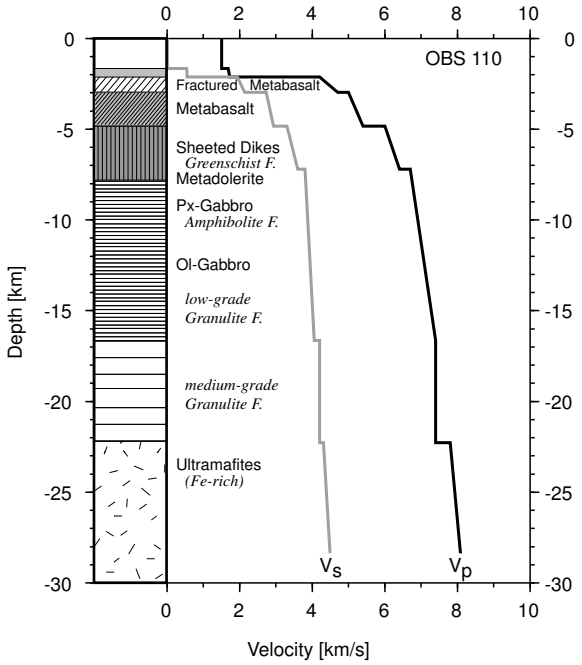


Figure 7.2: Velocity-depth profile and interpretation of layering at the location of OBS 110, situated above the central Malpelo Ridge. The ultramafic section in this area is proposed to contain a lower magnesium and higher iron content compared to the area northwest off the ridge (Figure 7.1). Location of the OBS is shown in Figure 7.4.

to the ongoing subduction of Cocos Ridge.

Another similarity to Cocos Ridge is found in the asymmetric thickness of the upper crustal layers northwest off the ridge and east off the southeastern plateau. Northwest off the ridge layer 2 reaches a maximum thickness of 2km whereas beneath OBH 96 to OBH 90 a maximum thickness of 4.5km is encountered. The thickness east off the southeastern plateau reduces to 3.5km if layer 2A, which was not modeled northwest off the ridge, is not considered. This remarkable difference in upper crustal thickness could be caused by a different crustal composition due to a spatial zonation of the Galapagos plume resulting in different magma types as proposed by Hoernle et al. [2000]. Walther [2001a] also discusses variation in the age of the oceanic crust overprinted by the hotspot, with the thinner upper crust being correlated to a younger age. At Malpelo Ridge no such correlation was indicated. A preliminary velocity-depth model of a recently acquired seismic wide-angle profile across Carnegie Ridge [Flueh et al., 2001] seems to exhibit a similar asymmetry with the oceanic crust being thinner north of the ridge.

The crust-mantle boundary also exhibits strong asymmetry: In northwestern direction the maximum depth of the Moho is reached within an offset of 40km whereas southeast of OBS 110 thickening of the lower crust extends over 100km. Walther [2001b] related a similar feature encountered at Cocos Ridge to the existence of nearby fracture zones. North of Malpelo Ridge a possible fracture zone could be situated along the Regina Ridge and Sandra Seamount, striking in NEE direction (Figure 7.4). Werner et al. [2002] suggest the existence of an abandoned spreading center in this area. Hardy [1991] also proposed the existence of an abandoned spreading center at $5°N$, east of $79°W$, that forms part of the southern boundary of a separate Coiba or North-Nazca Plate in the Eastern Panama Basin.

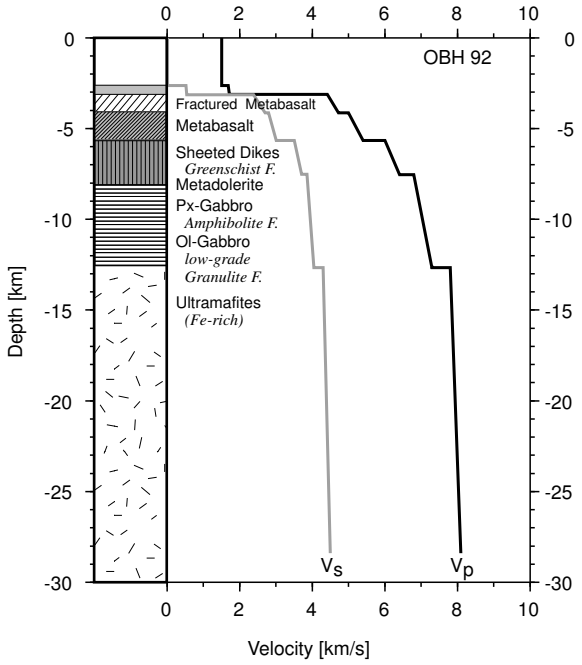


Figure 7.3: Velocity-depth profile and interpretation of layering at the location of OBH 110, situated at the eastern end of the profile. The ultramafic section in this area is also suggested to contain a higher Fe content compared to the area northwest off the ridge (Figure 7.3). Location of the OBH is shown in Figure 7.4.

Malpelo Ridge is considered to be one of the oldest parts of a hotspot track originating from the Galapagos Hotspot, as Carnegie and Cocos Ridge. It has been suggested to be either a former continuation of Cocos Ridge that was later transferred south along the Panama Fracture Zone [Hey, 1977] or to represent part of Carnegie Ridge that was rifted north [Lonsdale and Klitgord, 1978, Pennington, 1981, Hardy, 1991].

Samples taken from Malpelo Island were recently dated at an age of 15.8-17.3ma [Hoernle et al., 2002], samples taken from Malpelo Ridge were dated at 10.7-15.7ma [O'Connor et al., 2002]. The oldest magnetic anomalies identified south of Malpelo Ridge were identified as anomaly 5B (Figure 7.4), which represents an age of about 15ma. The younger dates of the investigated samples of Malpelo Ridge may be consistent with a long-term influence of the Galapagos Hotspot. It is not known exactly how long the hotspot could have influenced the melt temperature at the spreading center, possible long-term influences of a few million years are proposed from various authors, e.g. Kopf et al. [2001] demonstrate an activity of the hotspot mantle plume 6ma longer than the termination of the dominant construction phase of the Ninetyeast Ridge.

The interpretation of the seismic wide-angle model across Malpelo Ridge suggests a different chemical melt composition for the oceanic crust northwest off the ridge and the thickened crust beneath Malpelo Ridge. It is proposed to exhibit a higher Mg compared to the crustal layers of Malpelo Ridge, and furthermore, Poisson's ratio indicate a gradually cooler melt in direction towards Regina Ridge in this area. This implies that during the time period the oceanic crust northwest off the ridge was formed, an additional "high temperature source" was located near the spreading center. This "high temperature source" is probably the Galapagos Hotspot, and its influence became weaker with increasing dis-

tance from the rift zone, or, in other words, with ongoing spreading the hotspot and the spreading center were moving away from each other, resulting in a cooler melt at the rift zone. At the time these processes happened, the hotspot must have been located south of the rift zone.

The Galapagos Hotspot is assumed to exhibit a positive mantle temperature anomaly of about 200°C [Ito and Lin, 1995] today, accompanied by a temperature anomaly of $+50\pm25$°C at the Cocos Nazca Spreading Center at an off-axis distance of 170km from the hotspot. The crustal thickness northwest off the ridge of 5-6km seems to be associated with normal melt temperatures near 1280°C [White and McKenzie, 1989] and a comparable distance from the hotspot when spreading occurred. Simultaneous spreading and emplacement of the ridge would probably result in a much stronger influence of the hotspot than indicated by the data, e.g. a higher temperature of the melt during spreading would be associated with a thicker crust. Considering a possible long-term influence of the Galapagos Hotspot, it is proposed that the oceanic crust between Malpelo and Regina Ridges has been formed after emplacement of Malpelo Ridge took place. The encountered variation in the Mg content with increasing distance from Malpelo Ridge is attributed to temperature anomalies of about 40 - 10°C, decreasing with increased distance from the ridge.

There are some uncertainties remaining, e.g. the low Poisson's ratios indicate a high Mg content in this area, though, which should be attributed to a higher melt temperature and a correlated higher thickness of the crust. Subsequent thinning of the crust northwest off the ridge due to extensional processes would be probably associated with serpentinization, for which no evidence was detected in the data. Contrarily the thickened crust and upper mantle beneath Malpelo Ridge, which originates from the Galapagos Hotspot, exhibits relatively high Poisson's ratios interpreted in terms of a low Mg content and high Fe content which is consistent with geochemical analyses of samples taken from the ridge. Additional factors influencing the chemical composition of the lithology in crust and upper mantle are e.g. mantle flow, melt depletion, heat loss in the mantle, disequilibrium melting and fractionation, and a possible spatial zonation of the Galapagos plume. The interplay of these factors may be very complex and a more comprehensive understanding of these factors is needed to explain the discussed uncertainties. E.g. measurements of the natrium (Na) content could provide additional constraints, since the percentage of $Na_2O$ is a very sensitive measure of asthenosphere temperature [White and McKenzie, 1989]. Unfortunately no samples in this area have been taken so far. A detailed investigation of any gravity anomalies along the Malpelo Ridge profile could also be of great value.

The existence of an active spreading or asthenospheric upwelling between Regina and Malpelo Ridges is not indicated, as signs of partial melt would be detectable in both P- and S-wave velocities. Similarly the data do not support a plate boundary in this area as proposed by Hardy [1991], although there exist some indications from seismological measurements that the area between Malpelo and Regina Ridges is object to extensional processes. Crustal thickness in this area ranges from 5km to 6km, the existence of a plate

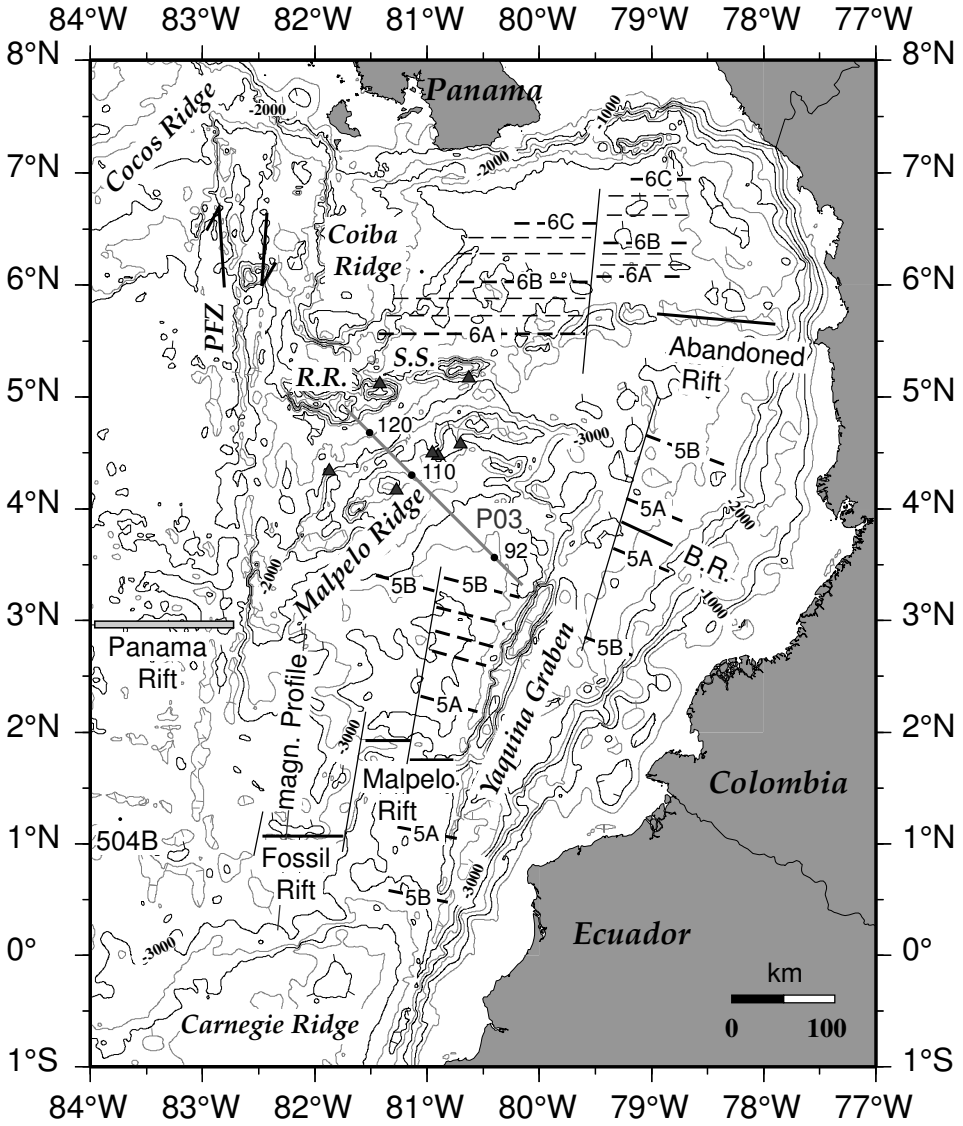


Figure 7.4: Bathymetric Map of the Eastern Panama Basin. Dashed lines denote magnetic anomalies, taken from Lonsdale and Klitgord [1978] and Hardy [1991]. Inactive rift zones are delineated as thick black lines. Small triangles show locations of samples taken within the PAGANINI Cruise SO144-3 [Werner et al., 2000]. A new magnetic profile that was acquired during the cruise is also shown. The abandoned rift was proposed by Hardy [1991]. P03, seismic profile across Malpelo Ridge. Numbers 92, 110, and 120, denote the OBS and OBH stations which are illustrated in Figures 7.1 to 7.3. R.R., Regina Ridge; S.S., Sandra Seamount; PFZ, Panama Fracture Zone; B.R., Buenaventura Rift. Bathymetry after Smith and Sandwell [1997].

boundary would be expected to be associated with porosity in the lower crust and upper mantle, resulting in serpentinization.

New magnetic data acquired south of Malpelo Ridge within the PAGANINI project seem to indicate that Malpelo and Carnegie Ridge were once attached and rifted away as proposed earlier. That both Malpelo and Carnegie Ridge exhibit a thinner upper crust

north of the ridge as opposed to Cocos Ridge, where this asymmetry is pronounced as a thinner upper crust south of the ridge, may further support this suggestion. Werner et al. [2002] propose that seafloor spreading between Carnegie and Malpelo Ridges at $82°W$, which was denoted as "Fossil Rift" by Pennington [1981], occurred between 14.5ma and 9.5ma and that the rift originated from a southward rift jump of a rift segment that was located between Coiba and Malpelo Ridges until 14.5ma. In this context the question of the possible origin of Regina Ridge and Sandra Seamount arises. East-west trending lineations (chapter 5.5, Figure 5.36) indicate that spreading in this region occurred at an east-west trending spreading center, with an orientation similar to the now active Panama Rift or the inactive Malpelo Rift. It seems to be a reasonable suggestion that a former rift located between Coiba and Malpelo Ridge could have been situated between Regina and Malpelo Ridges or jumped southward from a position north of Regina Ridge to a position south of Regina Ridge before a subsequent southward jump to a position between Malpelo and Carnegie Ridges occurred. Regina Ridge would then represent a former part of Malpelo Ridge that was moved north through rifting. The final evaluation of the samples taken during the PAGANINI Cruise SO144-3 [Werner et al., 2000, Hoernle et al., 2002, Werner et al., 2002] will hopefully support this interpretation.

# List of Figures

# Bibliography

[Andel et al., 1972] Andel, T. H. V., Heath, G. R., Malfait, B. T., Heinrichs, D. F., and Ewing, J. I. (1972). Tectonics of the Panama Basin, Eastern Equatorial Pacific. *Geol. Soc. Am. Bull.*, 82:1489–1508.

[Assumpçao, 1980] Assumpçao, M. (1980). Determination of Moho dip using PS reflections. *Geophys. J. R. astr. Soc.*, 60:77–84.

[Au and Clowes, 1984] Au, D. and Clowes, R. M. (1984). Shear-wave velocity structure of the oceanic lithosphere from ocean bottom seismometer studies. *Geophys. J. R. astr. Soc.*, 77:105–123.

[Barckhausen et al., 2001] Barckhausen, U., Ranero, C., von Huene, R., Cande, S. S., and Roeser, H. A. (2001). Revised tectonic boundaries in the Cocos Plate off Costa Rica: Implications for the segmentation of the convergent margin and for plate tectonic models. *J. Geophys. Res.*, 106(B9):19207–19220.

[Bialas and Flueh, 1999] Bialas, J. and Flueh, E. R. (1999). Ocean Bottom Seismometers. *Sea Technol.*, 40:41–46.

[Bialas et al., 1999] Bialas, J., Flueh, E. R., and Bohrmann, G. (1999). *FS Sonne. Cruise Report SO144-1&2. PAGANINI (PAnama basin and GAlapagos "Plume" - New INvestigations of Intraplate Magmatism)*, volume 94. Geomar Research Center, Kiel, Germany.

[Bratt and Solomon, 1984] Bratt, S. T. and Solomon, S. C. (1984). Compressional and Shear Wave Structure of the East Pacific Rise at 11°20'N: Constraints From Three-Component Ocean Bottom Seismometer Data. *J. Geophys. Res.*, 89(B7):6095–6110.

[Canales et al., 1997] Canales, J. P., Danobeita, J. J., Detrick, R. S., Hooft, E. E. E., Bartolome, R., and Naar, D. F. (1997). Variations in axial morphology along the Galapagos spreading center and the influence of the Galapagos hotspot. *J. Geophys. Res.*, 102(B12):27341–27354.

[Carlson and Herrick, 1990] Carlson, R. L. and Herrick, C. N. (1990). Densities and Porosities in the Oceanic Crust and Their Variations With Depth and Age. *J. Geophys. Res.*, 95(B6):9153–9170.

[Charvis et al., 1999] Charvis, P., Laesanpura, A., Gallart, J., Hirn, A., Lépine, J. C., de Voogd, B., and Pontoise, B. (1999). Spatial distribution of hotspot material added to

the lithosphere under La Réunion, from wide-angle data. *J. Geophys. Res.*, 104:2875–2893.

[Cheung and Clowes, 1981] Cheung, H. P. Y. and Clowes, R. M. (1981). Crustal structure from P- and S-wave analyses: ocean bottom seismometer results in the north-east Pacific. *Geophys. J. R. astr. Soc.*, 65:47–73.

[Chian and Louden, 1994] Chian, D. and Louden, K. E. (1994). The continent-ocean crustal transition across the southwest Greenland margin. *J. Geophys. Res.*, 99(B5):9117–9135.

[Christensen, 1978] Christensen, N. I. (1978). Ophiolites, Seismic Velocities and Oceanic Crustal Structure. *Tectonophysics*, 47:131–157.

[Christensen, 1996] Christensen, N. I. (1996). Poisson‘s ratio and crustal seismology. *J. Geophys. Res.*, 101(B2):3139–3156.

[Christensen and Mooney, 1995] Christensen, N. I. and Mooney, W. D. (1995). Seismic velocity structure and composition of the continental crust: A global view. *J. Geophys. Res.*, 100(B7):9761–9788.

[Christensen and Salisbury, 1979] Christensen, N. I. and Salisbury, M. H. (1979). Seismic anisotropy in the oceanic upper mantle: evidence from the Bay of Islands ophiolite complex. *J. Geophys. Res.*, 84:4601–4610.

[Christeson et al., 1997] Christeson, G. L., Shaw, P. R., and Garmany, J. D. (1997). Shear and compressional wave structure of the East Pacific Rise, 9°-10°N. *J. Geophys. Res.*, 102(B4):7821–7835.

[Clement et al., 1994] Clement, W. P., Carbonell, R., and Smithson, S. B. (1994). Shear-wave splitting in the lower crust beneath the Archean crust of southwest Greenland. *Tectonophysics*, 232:195–210.

[Clowes and Au, 1982] Clowes, R. M. and Au, D. (1982). In-Situ Evidence for a low degree of S-Wave Anisotropy in the Oceanic Upper Mantle. *Geophys. Res. Lett.*, 9(1):13–16.

[Collier and Singh, 1998] Collier, J. S. and Singh, S. C. (1998). Poisson’s ratio structure of young oceanic crust. *J. Geophys. Res.*, 103(B9):20981–20996.

[Collins et al., 1989] Collins, J. A., Purdy, M. G., and Brocher, T. M. (1989). Seismic velocity structure at the Deep Sea Drilling Project Site 504B, Panama Basin: Evidence for thin oceanic crust. *J. Geophys. Res.*, 94(B7):9283–9302.

[Crampin, 1985] Crampin, S. (1985). Evaluation of anisotropy by shear wave splitting. *Geophysics*, 50(1):142–152.

[DeMets et al., 1990] DeMets, C., Gordon, R. G., Argus, D. F., and Stein, S. (1990). Current plate motions. *Geophys. J. Int.*, 101:425–478.

[Detrick et al., 1994] Detrick, R., Collins, J., Stephen, R. A., and Swift, S. (1994). In-situ evidence for nature of the seimic layer 2-3 boundary in oceanic crust. *Nature*, 370:288–290.

[Dick et al., 1992] Dick, H. J. B., Erzinger, J., and Stokking, L. B. (1992). Initial Reports. *Proceedings of the Ocean Drilling Program*, 140.

[Dick et al., 2000] Dick, H. J. B., Natland, J. H., Alt, J. C., Bach, W., Bideau, D., Gee, J. S., and Haggas, S. (2000). A long in situ section of the lower ocean crust: results of ODP Leg 176 drilling at the Southwest Indian Ridge. *Earth Plan. Sci. Lett.*, 179:31–51.

[Dick et al., 1999] Dick, H. J. B., Natland, J. H., and Miller, D. J. (1999). Initial Reports. *Proceedings of the Ocean Drilling Program*, 176.

[Dunn and Toomey, 2001] Dunn, R. A. and Toomey, D. R. (2001). Crack-induced seismic anisotropy in the oceanic crust across the East Pacific Rise (9°30'N). *Earth Plan. Sci. Lett.*, 189:9–17.

[Flueh, 1991] Flueh, E. R., editor (1991). *Seismic studies of laterally heterogenous structures - interpretation and modelling of seismic data.* Comission on controlled source energy (CCSS), Geomar Research Center.

[Flueh and Bialas, 1996] Flueh, E. R. and Bialas, J. (1996). A digital, high data capacity ocean bottom recorder for seismic investigations. *Int. Underwater System Design*, 18(3):18–20.

[Flueh et al., 2001] Flueh, E. R., Bialas, J., and Charvis, P. (2001). *FS Sonne. Cruise Report SO159. SALIERI (South American LIthosphEric transects across volcanic RIdges).*, volume 101. Geomar Research Center, Kiel, Germany.

[Grevemeyer et al., 2001] Grevemeyer, I., Flueh, E. R., Reichert, C., Bialas, J., Kläschen, D., and Kopp, C. (2001). Crustal architecture and deep structure of the Ninetyeast Ridge hotspot trail from active-source ocean bottom seismology. *Geophys. J. Int.*, 144:414–431.

[Gutscher et al., 1999] Gutscher, M.-A., Malavieille, J., Lallemand, S., and Collot, J.-Y. (1999). Tectonic segmentation of the North Andean margin: impact of the Carnegie Rigde collision. *Earth Plan. Sci. Lett.*, 168:255–270.

[Hamilton, 1971] Hamilton, E. L. (1971). Elastic Properties of Marine Sediments. *J. Geophys. Res.*, 76(2):579–604.

[Hamilton, 1976] Hamilton, E. L. (1976). Shear-Wave Velocity versus Depth in Marine Sediments: A Review. *Geophysics*, 41(5):985–996.

[Hammond and Humphreys, 2000] Hammond, W. C. and Humphreys, E. D. (2000). Upper mantle seismic wave velocity: Effects of realistic partial melt geometries. *J. Geophys. Res.*, 105(B5):10975–10986.

[Hardy, 1991] Hardy, N. C. (1991). Tectonic evolution of the easternmost Panama Basin: some new data and inferences. *J. S. Am. Earth Sci.*, 4:261–269.

[Hauff et al., 1997] Hauff, F., Hoernle, K., Schmincke, H.-U., and Werner, R. (1997). A mid-Cretaceous origin for the Galápagos Hotspot: Volcanological, petrological, and geochemical evidence from Costa Rican oceanic crustal segments. *Geol. Rundschau*, 86:141–155.

[Hey, 1977] Hey, R. (1977). Tectoniv evolution of the Cocos-Nazca spreading center. *Bull. Geol. Soc. Am.*, 88(10):1404–1420.

[Hoernle et al., 2002] Hoernle, K., von den Bogaard, P., Werner, R., Hauff, F., Lissinna, B., Alvarado, G. E., and Garbe-Schönberg, D. (2002). Missing history (16-71Ma) of the Galápagos hotspot: Implications for the tectonic and biological evolution of the Americas. *Geophysics, in press*.

[Hoernle et al., 2000] Hoernle, K., Werner, R., Morgan, J. P., Garbe-Schönberg, D., Bryce, J., and Mrazek, J. (2000). Existence of complex spatial zonation in the Galápagos plume for at least 14 m.y. *Geology*, 28(5):435–438.

[Holbrook et al., 1988] Holbrook, W. S., Gajewski, D., Krammer, A., and Prodehl, C. (1988). An Interpretation of Wide-Angle Compressional and Shear Wave Data in Southwest Germany: Poisson's Ratio and Petrological Implications. *J. Geophys. Res.*, 93(B10):12081–12106.

[Humphries, 1995] Humphries, S. E. (1995). Hydrothermal processes at mid-ocean ridges. *Reviews of Geophysics*, 33(Suppl. 1995).

[Ito and Lin, 1995] Ito, G. T. and Lin, J. (1995). Mantle temperature anomalies along the past and paleoaxes of the Galápagos spreading center as inferred from gravity analyses. *J. Geophys. Res.*, 100(B3):3733–3745.

[Iturrino et al., 1991] Iturrino, G. J., Christensen, N. I., Kirby, S., and Salisbury, M. H. (1991). Seismic Velocities and Elastic Properties of Oceanic Gabbroic Rocks from Hole 735B. In von Herzen, R. P. and et al., P. T. R., editors, *Proceedings of the Ocean Drilling Program, Scientific Results*, volume 118, pages 227–237.

[Kearey and Vine, 1999] Kearey, P. and Vine, F. J. (1999). *Global Tectonics*. Blackwell Science, 2nd edition.

[Kellogg and Vega, 1995] Kellogg, J. N. and Vega, V. (1995). Tectonic Development of Panama, Costa Rica, and the Colombian Andes: Constraints from Global Positioning System Geodetic Studies and Gravity. In Mann, P., editor, *Geologic and tectonic development of the Caribbean plate boundary in southern central America*, number 295, pages 75–87. Geol. Soc. Am., Boulder, Colorado, special paper edition.

[Kern and Richter, 1981] Kern, H. and Richter, A. (1981). Temperature Derivatives of Compressional and Shear Wave Velocities in Crustal and Mantle rocks at 6 kbar Confining Pressure. *J. Geophys.*, 49:47–56.

[Klingelhöfer et al., 2000] Klingelhöfer, F., Géli, L., and White, R. S. (2000). Geophysical and geochemical constraints on crustal accretion at the very-slow spreading Mohns Ridge. *Geophy. Res. Lett.*, 27(10):1547–1550.

[Kopf et al., 2001] Kopf, A., Kläschen, D., Weinrebe, W., Flueh, E. R., and Grevemeyer, I. (2001). Geophysical evidence for late stage magmatism at the central Ninetyeast Ridge, Eastern Indian Ocean. *Mar. Geophys. Res.*, 22(3):225–234.

[Kuster and Toksöz, 1974] Kuster, G. T. and Toksöz, M. N. (1974). Velocity and Attenuation of seismic waves in two-phase media: Part II, Experimental results. *Geophysics*, 39:587–606.

[Lewis, 1983] Lewis, B. T. R. (1983). The Process of Formation of Ocean Crust. *Science*, 220(4593):151–157.

[Lonsdale and Fornari, 1980] Lonsdale, P. and Fornari, D. (1980). Submarine Geology of Malpelo Ridge, Panama Basin. *Marine Geology*, 36:65–83.

[Lonsdale and Klitgord, 1978] Lonsdale, P. and Klitgord, K. D. (1978). Structure and tectonic history of the eastern Panama Basin. *Geol. Soc. Am. Bull.*, 89:981–999.

[Luetgert, 1992] Luetgert, J. (1992). MacRay-Interactive two-dimensional seismic ray-tracing for the MacIntosh. Technical Report 92, U.S. Geol. Survey.

[Marcaillou, 2000] Marcaillou, B. (2000). Structure Profonde de la Ride de Malpelo (Colombie): Implications Geodynamiques. Master's thesis, Université P. et M. Curie (Paris VI-Villefranche).

[Meschede et al., 1998] Meschede, M., Barckhausen, U., and Worm, H.-U. (1998). Extinct spreading on the Cocos Ridge. *Terra Nova*, 10:211–216.

[Mithal and Mutter, 1989] Mithal, R. and Mutter, J. C. (1989). A low velocity zone within the layer 3 region of 118 Myr old oceanic crust in the western North Atlantic. *Geophys. J.*, 97:275–294.

[Mjelde, 1992] Mjelde, R. (1992). Shear waves from three-component ocean bottom seismographs off Lofoten, Norway, indicative of anisotropy in the lower crust. *Geophys. J. Int.*, 110:283–296.

[Müller, 1985] Müller, G. (1985). The reflectivity method: a tutorial. *J. Geophys.*, 58:153–174.

[Mutter and Mutter, 1993] Mutter, C. Z. and Mutter, J. C. (1993). Variations in thickness of layer 3 dominate oceanic crustal structure. *Earth Plan. Sci. Lett.*, 117:295–317.

[Nakamura and Garmany, 1991] Nakamura, Y. and Garmany, J. (1991). Development of upgraded ocean bottom seismograph. Technical Report 111, Univ. of Texas, Institute of Geophysics.

[Nicolas and Christensen, 1987] Nicolas, A. and Christensen, N. I. (1987). Formation of Anisotropy in Upper Mantle Peridotites - A Review. In Fuchs, K. and Froidevaux, C., editors, *Composition, Structure and Dynamics of the Lithosphere-Asthenosphere System (Geodynamics Series)*, volume 16, pages 111–123. AGU.

[O'Connor et al., 2002] O'Connor, J. M., Stoffers, P., Wijbrans, J., Ackermand, D., and Worthington, T. (2002). *SO144-PAGANINI: PAnama basin and GAlapagos plume - New INvestigatios of Intraplate magmatism. Abschlussbericht an das BMBF*. Institut für Geowissenschaften, Universität Kiel.

[Pennington, 1981] Pennington, W. D. (1981). Subduction of the Eastern Panama Basin and Seismotectonics of Northwestern South America. *J. Geophys. Res.*, 86(B11):10753–10770.

[Protti and Schwartz, 1994] Protti, M. and Schwartz, S. Y. (1994). Mechanics of back arc deformation in Costa Rica: Evidence from an aftershock study of the April 22, 1991, Valle de la Estrella, Costa Rica, earthquake (Mw=7.7). *Tectonics*, 13(5):1093–1107.

[Rosendahl, 1976] Rosendahl, B. R. (1976). Evolution of Oceanic Crust 2. Constraints, Implications, and Inferences. *J. Geophys. Res.*, 81(29):5305–5314.

[Rosendahl et al., 1976] Rosendahl, B. R., Raitt, R. W., Dorman, L. M., and Bibee, L. D. (1976). Evolution of Oceanic Crust 1. A Physical Model of the East Pacific Rise Crest Derived From Seismic Refraction Data. *J. Geophys. Res.*, 81(29):5294–5304.

[Salisbury and Christensen, 1978] Salisbury, M. H. and Christensen, N. I. (1978). The Seismic Velocity Structure of a Traverse Through the Bay of Islands Ophiolite Complex, Newfoundland, an Exposure of Oceanic Crust and Upper Mantle. *J. Geophys. Res.*, 83(2):805–817.

[Shaw, 1994] Shaw, P. R. (1994). Age ariations of oceanic crust Poisson's ratio: Inversion and a porosity evolution model. *J. Geophys. Res.*, 99(B2):3057–3066.

[Shearer, 1988] Shearer, P. M. (1988). Cracked media, Poisson's ratio and the structure of the upper oceanic crust. *Geophys. J. R. Astron. Soc.*, 92:357–362.

[Siegesmund et al., 1989] Siegesmund, S., Takeshita, T., and Kern, H. (1989). Anisotropy of $V_P$ and $V_S$ in an amphibolite of the deeper crust and its relationship to the mineralogical, microstructural and textural characteristics of the rock. *Tectonophysics*, 157:25–38.

[Simmons, 1964] Simmons, G. (1964). Velocity of Shear Waves in Rocks to 10 Kilobars, 1. *J. Geophys. Res.*, 69(6):1123–1130.

[Sinton et al., 1998] Sinton, C. W., Duncan, R. A., Storey, M., Lewis, J., and Estrada, J. J. (1998). An oceanic flood basalt province within the Carribean plate. *Earth Plan. Sci. Lett.*, 155:221–235.

[Smith and Sandwell, 1997] Smith, W. H. F. and Sandwell, D. T. (1997). Global sea floor topography from satellite altimetry and ship depth soundings. *Science*, 277:1956–1962.

[Spencer and Nur, 1976] Spencer, J. W. and Nur, A. M. (1976). The Effects of Pressure, Temperature, and Pore Water on Velocities in Westerly Granite. *J. Geophys. Res.*, 81(5):899–904.

[Spudich and Orcutt, 1980] Spudich, P. and Orcutt, J. (1980). Petrology and Porosity of an oceanic crustal site: Results from wave form modelling of seismic refraction data. *J. Geophys. Res.*, 85(B3):1409–1433.

[Stephen, 1985] Stephen, R. A. (1985). Seismic anisotropy in the upper oceanic crust. *J. Geophys. Res.*, 90:11383–11396.

[Stephen, 1988] Stephen, R. A. (1988). Lateral Heterogenity in the Upper Oceanic Crust at Deep Sea Drilling Project Site 504. *J. Geophys. Res.*, 93(6):6571–6584.

[Streckeisen, 1978] Streckeisen, A. L. (1978). IUGS Subcommission on the Systematics of Igneous Rocks. Classification and Nomenclature of Volcanic Rocks, Lamprophyres, Carbonatites and Melilite Rocks. Recommendations and Suggestions. *Neues Jahrbuch für Mineralogie, Abhandlungen*, 141:1–14.

[Swift et al., 1998a] Swift, S. A., Kent, G. M., Detrick, R. S., Collins, J. A., and Stephen, R. A. (1998a). Oceanic basement structure, sediment thickness, and heat flow near Hole 504B. *J. Geophys. Res.*, 103(7):15377–15391.

[Swift et al., 1998b] Swift, S. A., Lizarralde, D., Stephen, R. A., and Hoskins, H. (1998b). Seismic attenuation in upper ocean crust at Hole 504B. *J. Geophys. Res.*, 103(11):27193–27206.

[Swift et al., 1998c] Swift, S. A., Lizarralde, D., Stephen, R. A., and Hoskins, H. (1998c). Velocity structure in upper ocean crust at Hole 504B from vertical seismic profiles. *J. Geophys. Res.*, 103(7):15361–15376.

[Swift and Stephen, 1992] Swift, S. A. and Stephen, R. A. (1992). How much Gabbro is in Ocean Seismic Layer 3. *Geophys. Res. Lett.*, 19(18):1871–1874.

[Trey et al., 1999] Trey, H., Cooper, A. K., Pellis, G., della Vedova, B., Cochrane, G., Brancolini, G., and Makris, J. (1999). Transect across the West Antarctic rift system in the Ross Sea, Antarctica. *Tectonophysics*, 301:61–74.

[Wade et al., 1977] Wade, U. S., Lister, C. R. B., and Lewis, B. T. R. (1977). Seismic refraction over Malpelo Ridge in the Panama Basin. In Ramirez, J. E. and Aldrich, L. T., editors, *The Ocean-Continent Transition in Southeast Colombia*, pages 209–216. Editora Guadelupe Ltda., Bogota, Inst. Geofisico, Universidad Javeriana, Bogota.

[Walther, 2001a] Walther, C. H. E. (2001a). Crustal structure of the Cocos Ridge north-east of Cocos Island, Panamá Basin. subm. J. Geophys. Res.

[Walther, 2001b] Walther, C. H. E. (2001b). The crustal structure of the Cocos Ridge off Costa Rica. subm. J. Geophys. Res.

[Werner et al., 2000] Werner, R., Ackermand, D., Worthington, T., and ShipboardScientificParty (2000). *Cruise Report SONNE 144-3*. Number 10. Ber. Rep.Inst. Geowiss. Univ. Kiel, Kiel, Germany.

[Werner et al., 2002] Werner, R., Hoernle, K., Barckhausen, U., and Hauff, F. (2002). The geodynamic evolution of the Galápagos System (Central East Pacific) over the past 20 m.y.: Constraints from Morphology, Geochemistry, and Magnetic Signatures. in prep.

[Werner et al., 1999] Werner, R., Hoernle, K., van den Bogaard, P., Ranero, C., and von Huene, R. (1999). Drowned 14-m.y.-old Galápagos archipelago off the coast of Costa rica: Implications for tectonic and evolutionary models. *Geology*, 27(6):499–502.

[Wessel and Smith, 1999] Wessel, P. and Smith, W. H. F. (1999). The Generic Mapping Tools, GMT Version 3.2 Technical Reference and Cookbook. Technical report, School of Ocean and Earth Science and Technology, University of Hawaii at Manoa, NOAA/NESDIS/NODC.

[Westbrook et al., 1995] Westbrook, G. K., Hardy, N. C., and Heath, R. P. (1995). Structure and Tectonics of the Panama-Nazca Plate Boundary. In Mann, P., editor, *Structure and Tectonics of the Panama-Nazca Plate Boundary*, number 295, pages 91–109. Geol. Soc. Am., Boulder, Colorado, special paper edition.

[White and McKenzie, 1989] White, R. S. and McKenzie, D. (1989). Magmatism at Rift Zones: The Generation of Volcanic Continental Margins and Flood Basalts. *J. Geophys. Res.*, B6(94):7685–7729.

[White et al., 1992] White, R. S., McKenzie, D., and O'Nions, R. K. (1992). Oceanic Crustal Thickness From Seismic Measurements and Rare Earth Element Inversions. *J. Geophys. Res.*, 97(B13):19683–19715.

[White and Stephen, 1980] White, R. S. and Stephen, R. A. (1980). Compressional to shear wave conversion in oceanic crust. *Geophys. J. R. astr. Soc.*, 63:547–565.

[Wilkens et al., 1992] Wilkens, R. H., Cheng, C. H., and Meredith, J. A. (1992). Evaluation and Predicition of Shear Wave Velocities in Calcareous Marine Sediment and Rocks. *J. Geophys. Res.*, 97(B6):9297–9305.

[Wilkens et al., 1991] Wilkens, R. H., Fryer, G. J., and Karsten, J. (1991). Evolution of Porosity and Seismic Structure of Upper Oceanic Crust: Importance of Aspect Ratios. *J. Geophys. Res.*, 96(B11):17981–17995.

[Wilson and Hey, 1995] Wilson, D. S. and Hey, R. (1995). History of rift propagation and magnetization intensity for the Cocos-Nazca spreading center. *J. Geophys. Res.*, 100(B7):10041–10056.

[Yoder and Tilley, 1962] Yoder, H. S. and Tilley, C. E. (1962). Origin of basalt magmas: an experimental study of natural and synthetic rock systems. *J. Petrology*, 3:342–532.

[Zoeppritz, 1919] Zoeppritz, K. (1919). Über Reflexion und Durchgang seismischer Wellen durch Unstetigkeitsflächen. *Über Erdbebenwellen, Nachrichten der Königlichen Gesellschaft der Wissenschaften zu Göttingen. Mathematik-Physik.*, pages 47–84.

# Acknowledgements

I am very grateful to Prof. Dr. Ernst Flueh for his continuous support, advice, and understanding during the last few years.

Many thanks to the participants of the SONNE Cruises 144-1,2,&3, especially to the crew, for their professional help during data acquisition.

Prof. Dr. Philippe Charvis and Boris Marcaillou were so kind to give permission to work on the Malpelo Ridge data.

I thank Prof. Dr. Wolfgang Rabbel for spontaneously agreeing to act as co-reference.

Many thanks to Prof. Dr. Karl Millahn for his encouraging support.

During the final year of this work financial support was granted by the Austrian Academy of Sciences within the DOC-programme.
A stipendium ”Zur Förderung wissenschaftlicher Arbeiten im Ausland” by the Bundesministerium für Wissenschaft und Verkehr, Republik Österreich, was granted in 2000.

Special thanks to all members of the Geodynamics Department for their friendly assistance and for the kind atmosphere within the department.